Methods for Improving Comparability of Propeller Acoustic Experiments Conducted at Different Facilities and Scales

ThanhLong J. Duong

Thesis submitted to the Faculty of the
Virginia Polytechnic Institute and State University
in partial fulfillment of the requirements for the degree of

Master of Science
in
Aerospace Engineering

William N. Alexander, Chair
Nanyaporn Intaratep
Kevin T. Lowe

27 February 2026
Blacksburg, Virginia

Keywords: UAM, Propeller Broadband Noise, Ground Boards, Anechoic Wind Tunnel, Outdoor Field Tests, Predictability and Comparability

Methods for Improving Comparability of Propeller Acoustic Experiments Conducted at Different Facilities and Scales

ThanhLong J. Duong

(ABSTRACT)

Development of urban air mobility (UAM) vehicles are on the rise, and their noisy operation near many people can cause negative health effects, so it is important to quickly understand their acoustic behaviors. This is done through many conduits, including computational fluid dynamics (CFD), outdoor field tests, and controlled indoor experiments. Outdoor field tests allow for full-scale vehicle testing, but subjects the test article to uncontrollable, unpredictable variables, whereas indoor experiments are much more controllable and predictable, but such indoor experiments are often constrained by space and are unable to test the full-scale vehicle. Research should develop methods to improve comparability between indoor and outdoor acoustic experiments. The presented work aims to provide such methods with three experiments: one investigating ground board acoustic behavior in an anechoic chamber, one investigating propeller noise in an outdoor facility, and one investigating propeller noise in an indoor facility.

Ground boards are thin rigid boards, typically in the shape of a $1m$ diameter circle a few millimeters thick, and are standardized for use [5] [10] [11] [13] in outdoor acoustic experiments to mount microphones and provide a consistent reflective surface. An experiment was conducted in an anechoic chamber to observe the behavior of a $1m$ diameter, $6mm$ thick plywood ground board with the noise source at various incidence angles and with the microphone lain at the center and at three-quarters the radius of the ground board. The configuration of interest is a 23° incidence angle with the microphone at the center since this is the configuration used in the outdoor field test. With this configuration, the behavior of the ground board is similar to that of a perfect reflector ($6dB$ increase in measured sound pressure level (SPL)) within about $200Hz$ to $10000Hz$. Below $2000Hz$, the shallower source angles (20°, 23°, and 45°) have a lower SPL magnification; in the $2000Hz$ to $8000Hz$ frequency range, there appears to be little dependence of ΔPSD on the source angle; above $8000Hz$, the higher source angles (65° and 80°) have a lower SPL magnification. With the microphone lain at three-quarters the radius of the ground board, a similar trend was observed, but its sensitivity to the source angle was lower.

A Techsburg Inc. propeller was tested in an outdoor facility at two scales: $0.914m$ and $0.457m$ diameters. The propeller was mounted with its center $1.905m$ above the ground, and 13 microphones were placed on top of ground boards in a $4.6m$ semicircle around the propeller, ranging from upstream to downstream of the propeller. Wind measurements were simultaneously collected from an anemometer a few meters away from the microphone arc. The background noise at this facility was significant up to about $800Hz$, and motor noise was significant around $5000Hz$ to $9000Hz$. Wind velocity data was collected simultaneously

to acoustics, and a relationship was found between broadband noise and inflow velocity. The total propeller noise was decomposed into broadband and tonal components through phase averaging methods, and it was found that the overwhelming majority of the noise was dominated by the broadband component. Generally, when the inflow velocity was about $-1m/s$ to $0.5m/s$, the broadband noise within $2000Hz$ to $5000Hz$ was about $1dB$ to $2dB$ louder than when the inflow velocity was about $0.5m/s$ to $3m/s$. Furthermore, the spectra calculated from when the inflow velocity was between $-1m/s$ and $0.5m/s$ was much more comparable to the Gill-Lee Spectrum Model (GLSM), a trailing edge noise prediction model trained on hundreds of propeller noise datasets primarily at a hover condition. To compare the two scales, the tip Mach number was held constant, so the $0.914m$ diameter propeller rotated half as fast as the $0.457m$ diameter propeller, resulting in half the blade passage frequency (BPF) and twice the harmonics. The broadband noise of the larger propeller peaked around $2000Hz$, whereas the smaller propeller's broadband curve peaked around $4500Hz$. This relative peak behavior is reflected in the GLSM, although the GLSM generally overpredicts both scales. The expected difference in tones between the two scales was calculated from the thrust squared to be approximately $11dB$, and the observed difference in tones was observed to be approximately $7dB$ at most. However, these thrust measurements were averaged over the entire sampling period, so the absolute magnitude of this calculation should be considered with reasonable skepticism. The reduction in pitch angle resulted in quieter broadband noise, which is expected since this would reduce thrust and therefore reduce noise. The addition of turbulence trips did not result in the expected consistent increase in broadband noise, but this may be due to the inherent difficulty of outdoor acoustic experiments: the environmental conditions in field tests are uncontrollable, and sequestration was unable to isolate period of similar wind velocities, so the two datasets were not entirely comparable.

A similar experiment was performed in an anechoic wind tunnel, the Virginia Tech Subsonic Modular Anechoic Research Tunnel (VTSMART), to observe the effects of test facility. Five microphones were mounted at the same height as the propeller $1.016m$ away from the propeller, evenly spaced by 10° between each, starting from 10° upstream to 30° downstream. A sixth microphone was mounted further downstream closer to the axis of rotation. Due to size constraints of the wind tunnel, only the $0.457m$ diameter propeller was tested at this facility. Background noise was much quieter and more consistent than the outdoor facility, and the SNR was positive throughout $100Hz$ to $20000Hz$. Spectrograms were generated for both background and propeller noise measurements, and both were found to be relatively constant in time, so the background noise was directly subtracted from the propeller noise measurements. Again, the total propeller noise was broken into broadband and tonal components, and the majority of the noise was still composed of the broadband component. The tunnel was operated at two conditions: one without flow and one with $4m/s$ flow. Between the two tunnel conditions, the broad spectral features did not change significantly, and the largest differences were observed in the tonal features. With $4m/s$ flow, the tones at the BPF were quieter than without flow by approximately $5dB$. The GLSM generally captured the broad spectral features at the indoor facility better than at the outdoor facility, typically within about $3dB$ of the experimental data. The data from both experiments were

compared to each other after a correction to account for the difference in distance. The outdoor broadband noise with an inflow velocity of about $0.5m/s$ to $3m/s$ was similar to the indoor broadband noise with $4m/s$ flow in the $2000Hz$ to $6000Hz$ range within about $2dB$, and a similar result is seen when comparing the outdoor broadband noise with an inflow velocity of $-1m/s$ and $0.5m/s$ to the indoor broadband noise with no flow. All configurations were again compared to each other at this facility, but much smaller differences were observed. This is likely due to the confinement of the wind tunnel facility and the inability of the wake to be convected far enough downstream of the propeller, causing these broadband noise sources to dominate over changes in pitch and turbulence trips.

In each experiment, there are many limitations and possible improvements with further research. For the ground board experiment, more source incidence angles, microphone orientations, and surrounding substrates could be tested, which would improve the understanding of ground board response. Such research has been done in the past [2] [4] [14] [22]. For the outdoor Drone Park experiment, the ground boards could have been calibrated before collecting propeller acoustics so that measurements could be properly corrected for the effects of the ground board in the field. Wind anemometer data could also be fully synchronized to the propeller acoustics such that direct correlations would be more meaningful. Similarly, synchronized performance data should be collected as well, specifically thrust and torque, which would allow for more accurate GLSM calculations, since this model takes thrust into consideration. For the indoor VTSMART experiment, particle imaging velocimetry (PIV) could be conducted to observe the physical phenomena and confirm if the confinement of the wind tunnel is indeed causing the wake to loiter near the propeller.

Methods for Improving Comparability of Propeller Acoustic Experiments Conducted at Different Facilities and Scales

ThanhLong J. Duong

(GENERAL AUDIENCE ABSTRACT)

Urban air mobility (UAM) vehicles are designed to operate similar to taxis in the air for better transportation in cities. However, these UAM vehicles generate loud noises, typically by the use of rotors, so it is important to understand the acoustic behavior of these vehicles. This can be done through both indoor and outdoor experiments, but both have their benefits and drawbacks. With indoor experiments, the environment is very controlled, but it is constrained by space, and only smaller scale rotors can be tested. With outdoor experiments, the space is virtually unlimited, and full-scale rotors can be tested; however, the environment is uncontrollable, and effects like background noise may be too loud for reasonable experimentation. It is important to be able to compare experiments from both facilities and obtain repeatable results; therefore, this work aims to provide a few such methods.

In outdoor acoustic experiments, there are standards that require the use of ground boards [5] [10] [11] [13], which are essentially thin rigid plates, typically in the shape of a circle a few millimeters thick. Microphones are directly mounted on top of these ground boards, which provides a surface that has consistent reflective properties to improve repeatability between outdoor acoustic experiments. An experiment was conducted in an anechoic chamber to observe how a $1m$ diameter, $6mm$ thick plywood ground board affects microphone measurements with a speaker at various angles and with various microphone mounting methods. The configuration of interest is a 23° angle with the microphone simply lain at the center of the ground board. In this configuration, the ground board behaves similarly to a perfect reflector, which increases the sound heard by the microphone by $6dB$ compared to if the ground board was not there at all.

A Techsburg Inc. propeller was tested in an outdoor facility at two sizes: $0.914m$ and $0.457m$ diameters. The propeller was mounted $1.905m$ above the ground, and 13 microphones were placed at the center of their own ground boards in a $4.6m$ semicircle, which matches the 23° angle from the previous experiment. Wind measurements were simultaneously collected to acoustics, and a relationship between the wind velocity into the face of the propeller and the noise between $2000Hz$ to $6000Hz$. Background noise at this facility was significant up to $800Hz$, and the noise generated by the motor was significant between $5000Hz$ to $9000Hz$. The propeller noise was broken into two components: broadband (noise spread over a broad range of frequencies) and tonal (noise concentrated at one frequency), and the majority of the noise consisted of the broadband component. Generally, when the inflow velocity was about $-1m/s$ to $0.5m/s$, the broadband noise was louder than when the inflow velocity was about $0.5m/s$ to $3m/s$. Furthermore, the noise when the inflow velocity was about $0.5m/s$ to $3m/s$ was more similar to the Gill-Lee Spectrum Model (GLSM), a

broadband noise prediction model based mostly on zero-inflow conditions. To compare the two propeller sizes, the tip speeds were held constant, so the larger propeller spun half as fast as the smaller propeller. The broadband noise of the larger propeller was loudest at a lower frequency than the smaller propeller, which is predicted by the GLSM. The difference in tones between the two sizes was about $7dB$, but this was expected to be slightly higher at $11dB$. This was predicted using the measured thrust values, but it should be noted that the thrust was not measured simultaneously to the acoustics, so this prediction may have higher uncertainty. The reduction in pitch (angle of each blade) resulted in reduced broadband noise, which is expected since this would reduce thrust and therefore reduce noise. The addition of turbulence trips did not result in the consistent increase in broadband noise, but this may be due to the chaotic, uncontrollable outdoor environment causing unforeseen changes to the broadband levels.

A similar experiment was performed in an anechoic wind tunnel, the Virginia Tech Subsonic Modular Anechoic Research Tunnel (VTSMART). This was done to observe the differences between a chaotic outdoor environment to a controlled indoor environment. Five microphones were mounted at the same height as the propeller $1.02m$ away from the propeller, evenly spaced by 10° between each. Due to size constraints of the wind tunnel, only the $0.457m$ diameter propeller was tested at this indoor facility. The wind tunnel was operated without flow and with $4m/s$ flow. Background noise was quieter compared to the outdoor facility, and the propeller was significantly louder than the background noise. Both propeller and background noise were found to be unchanging in time, so the background noise was directly subtracted from the propeller noise measurements. Again, the propeller noise was separated into broadband and tonal components, and the majority of the noise was also composed of the broadband component. Between the two flow conditions, the broadband noise did not change significantly, whereas the largest differences were observed in the tones. The tones were quieter by about $5dB$ with $4m/s$ flow than without flow. The GLSM generally captured the broadband noise features at the indoor facility better than at the outdoor facility. The broadband noise between the two experiments generally agreed when matching the flow conditions: the noise from the outdoor experiment with wind between $0.5m/s$ and $3m/s$ matched the noise from the indoor experiment with $4m/s$ flow, and the noise from the outdoor experiment with wind between $-1m/s$ and $0.5m/s$ matched the noise from the indoor experiment without flow. Changes in pitch and turbulence trips at the indoor facility did not yield significant changes in the broadband noise. This is likely due to the spatial confinement of the wind tunnel facility, which would trap flow features near the propeller, causing these broadband noise sources (which would be relatively the same with each configuration change) to dominate over changes in pitch and turbulence trips.

In each experiment, there are many limitations and possible improvements with further research. For the ground board experiment, more source angles, microphone orientations, and surrounding materials could be tested, which would improve the understanding of ground board response. Such research has been done in the past [2] [4] [14] [22], proving its feasibility. For the outdoor Drone Park experiment, the effect of the ground boards in the actual field could have been understood before collecting propeller acoustics so that measurements could

be properly corrected. Wind data could also be fully synchronized to the propeller acoustics such that direct correlations would be more meaningful. Similarly, synchronized thrust data should be collected as well, which would allow for more accurate GLSM predictions, since this model takes thrust into consideration. For the indoor VTSMART experiment, flow visualization techniques could be used to observe the physical phenomena and confirm if the confinement of the wind tunnel is indeed trapping flow features near the propeller.

Dedication

To my loving family.

Acknowledgments

I'd like to begin by thanking my advisor, Dr. Nathan Alexander. Thank you for providing me with this unique opportunity to dig into and get to really know this part of the aerospace engineering field. Thank you for your mentorship and guidance, and for being much more patient with me than I would have been with myself. For my entire committee, Dr. Nanyaporn Intaratep and Dr. Kevin Todd Lowe, thank you as well for your support and advice throughout my entire graduate career. To Bill Oetjens and Dr. Aurelien Borgoltz, thank you for starting this snowball of a journey and introducing me to Dr. Alexander years ago.

I'd also like to thank those on collaborating teams: Jonathan Fleming, Matthew Langford, and Will Walton from Techsburg, Inc.; Ricardo Burdisso and Bennett Witcher from AVEC, Inc.; and James Lambert, Cameron Hollandsworth, and Roy Handy from the AOE Machine Shop. It was a pleasure to first meet you years ago in the Stability Wind Tunnel, and I am glad that I got the opportunity to work with you again. Thank you all for allowing me to be a part of your team, and it has been a genuine pleasure working with you.

I'd like to acknowledge the sponsor for this work, the NASA SBIR/STTR office, for providing the funding to perform this work under the Phase I STTR contract 80NSSC23PB607, as well as the NASA ULI funding after the completion of the Phase 1 project.

I am also very grateful for my fellow students. First, the NASA ULI team, Steve Huang, Shreyas Chaware, and Ryan Lundquist, thank you for incorporating me into your team and showing me how to navigate this space. I'd also like to thank Charlie Galluscio, Charlie Van Horn, Andrew Single, and Muhammad Raza, for fostering a very welcoming and open environment, for giving me pointers for my research, and for putting up with my sense of humor.

I also want to thank my closest friends in Blacksburg also in the aerospace engineering department, Jack Gradle and Rory Underwood, who have always believed in me, and have pushed me to do better while supporting me at my worst. Thank you for the cheers and the beers.

Lastly, and perhaps most importantly, I'd like to thank my family, my mom, dad, and little brother, who have shaped me to be who I am so I could get to where I am today. Thank you for your unconditional love and support, and I hope this makes you proud.

Thanks everyone,
ThanhLong Duong

Contents

List of Figures

List of Tables

List of Abbreviations

Abbreviations

B&K Brüel & Kjær

BPF Blade Passage Frequency

BVI Blade Vortex Interaction

BWI Blade Wake Interaction

CAD Computer-Aided Design

CFD Computational Fluid Dynamics

EA Excess Attenuation

EASA European Union Aviation Safety Agency

GLSM Gill-Lee Spectrum Model

ICAO International Civil Aviation Organization

IEC International Electrotechnical Commission

ISO International Organization for Standardization

OASPL Overall Sound Pressure Level

PSD Power Spectral Density

RPM Rotations Per Minute

SPL Sound Pressure Level

TIN Turbulence Ingestion Noise

UAM Urban Air Mobility

VFS Vertical Flight Society

VTSMART Virginia Tech Subsonic Modular Anechoic Research Tunnel

Symbols

α_{eff} Effective Angle of Attack

β Local Twist Angle

$\Delta f_{1/3}$ Third-Octave Band Frequency Bandwidth

Δf_{Narrow} Narrowband Frequency Bandwidth

$\delta\,[a]$ Uncertainty of Variable "x"

Δ_{GL} Gill-Lee Spectrum Model Parameter

σ Propeller Solidity

θ_0 Observer Elevation Angle Relative to Propeller Plane

$\vec{V}_{Tip}$ Blade Tip Velocity

C Clean Signal

C_T Thrust Coefficient

c_σ Solidity-Weighted Chord Length

f Frequency

f_S Sampling Frequency

G_{aa} Autospectrum of Variable "a"

G_{ab} Cross Spectrum Between Variables "a" and "b"

$G_{pp,Corrected}$ Corrected Autospectrum of Pressure

$G_{pp,Raw}$ Raw Autospectrum of Pressure

G_{pp} Autospectrum of Pressure

H_{Cal} Calibration Transfer Function

M_t Blade Tip Mach Number

N Number of Propeller Blades

N_{Rec} Number of Records

n_{Rec} Number of Samples Per Record

p_a Ambient Pressure

p_d Dynamic Pressure

$p_{incident}$ Incident Sound Pressure

p_{Ref} Reference Pressure

p_{total} Total Measured Sound Pressure

PSD Power Spectral Density

q Fractional Record Overlap

R Gas Constant

R Propeller Radius

s_0 Observer Distance Relative to Center of Propeller Disk

S_t Strouhal Number

$SPL_{1/3}$ Third-Octave Band Sound Pressure Level

SPL_{Narrow} Narrowband Sound Pressure Level

T Sampling Period

T_a Ambient Temperature

U_∞ Freestream Flow Velocity

V_t Blade Tip Velocity

v_{local} Linear Velocity at a Local Blade Location

EA Excess Attenuation

Chapter 1

Introduction

1.1 Motivation

Urban air mobility (UAM) vehicles and concepts are designed to operate in cities and areas with a dense population. These vehicles generate noise which can cause negative health effects to residents. Therefore, UAM development must focus on minimizing noise to safely operate at full scale.

To further understand UAM propeller noise, experiments are conducted at both indoor and outdoor facilities, each having their own benefits and drawbacks. In indoor facilities such as wind tunnels, the environment can be controlled, reducing background noise, reflections, turbulence, and other unwanted noise sources that would be present and uncontrollable in an outdoor facility. On the other hand, outdoor facilities are much less limited by space than indoor facilities, so full-scale test articles can be tested for a direct understanding of the UAM vehicle or structure. Balancing these pros and cons may be difficult without access to very large anechoic wind tunnels, such as the National Full-Scale Aerodynamics Complex (NFAC) at the NASA Ames Research Center, so for most researchers, effects of scale, testing environment, and the ability to relate experiments using different scales and testing environments are of interest.

1.2 Literature Review and Theoretical Background

1.2.1 Propeller Acoustics

In general, the aerodynamic noise produced by propellers and rotors mainly arises from the interaction between a solid body and a fluid medium. There are many different ways these interactions can occur, but for a propeller, they can generally be categorized into two sets based on the type of noise they produce: broadband noise sources and tonal noise sources. Tonal noise is the sound associated with purely periodic phenomena, namely the shaft rate, blade passage frequency (BPF), and their harmonics, which are ideally constant. Broadband noise is the sound associated with the interaction of the propeller with stochastic and non-periodic events, such as atmospheric turbulence. A tree diagram adapted from Marte and

Kurtz [18] is shown in Figure 1.1, which shows a general breakdown of aerodynamic noise sources.

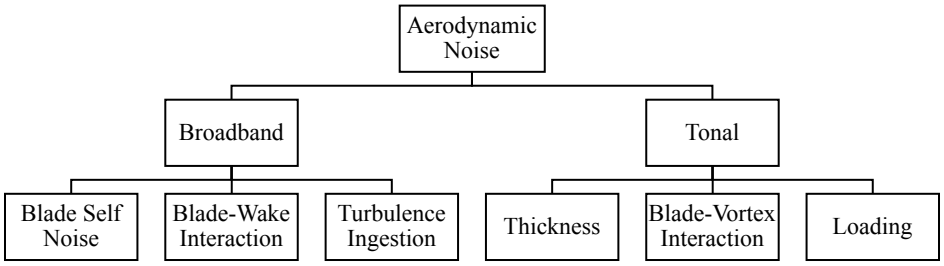

Figure 1.1: Hierarchy of General Aerodynamic Noise Sources.

Tonal noise can be further broken down into more sources, three of which will be addressed in this discussion. The first source is thickness noise, which is mainly dependent on body geometry and rotational speed. Thickness noise arises from the displacement of the fluid medium as the body passes through. From the perspective of a stationary observer, this periodic mass fluctuation appears as a monopole source, but generally dominates over other sources within the rotor plane. The second source that will be addressed is blade-vortex interaction (BVI), which is a subset of a more general periodic interaction noise category. BVI noise is generated by the interaction between the blades and the flow generated by the tip vortices of each blade. These tip vortices can be modeled by an elementary vortex, which generates a constant and predictable flow. The periodic interaction between the blades and this constant vortex flow causes strong tonal noise with dipole directivity. The last tonal noise source is steady loading noise, which is caused by the steady thrust and torque of the propeller. These loads are caused by the lift and drag of each blade. However, from the perspective of a stationary observer, these forces fluctuate at the rate of the BPF. Intuitively, the thrust noise is directed along the axis of rotation and the torque noise is directed along the plane of rotation.

Broadband noise can also be broken down into different sources, and three will be addressed. The first is blade self noise, which is essentially the interaction between the blade airfoil and its own unsteady pressure fluctuations, most commonly and dominantly trailing edge interaction with and scattering of a turbulent boundary layer. The trailing edge noise and blade self noise in general radiates upstream of each airfoil, which translates to strongest directivity in the plane of rotation. The second source of broadband noise to be discussed is turbulence ingestion noise (TIN). This is caused by the interaction between the rotor and atmospheric turbulence, and this is heard as broadband noise because the atmospheric turbulence is stochastic in nature. The directivity of TIN can be quite complex and dependent on blade pitch and inflow conditions, but can be modeled as a dipole along the axis of rotation assuming an acoustically compact rotor. The last broadband noise source is from blade-wake interaction (BWI). Recall that tip vortices are generated and can be understood as a constant vortex. This core vortex is constant in time, but also carries some turbulence that fluctuates around this core flow. Additionally, the stochastic wake from portions of the

span closer to the propeller center may have influences and cause more interactions. The interaction between the blades and this turbulence associated with the wake of the preceding blade is the cause for BWI, which also has directivity similar to TIN. An important distinction between BWI and TIN should be made: if the wake of the propeller is recirculated and reingested into the propeller, this is no longer classified as a blade-wake interaction, but rather turbulence ingestion.

Some of these sources are relatively trivial to predict and model, such as the tonal thickness and steady loading noise sources. More difficult to predict and model is generally the broadband noise, such as TIN and BWI. The latter sources are more difficult because they are more sensitive to unpredictable events, such as environmental turbulence or self-generated turbulence. In the context of developing more consistent predictions and experiments, the less predictable broadband noise is of relatively higher interest.

1.2.2 Ground Board Research

Outdoor acoustic experiments commonly employ a ground board, which are essentially a large plate on which microphones are mounted. These ground boards provide a surface that will behave consistently among different experiments such that microphone recordings are comparable and repeatable among these experiments. However, indoor acoustic experiments are commonly conducted in anechoic chambers, where ground boards would not be necessary. Therefore, regardless of the acoustic source, the effect of ground boards must be understood to compare results from various experiments.

Currently, there exist many standards and regulations for noise measurement processes regarding the use of a microphone and plate or ground board, which share general guidelines among each other with small discrepancies. For example, both the International Civil Aviation Organization (ICAO) [10] and the European Union Aviation Safety Agency (EASA) [5] dictate that for field measurements of propeller-driven airplanes weighing at most $8618kg$, the microphone must be "a 12.7 mm diameter pressure type" with a protective grid and mounted an inverted position $7mm$ above and parallel to a ground plate, which must be white, circular, metal, $40cm$ in diameter, $2.5mm$ thick, and placed horizontally and flush with the ground with no cavities underneath. Although these documents share many similarities, where they differ is in their prescription of where the microphone should be mounted above the ground board. ICAO Annex 16 requires the microphone be located "three-quarters of the distance from the centre to the edge" [10], whereas EASA guidelines require the microphone be located "15 cm from the centre of the circular plate" [5]. Even within the ICAO Annex 16 document, there contains different standards concerning the microphone and ground board configuration, which are dependent on the test article or vehicle. For example, the requirements for subsonic jet airplanes are that the microphone be oriented as closely as possible to the calibrated direction and placed approximately $1.2m$ above the ground, differing from the previous standard prescribing ground-mounted microphones. Even more standards

are available, such as ISO 5305:2024 [13] and IEC 61400-11 [11], which prescribes similar requirements for unmanned aircraft systems (UAS) and wind turbines.

Differences aside, these regulations are all meant to provide a standard ground board configuration to keep acoustic experiments easily repeatable and comparable. Different tests may be conducted with different environmental conditions, which would impact the sound measured by a microphone in the absence of a ground board due to non-repeatable or uncontrolled environmental conditions, especially the substance on which the microphone is grounded, since this will affect the behavior of acoustic reflections. However, employing a consistent microphone and ground board configuration may mitigate these effects and make two tests repeatable and comparable despite their differences. Furthermore, many people have worked to and are working to both further our understanding of standard ground board behavior and develop improved methods and ground board designs to mitigate common inherent issues with ground board usage, such as reflection and edge scattering effects.

Anderson et al. [2] investigated the effects of both microphone configuration relative to the ground board as well as the material on which the ground board is placed. Specifically, they tested two microphone configurations: the standardized inverted microphone and an embedded microphone flush with the top surface of the ground board. They also tested three surface substrates: free air, sand, and plywood. Furthermore, they opted to use a ground board constructed from a high-density plastic material instead of metal. This was done to reduce weight and make it easier for experimentalists to work with the ground board.

First, they performed normal impedance tube testing from $100Hz$ to $3000Hz$ on different sand depths, the plywood, and the ground board. Four different sand depths went through normal impedance tube testing: $0.0254m$, $0.0762m$, $0.152m$, and $0.229m$, and they found little to no correlation between sand depth and reflectivity. The plywood and ground board were simply supported to isolate their impedance on air, and both materials were found to be perfectly reflective within the entire frequency range. This result challenges both the requirement for no cavities beneath the ground board and the requirement for the metal ground board material. Acoustic performance was also gathered for the plywood and ground board on top of three inches of sand, the depth of which was chosen due to its balance between relatively uniform reflectivity within the frequency range and its ease of implementation. Anderson et al. found that the ground board maintained essentially perfect reflectivity across the entire spectrum, whereas the plywood exhibited lower reflectivity, increasing until about $1000Hz$, where it reaches 100% reflectivity.

With the ground board reflectivity characterized, Anderson et al. moved on to anechoic testing of acoustic performance at different azimuth and incidence angles, microphone configurations, and simulated ground conditions. They tested azimuth angles of 0° (microphone rotated further from source) and 180° (microphone rotated closer to source), incidence angles ranging from 5° to 90°, inverted and flush embedded microphone configurations, and two simulated ground conditions: the ground board atop three inches of sand alone, and the ground board atop a plywood sheet atop three inches of sand. They provided frequency

spectra of these tests with reference to free-field measurements. In summary, they found that most incidence angles resulted in the ground board performing within $\pm 3dB$ of free-field, except at shallower grazing angles, where edge diffraction effects were more prominent, caused destructive interference, and thus resulted in the ground board microphone measuring significantly lower sound than free-field. They also found that the plywood acted as an acoustically hard surface, effectively extending the edge of the ground board and dampening the diffraction effects. This caused the ground board's acoustic performance to tend closer towards free-field measurements at all incidence angles and both microphone configurations. They also found that at an azimuth angle of 180°, edge diffraction effects were enhanced especially at shallower incidence angles since there is less ground board between the microphone and the source compared to a 0° azimuth angle. Microphone configuration comparisons are less conclusive. At most frequencies, both microphone configurations performed similarly, but around the end of their frequency range (above $10000Hz$), the frequency spectra for the inverted microphone rolls down due to its limited response range. However, the opposite occurs for the embedded microphone, where its frequency spectra rolls upwards, the cause of which was not concluded by Anderson.

Lastly, Anderson et al. further investigated the effects of azimuth angles but in the outdoor environment. Two microphones were set up very closely alongside each other and measured both level and descending flight conditions. They find that both orientations result in very similar sound pressure levels above $30Hz$ (less than $0.1dB$ difference), and differences below $30Hz$ are attributed to external effects separate from the flight noise. They admit that their field investigations were limited, and suggest that further experimentation should be conducted to verify if this conclusion can be generalized.

Willshire and Nystrom [22] conducted similar ground board research as Anderson, investigating different microphone positions and orientations. Willshire and Nystrom tested flush, inverted, and lain microphone configurations in comparison to a free-field reference microphone at various incidence angles. Additionally, they tested the effects of shrouds, which are essentially attachments to the edges of the ground board to round the edges with the intent to reduce diffraction effects. These shrouds were made of a fiberglass material and of a one-quarter ellipse shape with a $0.305m$ major diameter, $0.203m$ minor diameter, and $0.635cm$ thickness. These were fitted to the $1.22m$ square, $0.635cm$ thick aluminum ground board.

Willshire and Nystrom conducted these tests in an anechoic chamber with an anechoic limit of $150Hz$ to $50000Hz$, and they analyzed the spectra into third-octave bands with center frequencies from $315Hz$ to $20000Hz$. First, regarding the shrouds, they found that the diffraction effects were reduced as intended and expected. The ground board with shrouds performed much better than without shrouds at isolating the pressure doubling effect, essentially making the ground board behave more similarly to an infinite plate. These measurements were taken using a flush-mounted microphone, which serves as a reference for the other microphone configurations.

Multiple inverted microphone heights were tested, which were normalized on the microphone diameter. They tested height-to-diameter ratios of 0.125, 0.25, 0.5, 0.75, 1, and 2. For each height-to-diameter ratio except for 2, the spectra agreed very well with the flush-mounted microphone under $4000Hz$, where as agreement was only good for a height-to-diameter ratio of to under $1000Hz$. Above these frequencies, destructive interference emerged from the difference in directed and reflected path distances. The primary dip in SPL due to destructive interference is largely a function of geometry, and Willshire and Nystrom found that the frequency at which this dip occurs is shifted to lower frequencies when the height-to-diameter ratio is increased. They also found that at the lower height-to-diameter ratios, constructive interference was experiences, which they attribute to structural resonance. The lying microphone configuration was also tested and found to closely match with the flush-mounted microphone up to about $4000Hz$. Above this frequency, the finite size of the microphone starts to have an effect, where its geometry causes differences in path distance and some destructive interference can be seen as well, especially at shallower incidence angles. The purpose of this investigation was to find a ground board design that would minimize the impacts of edge diffraction and ground impedance. Notice that especially in the new Airbus design, although there are a few axes of symmetry, it is not fully circularly symmetric, which was done such that any edge effects would be less likely to coalesce at the center of the ground board.

Focusing more on the ground board geometry, Blandeau and Bousquet [4] investigated two different ground board shapes, both experimentally and numerically. The two geometries are shown in Figure 1.2.

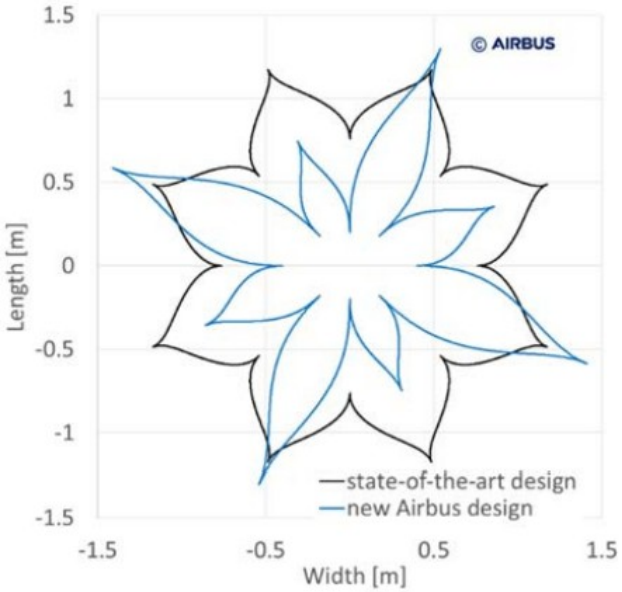

Figure 1.2: Daisy Plate and New Airbus Ground Board Designs. Adapted from Blandeau and Bousquet [4]

The numerical portion of their investigation used Airbus's ACTIPOLE code, which is based on a boundary element method. They considered factors such as ground absorption, acoustic ray incidence angle, and ground board thickness. The detailed mesh formation process is described by Abboud et al. [1], but importantly, factors used were two ground impedance models (one for low absorption to model grass, and one for moderate absorption to model beech wood), incidence angles from 20° to 160° at every 1° increment, three ground board thicknesses ($10mm$, $75mm$, and $150mm$), and a frequency range from $50Hz$ to $5000Hz$. Blandeau and Bousquet present their results in terms of excess attenuation EA as defined in Equation 1.1

$$EA = 20\log_{10}\left(\frac{p_{total}}{p_{incident}}\right) \tag{1.1}$$

where p_{total} is the actual sound pressure measured by the microphone in the presence of a ground board and $p_{incident}$ is the sound pressure measured by a microphone in the absence of a ground board. For a perfect reflector causing pressure doubling, the excess attenuation would be $EA = 20\log_{10}(2) \approx 6dB$.

ACTIPOLE results revealed that for ground board thicknesses of $75mm$ and $150mm$ and both ground impedance models, the new Airbus design is significantly less sensitive than the daisy plate design with respect to incidence angle and frequency, especially in the combined incidence angle and frequency ranges of 75° to 105° from $200Hz$ to $800Hz$, and 45° to 75° from $400Hz$ to $1000Hz$. Slightly less sensitivity in the new Airbus design can also be observed with incidence angles lower than 25° and frequencies higher than $1000Hz$, but Blandeau and Bousquet note that the differences between the two designs are too insignificant and could be due to model limitations regarding shallow incidence angles. Additionally, above $1000Hz$, both designs have little sensitivity on incidence angle, especially at source positions near directly above the ground boards. The lower sensitivity of the new Airbus design means easier experimental repeatability and more consistent excess attenuation corrections.

For a ground board thickness of $10mm$ and low ground absorption, both ground board designs behaved very similarly to a perfect reflector, with an excess attenuation of about $6dB$ throughout the entire observed frequency range. Blandeau and Bousquet conservatively suggest that under these conditions, subtracting $6dB$ from field measurements with either ground board design may be adequate to correct for the ground board effects and obtain an accurate estimation of the free-field, but admit that further experimentation should be conducted to verify this.

Blandeu and Bousquet's experimental investigation occurred outdoors near the Toulouse-Blagnac Airport in France. Three microphones were used: one reference microphone, one microphone mounted to a daisy plate ground board, and one microphone mounted to a new Airbus ground board. The microphone was lain horizontally on the ground, and both ground board microphones were mounted vertically flush to the center of the ground board surface. The daisy plate ground board and new Airbus ground board were located about

$20m$ and $30m$ from the reference microphone, respectively. The ground impedance around each microphone was also measured.

A few limitations of their experimental setup include close proximity to trees, which makes measuring the lower incidence angles difficult and inaccurate. There were more differences between the two ground boards other than their shape: their distances to the reference microphone, and their color (which would cause different temperature gradients above either plate). Furthermore, the different mounting schemes for the reference microphone and ground board microphones caused inaccuracies at higher frequencies. All of these factors create difficulties for accurate corrections and estimating excess attenuation.

The measurements of both ground board microphones were compared to each other and their own numerical predictions from ACTIPOLE. Similar to the ACTIPOLE results, the experimental results suggest that the new Airbus design has a better acoustic response than the daisy plate design due to reduced destructive interference patterns. However, the daisy plate design yielded experimental results that agree with ACTIPOLE results better than the new Airbus design, likely due to the previously stated limitations.

Blandeu and Bousquet conclude with recommendations for ground board usage in field measurements of aircraft noise. These recommendations include mounting the ground board flush to the surrounding surface, using a ground surface with low absorption, and mounting the microphones vertically such that the membrane is flush with the plate. Additionally, they suggest the new Airbus design over the daisy plate design and suggest improved experiments to further characterize the behavior of the new Airbus design.

To provide an alternative computational model to ACTIPOLE and Abboud et al. [1], Kingan et al. presents another model based on boundary element method [14]. Commonly, the ground surrounding the ground board is modeled as a finite plane, resulting in difficulties regarding edge diffraction off the finite ground plane. Kingan et al.'s formulation models the ground as an infinite impedance plane to avoid these issues. The derivation and theoretical development of this model is outside the scope of this discussion, but ultimately, SPL on the entire surface of the ground board can be calculated for both finite-thickness and zero-thickness ground boards. Side view schematics of these situations are shown in Figure 1.3, which are adapted from Kingan et al. [14].

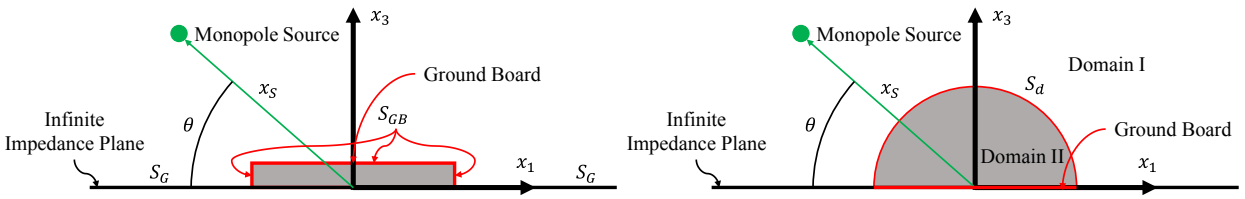

(a) Finite-Thickness Ground Board Schematic. (b) Zero-Thickness Ground Board Schematic.

Figure 1.3: Ground Board Simulation Schematics, Adapted from Kingan et al. [14]

In Figure 1.3, x_S is the distance from the origin to the monopole source, θ is the elevation

angle to the monopole source, S_G is the ground surface, and S_{GB} is the ground board surface.

This new model was evaluated through MATLAB, and for validation, was compared against COMSOL Multiphysics finite element method solutions. Validation revealed excellent agreement between the new boundary element method and the COMSOL finite element method for both finite-thickness and zero-thickness ground boards.

Simulations were executed for $10mm$ thick, $0.4m$ diameter circular ground boards at frequencies of $1000Hz$, $2500Hz$, and $5000Hz$, incidence angles of 30°, 60°, and 90°, and on top of surfaces with an impedance corresponding to grass, sand, and asphalt. Results are also shown in terms of excess attenuation as calculated in Equation 1.1 on the upper surface of the ground board. For all conditions, Kingan et al. found that the excess attenuation may have large fluctuations, $6dB \pm 4dB$, over short distances. These variations are likely caused by constructive and destructive interference patterns from edge diffraction effects. Contour plots were also produced to observe combined effects of frequency (from $50Hz$ to $5000Hz$ with 4 points per one-third octave band resolution) and incidence angle (from 5° to 90° in 1° increments) on the excess attenuation for various ground surfaces. Again, large variations are observed in the frequency spectra, especially for frequencies above about $1000Hz$ and incidence angles above 10°. Unsurprisingly, variations are reduced for ground substrates with higher impedance. Additionally, the same contour plot was generated for a ground board flush with the ground, which resulted in slightly reduced variations in excess attenuation than a $10mm$ thick ground board under the same conditions. Line spectra were generated for various incidence angles (30°, 50°, 70°, and 90°) to more closely observe the effect of thickness. It is clear that at every incidence angle, the zero-thickness ground board resulted in reduced excess attenuation compared to the $10mm$ thick ground board.

Kingan et al. applied their new boundary element method model to the new Airbus design from Blandeau and Bousquet [4]. Kingan et al. considered this ground board design at $10mm$ thickness on top of a ground surface with grass-equivalent impedance at frequencies of $100Hz$, $500Hz$, $1000Hz$, and $2500Hz$, and incidence angles of 30°, 60°, and 90°. Contour plots were generated at every combination of these frequencies and incidence angles to show excess attenuation variation on the upper surface of the ground board. Some similar trends are observed with this design compared to the circular ground board, but most importantly, the variation in excess attenuation at the center of the new ground board design is much lower than the circular ground board, corroborating Blandeu and Bousquet's results [4]. Line spectra were generated for an observer at the center of the ground board at all three incidence angles, which shows that the excess attenuation varies at most by $6dB \pm 1dB$. This improved performance compared to the circular ground board is likely due to the reduced symmetry and therefore reduced constructive and destructive interference at the center of the ground board.

Validation of Kingan et al.'s boundary element method with COMSOL Multiphysics finite element method as well as agreement with Blandeau and Bousquet's numerical and experimental results [4] suggest that this new model is successful, robust, and avoids the unwanted

edge diffraction effects of the ground surface.

This review of the ground boards is especially important for the analysis of outdoor acoustic experiments where microphones are mounted on top of a ground board. In Chapter 3, a similar experiment will be presented that aims to further understand the behavior of circular wooden ground boards with different microphone mounting configurations and source incidence angles, especially the configuration and incidence angle used to measure propeller noise in the outdoor field test presented in Chapter 4.

1.2.3 Broadband Rotor Noise Predictive Capabilities

Currently, there exist many broadband rotor noise prediction methods, ranging from pure analytical mathematical analogies to semi-empirical models to computational fluid dynamics (CFD) solutions. Each have their costs and benefits, including accuracy, scope, and computation time. Importantly, these methods allow for a good baseline and initial UAM design without the hassle of having to set up large tedious physical experiments.

One example of a CFD prediction method is provided by Dr. Sicheng Li and Dr. Seongkyu Lee, who developed a model named UCD-QuietFly [16]. UCD-QuietFly results are limited to turbulent boundary layer trailing edge noise and does not account for BWI or TIN. This model uses a combination of blade element momentum theory (BEMT), XFOIL's boundary layer analysis, and another empirical wall pressure spectrum model developed by Dr. Lee and Dr. Jessica Shum [15]. These three models generate parameters that can be input into a set of equations derived from Amiet's power spectral density (PSD) formulation for a rotor blade section given an observer position [16]. Furthermore, other rotor parameters were considered, including but not limited to tip Mach number, rotor radius, collective pitch, blade twist, and chord length.

UCD-QuietFly was validated against experimental data from one airfoil trailing edge noise case and two rotor trailing edge noise cases. For the single airfoil case, a $0.4m$ chord, $1m$ span NACA0012 airfoil was used considering $53m/s$ freestream velocity. The model aligned with the experimental data well within $\pm 3dB$, suggesting the validity of this method. For the two rotor configurations, both used NACA0012 airfoils with 2 blades, but one with a $6.71m$ radius at 0.67 tip Mach number, and the other with a $8.5m$ radius at 0.47 tip Mach number. Note that these conditions are more representative of a helicopter, but the methods are later validated for smaller propellers closer to UAM vehicles. For the smaller of the rotor cases, UCD-QuietFly provided a better prediction than previous methods, and for the larger rotor, UCD-QuietFly failed to predict all minor features thought to be caused by sources not captured by this model, such as trailing edge bluntness noise. This model with a single rotor and single observer costs about $60s$ to compute, and scales directly with the desired number of observers to calculate. Further analysis was conducted to observe SPL trends independently with rotational speed, collective pitch, blade pitch, chord length, rotor radius, and inflow velocity. Attenuation and directivity effects were also observed in horizontal and

vertical planes.

Dr. Lee and Dr. Li further expanded UCD-QuietFly to consider trailing edge bluntness noise and stall noise, which was then used to predict broadband noise from a multi-rotor configuration, more similar to a UAM vehicle than a helicopter [17]. Small-scale validation was performed against an APC Slow Flyer 11×4.7 propeller, a $0.014m$ radius two-bladed drone propeller, operating at $3600RPM$, $4200RPM$, and $4800RPM$. Similar to their previous study, UCD-QuietFly captures the broadband noise of this propeller within about $\pm 3dB$, especially in the mid- to high-frequency ranges, or around $3000Hz$ to $30000Hz$.

UCD-QuietFly was then used to generate predictions for three vertical take-off and landing (VTOL) vehicles: a quadcopter design, a side-by-side design, and a lift and cruise design. The major parameters of these vehicles are summarized in Table 1.1.

Table 1.1: VTOL Vehicle Design Parameters. Adapted from Lee and Li [17].

Parameter	**Quadcopter**	**Side-by-Side**	**Lift and Cruise**
Rotor Radius (m)	3.99	4.54	1.52
Total Rotors	4	2	8
Blades Per Rotor	3	4	2
Rotational Speed (RPM)	400	353	1120

Broadband noise was calculated for these parameters at altitudes between $15.2m$ to $457m$ and compared to background noise from different types of communities, the loudest being freeway and the quietest being rural. For the quadcopter design at $457m$, the broadband noise is louder than the rural background noise above about $700Hz$ and freeway background noise above about $6000Hz$. Compared to the other VTOL designs, the quadcopter generated about $2dB$ more broadband noise than the side-by-side design throughout the entire frequency spectrum ($100Hz$ to $10000Hz$), and less low-frequency broadband noise and about the same high-frequency broadband noise as the lift and cruise design. This interesting relationship was studied further by varying the number of rotors on a lift and cruise design VTOL, while maintaining propeller tip speed and total swept area constant, which means a decrease in rotor radius with an increase in number of rotors. The effect of increasing the number of rotors resulted in quieter low-frequency noise and louder high-frequency noise. Li and Lee attribute this trend to the combination of two factors: the decrease in rotor radius causes a decrease in low-frequency noise, while the increase in number of rotors increases the high-frequency trailing edge noise.

Dr. Lee provides another broadband rotor noise prediction model, this time developed with Dr. Hyunjune Gill [8]. Contrastingly to the previous CFD model built primarily upon theory, this method uses a gene expression programming method to build upon earlier empirical models, such as the Schlegel-King-Mull spectrum model [20] or Pegg model [19], specifically targeting limitations in scope. The mechanism behind gene expression programming is beyond the scope of this discussion, and further detail can be found in Gill and Lee's

documentation [8]. The content of interest is their broadband noise spectrum model, named the Gill-Lee Spectrum Model (GLSM), based off hundreds of empirical datasets from drones and propellers. These datasets consider parameters including Mach numbers between 0.08 to 0.67, blade loading mostly around $0.1 \leq \frac{C_T}{\sigma} \leq 0.18$, observer distance from 6 to 25 times the rotor radius, and elevation angles throughout $-90°$ to $90°$. Furthermore, contour plots show that the majority of the datasets operate with Mach numbers between 0.2 and 0.4 and normalized thrust coefficients between 0.14 and 0.18, and that little to no datasets contain low tip speeds with low thrust or high tip speeds with low thrust. The equation and set of parameters are shown in Equations 1.2 and 1.3, respectively.

$$SPL_{1/3} = \frac{f_0 \Delta_{GL}^{0.6}}{[f_3 \Delta_{GL}^{f_4} + f_5]^{f_6} + [f_7 \Delta_{GL}]^{f_8}} \tag{1.2}$$

$$\begin{aligned}
\Delta_{GL} &= S_t - (f_1 \log_{10} C_T + f_2 \log_{10} \sigma) \\
S_t &= \frac{fc}{V_t} \\
c_\sigma &= \frac{\sigma \pi R}{N} \\
f_0 &= 10 \log_{10} \left(V_t^{7.84}\right) \\
f_1 &= \sigma \\
f_2 &= 0.9 M_t \sigma \left(M_t + 3.92\right) \\
f_3 &= 1 \\
f_4 &= 1 \\
f_5 &= -2M_t^2 + 2.06 \\
f_6 &= -C_T M_t \left(C_T - \sin|\theta_0| + 2.06\right) + 1 \\
f_7 &= C_T \\
f_8 &= 4.97 C_T \sin|\theta_0| \left(1.5 \frac{s_0}{R} M_t - \frac{s_0}{R} + 15\right)
\end{aligned} \tag{1.3}$$

Here, c_σ is the solidity-weighted chord length, on which the Strouhal number S_t is based. C_T is the thrust coefficient, σ is the rotor solidity, V_t is the blade tip velocity, R is the rotor radius, N is the number of rotor blades, M_t is the blade tip Mach number, and s_0 and θ_0 are the observer distance and angle, respectively. The observer position is defined in Figure 1.4.

Notice that Equation 1.2 produces a third-octave band SPL. The conversion from narrowband PSD to third-octave band spectra is quite simple, but the reverse is technically and theoretically impossible. However, an approximation can be done assuming the spectra are smooth. This is simply calculated as a ratio of the third-octave band frequency bin width to the narrowband frequency resolution, as shown in Equation 1.4.

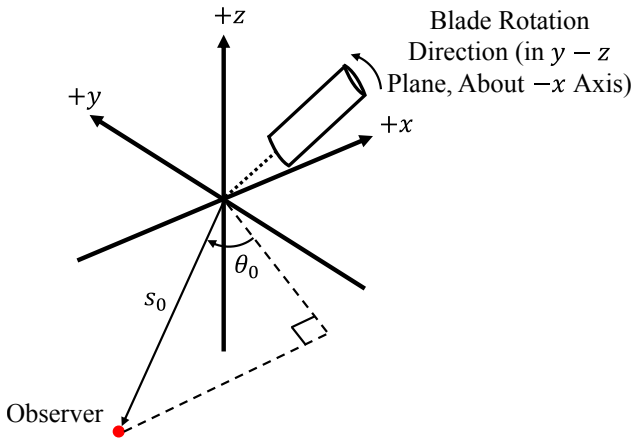

Figure 1.4: Propeller Coordinate System, and Observer Distance and Elevation Angle Definitions. Adapted from Gill and Lee [8], Adjusted for Document Consistency.

$$SPL_{Narrow} = SPL_{1/3} - 10\log_{10}\left(\frac{\Delta f_{1/3}}{\Delta f_{Narrow}}\right) \tag{1.4}$$

This conversion shifts the levels such that the GLSM output is comparable to narrowband spectra. This will be done in Chapters 4 and 5 to compare with experimental propeller noise narrowband spectra with a frequency resolution of $8Hz$.

1.2.4 Broadband/Tonal Noise Decomposition

Propeller noise experiments inevitably capture both broadband and tonal noise components. The tonal component is less difficult to model and predict than the broadband component, so the current focus is to further understand broadband noise, specifically at different scales and test facilities in this document. In order to experimentally investigate the broadband noise component, it needs to be isolated from the tonal noise component. To do so, these components can be extracted from the time-series data by recording rotational speed data synchronously with the acoustic pressure data.

First, consider a pressure time history associated with the noise of a rotor. The sound generated by this rotor will have both random and deterministic components, which are directly related to broadband and tonal components, respectively. Furthermore, the deterministic components will be directly linked to the rotation of the propeller and its blades, which is why it is necessary to record the propeller rotation signal synchronized with the acoustic pressure.

Often times, the blade rotation is recorded by a simple voltage impulse signal from a laser diode tachometer, usually a square or sawtooth wave. Sometimes, these impulses

resemble the passage of each blade, and other times, they resemble an entire rotation of the propeller. In this discussion and unless otherwise stated, the impulse will be a square wave and treated as the detection of a full propeller rotation. A sample generated square wave and corresponding pressure time history is shown in Figure 1.5.

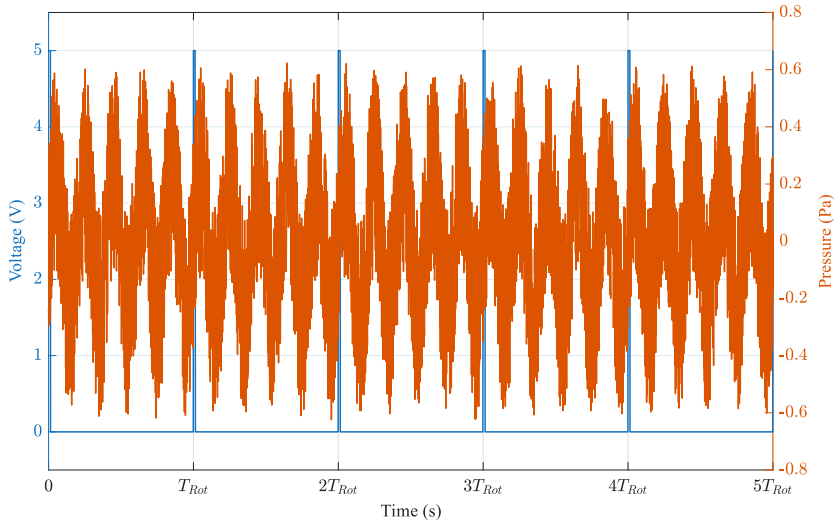

Figure 1.5: Voltage Impulse Signal and Pressure Time History Over 5 Propeller Rotations.

The left axis shows the square wave impulse signal in blue, and the right axis shows the acoustic pressure time history in orange. Note that this square wave has a duration of $0.00002s$ and indicates one full propeller rotation, so a time interval between impulses of about $0.0146s$ would indicate a rotational speed of $4096RPM$. Also note that Figure 1.5 only shows the signal for a five rotations of the full $10s$ time series data. This is so that the individual features are more visible, but the full $10s$ was still calculated so that the next steps also yield visible results. Furthermore, the pressure time history was generated by simply adding random noise to a sine wave. The sine wave has a frequency of 5 times the square wave impulses to represent a propeller with 5 blades and an amplitude of $0.25Pa$. The random noise has an amplitude of about $0.375Pa$. These parameters were chosen to mimic the behavior of random noise generated by a 5-bladed rotor operating at $4096RPM$.

With these raw voltage and pressure signals, the first step in separating the broadband and tonal noise components is to calculate the average pressure fluctuation caused by each rotation. This is done by dividing the full pressure time history into segments based on the impulse signal and averaging them. The number of segments considered in the average will depend on the sampling period and the rotational speed. In practice, the propeller's rotational speed will not be perfectly constant throughout the entire sampling period, so the time between each impulse would vary. This can be dealt with by creating a standard grid in time with a very fine resolution, fitting the raw pressure time history divisions to the size of this standard grid, and interpolating the raw data onto this grid. The result of this

process is a single curve representative of the average pressure fluctuations within the period of a single propeller revolution. An example of this result is shown in Figure 1.6, which was calculated from the data shown in Figure 1.5

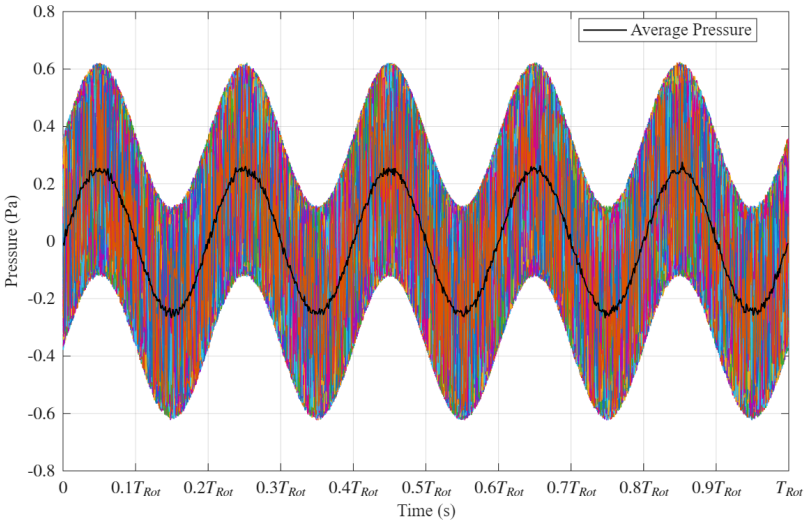

Figure 1.6: Pressure Averaged Over Each Propeller Rotation.

The colored curves are the raw pressures divided by the impulse signal and interpolated onto the standard grid, and the black curve represents the average of all of the colored curves. Clearly, this process begins to recover the original sine curve used to define the full pressure time history. Taking this a step further, this can be used to extract the tonal component, since this process will average out the random noise and retain only the noise associated purely with the propeller rotation.

To obtain the broadband component, this rotation-averaged pressure can be expanded to the full sampling period by simply repeating this wave by the number of segments or averages. This expanded tonal pressure signal can be subtracted from the total sound pressure to obtain the broadband pressure signal. This subtraction is shown in Figure 1.7.

Again, this process appears to separate the deterministic sine wave from the additional random noise. These deterministic and random components expanded to the full sampling period can be spectrally processed as usual, and the following result is shown in Figure 1.8

Notice here that the most dominant tone is what the simulated blade passage frequency (BPF) would be, which for a 5-bladed propeller at $4096RPM$ is approximately $341.33Hz$. The rest of this signal appears to be dominantly broadband, which is nearly a flat line on this spectrum. This is because this randomly generated data is very nearly truly random, and would thus register on a spectrum as white noise. Also notice that the total spectrum is nearly invisible, hidden behind either the tonal or broadband spectrum at most frequencies, except near where the two components intersect. Of course, this result is for a known signal

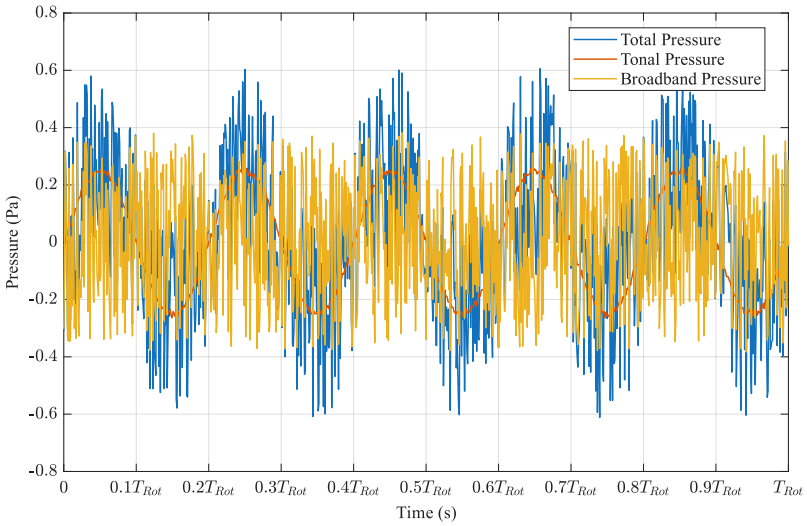

Figure 1.7: Broadband Pressure Obtained By Subtracting Tonal Pressure From Total Pressure.

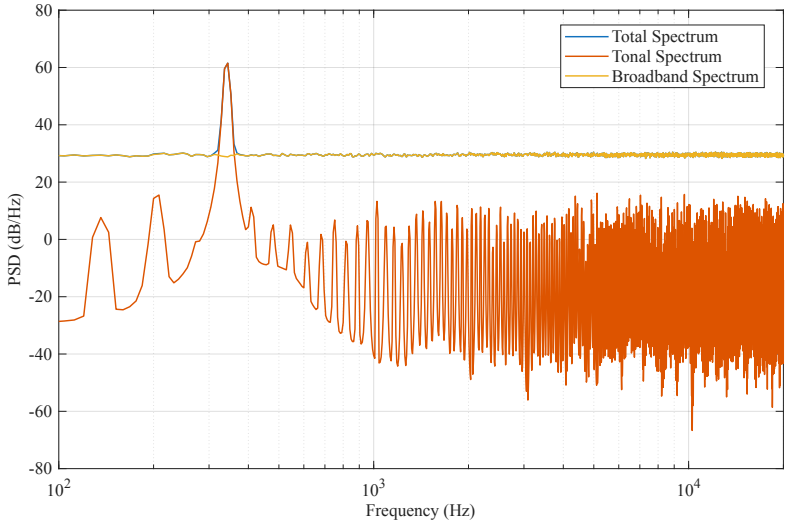

Figure 1.8: Total, Tonal, and Broadband Spectra.

with a prescribed amplitude, frequency, and random noise variation. Although the process will be the same, the result will be much more interesting for true rotor noise gathered experimentally.

1.3 Objectives

Ultimately, propeller noise is a rapidly growing area of research interest, especially for the development of UAM vehicles. Difficulties involving initial design phases, specifically with relating indoor and outdoor acoustic experiments, demand practices to keep these experiments consistent, repeatable, and comparable. There currently exist a number of standards to keep outdoor acoustics research consistent, as well as models to predict propeller noise behavior, but as with everything, there is always room for improvement. Therefore, the objectives of this document are generally to help further understand the effects of scale and testing facility and suggest good research practices for analyzing data acquired in uncontrolled environments, specifically by:

- characterizing the response of a $1m$ diameter, $6mm$ thick plywood ground board in an anechoic chamber at various source incidence angles and microphone positions on top of the ground board
- characterizing the effects of scale, pitch angle, and turbulence trips on broadband noise
- correlating wind velocities with outdoor propeller noise over time to develop methods to improve comparability between different test conditions using the same test article
- evaluating the differences between acoustic experiments conducted indoors and outdoors and comparing both to prediction models

Chapter 2

General Facilities and Instrumentation

This chapter describes the facilities and general instrumentation used in each experiment. Much of the instrumentation is common to all experiments. For example, the same microphone model is used in multiple experiments. Therefore, these common instruments are described here to reduce redundancy.

2.1 Durham Hall Anechoic Chamber

The Durham Hall Anechoic Chamber has an inside workable space of $5.4m \times 4.1m \times 2.4m$ and an anechoic lower limit of $100Hz$. The interior is completely covered in triangular anechoic foam wedges. The flooring is made of a thin wireframe material above the foam wedges, which allows for people to walk around the chamber without stepping on the foam on the ground. There are a number of fixed metal shafts placed beneath the wireframe floor as well as metal rings fixed to the ceiling of the chamber. These structures provide rigid mounting surfaces for any instrumentation the experimentalist may want to use. The locations of these shafts and rings are fixed, which is an important design consideration if different mounting configurations are desired. An image of the interior of the anechoic chamber is shown in Figure 2.1.

2.2 Drone Park

The Virginia Tech Drone Park is an outdoor facility where students and professional engineers can experiment with drones and related technology. The Drone Park measures $91.4m$ long and $36.6m$ wide and features an $25.9m$ tall netted enclosure. An image of the Drone Park is depicted in Figure 2.2. The facility is also equipped with electrical outlets on each netting support. Additionally, https://montgomery.weatherstem.com/vtdronepark WeatherSTEM provides both real-time and historical weather data specifically at the Virginia Tech Drone Park, including but not limited to ambient pressure, temperature, and relative humidity.

Figure 2.1: Durham Hall Anechoic Chamber. Photo Credit: Muhammad Raza.

Figure 2.2: Virginia Tech Drone Park Image. Photo Credit: Erica Corder (https://eng.vt.edu/magazine/stories/fall-2018/if-we-build-it-they-will-come.html).

The Drone Park is located approximately half a kilometer from the nearest highway when measured linearly and ignoring any terrain or minor roads. The close proximity to busy roads may present an issue when trying to take acoustic measurements. However, this was worked around by collecting background noise information before collecting the target propeller acoustics data. Chapter 4 will describe this process and show general background noise behavior in more detail.

2.3 Virginia Tech Subsonic Modular Anechoic Research Tunnel (VTSMART)

Virginia Tech also features an anechoic open-jet wind tunnel, named the Virginia Tech Subsonic Modular Anechoic Research Tunnel (VTSMART). This facility is located indoors at the Virginia Tech Swing Space (VTSS). A schematic image of the VTSMART has been adapted from Jeremiah Whelchel's dissertation [21] and shown in Figure 2.3.

This tunnel is powered by a Twin City QSL axial fan, allowing the tunnel to operate at a maximum freestream speed of about $40m/s$. The flow passes through a 90° muffler and acoustic baffles to reduce undesired acoustic interference. The flow is then straightened and cleaned by Kevlar screens within the settling chamber to reduce turbulence. The flow then moves through a $7.8:1$ contraction section to the $0.762m \times 0.762m$ inlet of the open jet test section. Within the test section, acoustic foam wedges are placed on the walls, ceiling, and floor to mitigate acoustic reflection effects, obtaining an anechoic lower limit of $420Hz$. Finally, the $1.27m \times 1.27m$ outlet exits the flow to the rest of the room.

2.4 Techsburg Propeller

The propeller used in all experiments was provided by Techsburg Inc., and detailed descriptions about their propellers can be found from their corresponding Vertical Flight Society Forum (VFS) conference papers [6] [7]. For each propeller blade, Techsburg used an airfoil design for propellers from Martin Hepperle and fabricated via injection molding with nylon reinforced with carbon fiber. The blade thicknesses vary from 20% to 14% to 10% of the chord from the root to midspan to tip, respectively. Twist and chord distributions are available from the Techsburg's VFS conference papers and also shown in Figure 2.4.

A clamshell hub design with pitch inserts allowed for manually adjustable blade pitches. Two of these hubs were fabricated to allow for a five-blade propeller at both $0.457m$ and $0.914m$ diameter scales. The two scales are geometrically similar, and both have a solidity of $\sigma = 0.195$. The original design condition for the five-blade $0.914m$ diameter propeller is about $233.5N$ of thrust at an air density equivalent to that at $610m$ operating at $2000RPM$. The entire propeller assembly was balanced using an Aces Systems 2020HR balancer. Computer-aided design (CAD) line drawings of an individual blade and the entire propeller assembly are shown in Figure 2.5, an image of the clamshell hub, 7° pitch insert, and assembled $0.914m$ propeller are shown in Figure 2.6.

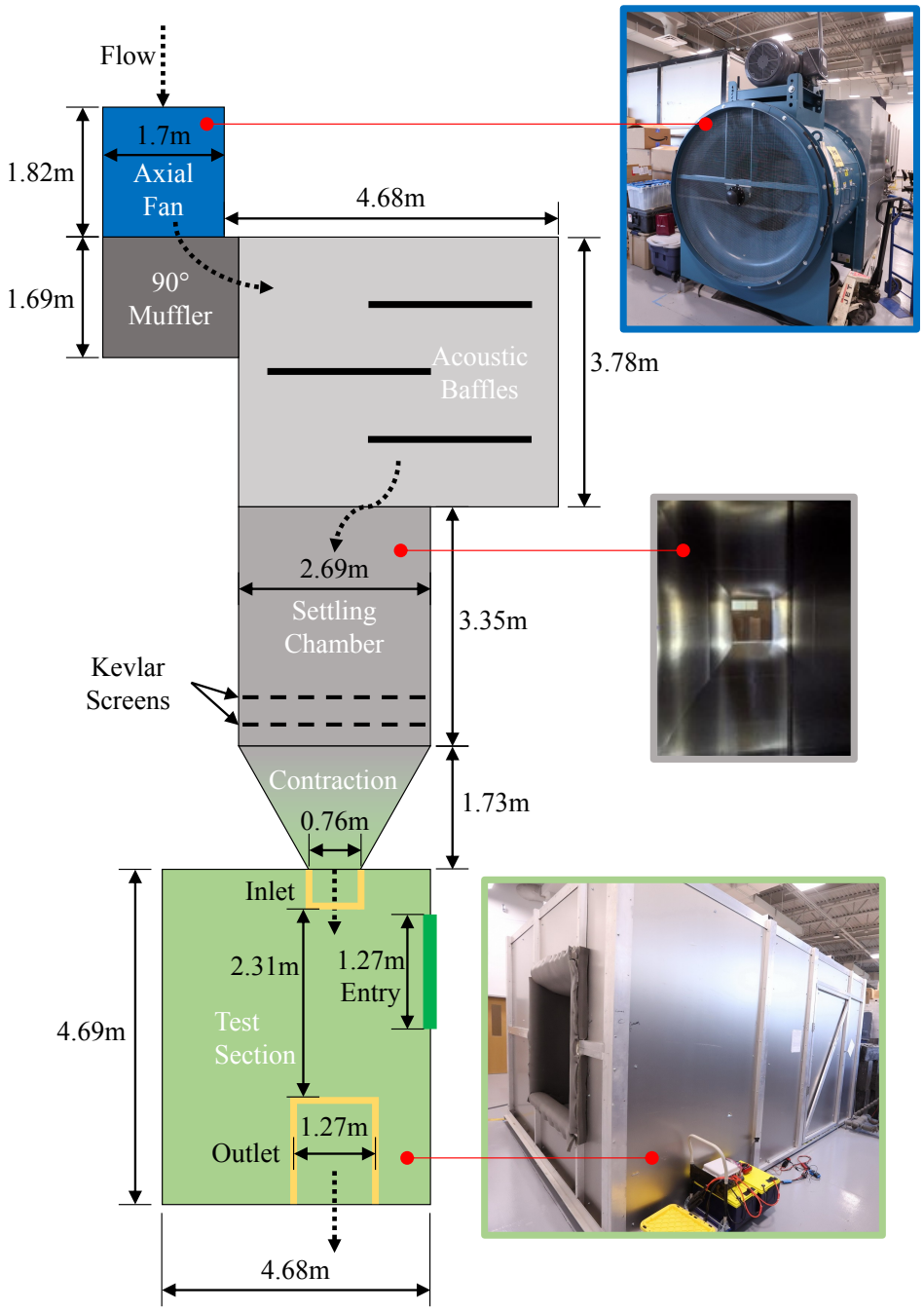

Figure 2.3: Schematic of VTSMART. Adapted from Whelchel [21]

2.5 Brüel & Kjær Instruments

The acoustic measurement devices, specifically the microphones and data acquisition systems (DAQs), were purchased from Brüel & Kjær (B&K).

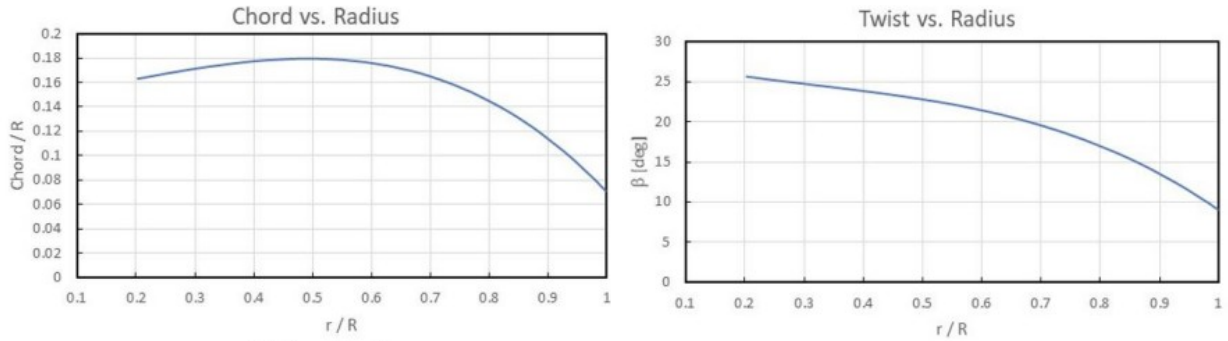

(a) Chord Versus Radius Distribution. (b) Twist Versus Radius Distribution.

Figure 2.4: Chord and Twist Distributions. Adapted from [6] [7].

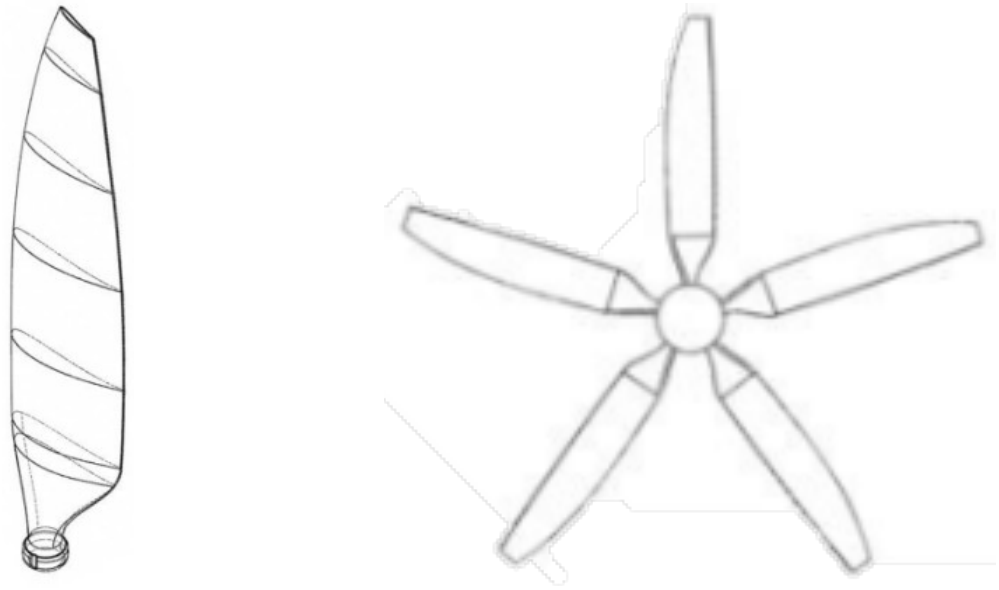

(a) Line Drawing of Individual Blade. (b) Line Drawing of Propeller Assembly.

Figure 2.5: CAD Line Drawings. Adapted from [6].

The microphones used are B&K Type 4190 microphones. These microphones are half an inch in diameter and are accurate within a frequency range of $6.3Hz$ to $20000Hz$. They have a nominal sensitivity of $50mV/Pa$ and dynamic range of $14.6dB$ to $146dB$, although each microphone is individually calibrated, which is provided to the purchaser and encoded into the device itself. Each microphone is directly connected to a Family 2669 preamplifier, which is capable of measuring between $3Hz$ and $200000Hz$, well above the capabilities of the microphone. The Family 2669 preamplifiers have a male LEMO 0B 7-pin connection, and a variety of corresponding female cables are available.

These cables directly plug into B&K DAQs, the model of which are Type 3050-A-060-R.

(a) Clamshell Hub and 7° Pitch Insert.

(b) 5-Blade 0.914m Diameter Propeller.

Figure 2.6: 0.914m Diameter Propeller, Clamshell Hub, and Pitch Insert. Photo Credit: Jon Fleming.

These DAQs have interchangeable front panels depending on the preferred connector type, and each front panel has six input channels. For the experiments discussed in this document, a female LEMO 0B 10-pin front plate will be used, and a corresponding cable will be used to connect the preamplifier to the DAQs. Furthermore, these DAQs have a frequency range from DC input to 51.2kHz and communicate with the control computer via ethernet cable. The data from the DAQs are collected through Brüel & Kjær's software "BK Connect Front-end Setup" and "BK Connect", which are capable of exporting time-series files into many workable formats. An image of the B&K instruments is shown in Figure 2.7.

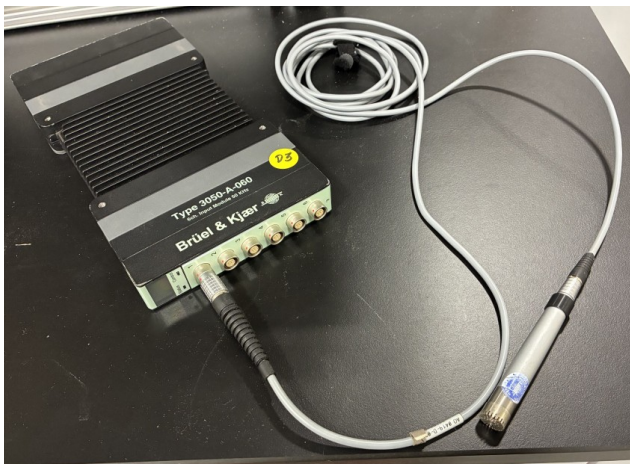

Figure 2.7: Brüel & Kjær Type 3050-A-060-R DAQ and Type 4190 Microphone.

These time-series data will be spectrally processed to the frequency domain using Welch's method with a Hanning window [3]. The parameters for this analysis are a sampling frequency of $f_S = 65536Hz$, a total sampling period of $T = 32s$, a record length of $n_{Rec} = 8192$ samples, a record overlap of $q = 0.5$ (or 50%), and a reference pressure of $p_{Ref} = 20 \times 10^{-6} Pa$. This reference pressure is generally regarded as an aeroacoustic standard and roughly corresponds to the lower threshold of human hearing. A single-sided power spectral density (PSD) can be calculated directly from the spectra and reference pressure, as shown in Equation 2.1.

$$PSD = 10 \log_{10} \left(\frac{G_{pp}}{p_{Ref}^2} \right) \tag{2.1}$$

where G_{pp} is the autospectrum of the mean-square-pressure. Additionally, overall sound pressure level (OASPL) can be calculated by integrating the spectrum within a desired frequency range to obtain a single value to represent the general sound power of the acoustic signal. On the other hand, a spectrogram can be generated to observe the behavior of the frequency spectrum distributed over time. This can be easily done by a slight modification to the calculation of the PSD. Rather than calculating the spectrum of each record and averaging all of the spectra, each record's spectrum can be treated as a representation of the frequency content at that instant in time. A contour plot can be generated with these time-varying spectra, with time on the x-axis, frequency on the y-axis, and PSD on the contour. A time-varying OASPL can be calculated from the spectrogram by integrating the spectrum of each record within a desired frequency range to represent the general sound power of each record.

2.6 Miscellaneous

There are a number of other individual pieces of equipment used as well, the description of which would not warrant their own section, so they are collectively described in this section.

For some calibrations, a white noise signal was required. This white signal was generated from an NTi Audio MR2 Minirator function generator. This function generator is capable of generating many different signals, such as sinusoids, pink noise, and white noise. It has a maximum output level of $8dBu$, so it was connected to an amplifier before the speaker. This amplifier is a Crown XTi 4000, rated for $1600W$ output at 2Ω for each of two channels. The speaker is a very simple magnetic dipole attached to a wooden block for ease of mounting. This speaker is connected to the amplifier via $14AWG$ copper speaker cables. Images of these components are shown in Figure 2.8.

Recall that the B&K DAQs communicate via ethernet cable and can measure up to six microphones simultaneously. Therefore, if more than six simultaneous microphone measurements are desired, multiple DAQs must be connected to an ethernet hub. The ethernet hub

(a) Minirator MR2 Function Generator.

(b) Crown XTi 4000 Amplifier.

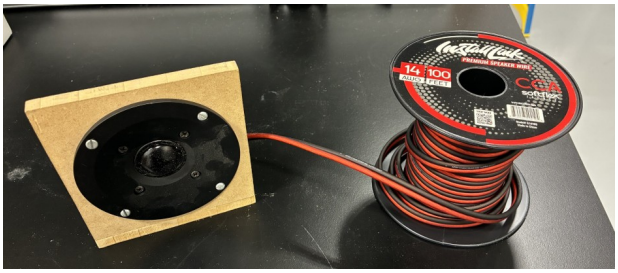

(c) Speaker and Speaker Wire.

Figure 2.8: General Sound Output System.

used was a NETGEAR Prosafe GS108 Gigabit Switch, which has eight $1000Mbps$ channels. This switch can connect directly to the control laptop, on which the BK Connect software will automatically synchronize the DAQs. An image of this ethernet hub is seen in Figure 2.9.

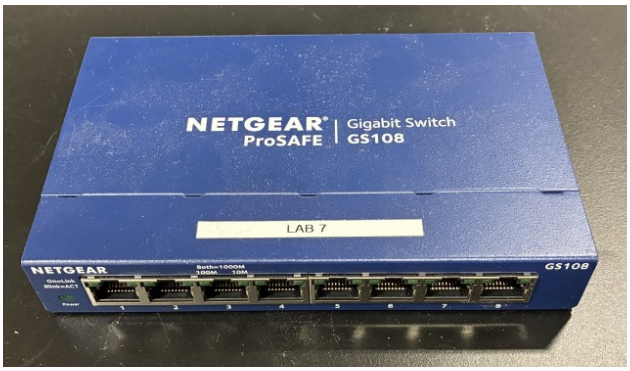

Figure 2.9: NETGEAR Prosafe GS108 Gigabit Switch.

To spin the propeller, a T-Motor U15-II KV100 with a T-Motor Flame 200A electronic speed controller (ESC) was used. This motor can obtain a maximum no-load nominal speed

of $9480RPM$ and can supply up to $9940W$ for $180s$. The motor can handle up to $167A$ continuously for $180s$ and requires between 12S and 24S LiPo batteries. The ESC can supply $200A$ continuously and up to $240A$ for $10s$, and is compatible with 6S to 14S LiPo batteries.

For the sensing side during the propeller noise experiments at both indoor and outdoor facilities, a load cell and a tachometer are required to detect loads, specifically thrust and torque, and rotational speed. To measure the former, an ATI Omega 85 six-component force and torque sensor was used with the US-105-185 calibration. This model and calibration combination has a force range of $470N$ in the F_x and F_y directions and $930N$ in the F_z direction, and a torque range of $21N\text{-}m$ in all T_x, T_y, and T_z directions. Its resolution is $0.086N$ for F_x and F_y, $0.103N$ for F_z, $3.93N\text{-}mm$ for T_x and T_y, and $2.35N\text{-}mm$ for T_z. To measure the propeller speed, a laser tachometer detected the passage of a single marked blade. Additionally, a Trisonica LI-550 ultrasonic anemometer was used to obtain wind velocity data at $10Hz$. Images of the motor, ESC, and anemometer are shown in Figure 2.10.

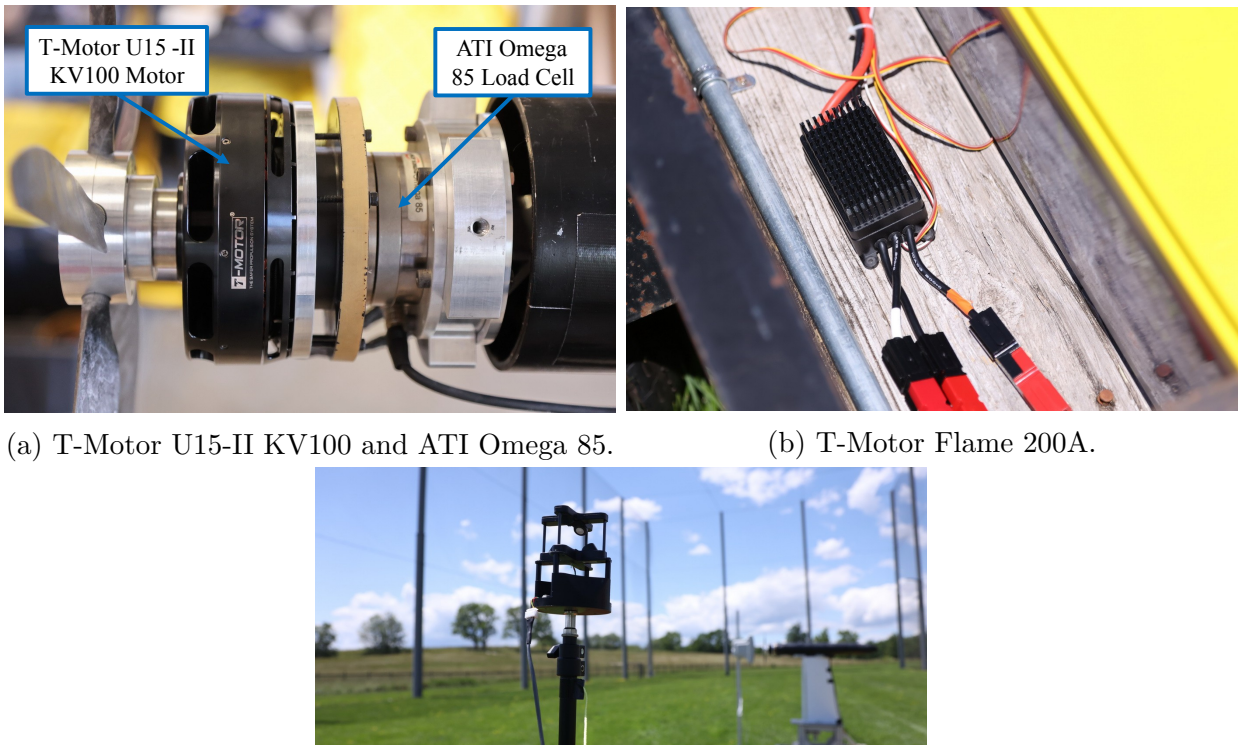

(a) T-Motor U15-II KV100 and ATI Omega 85.

(b) T-Motor Flame 200A.

(c) Trisonica LI-550.

Figure 2.10: General Rotor Control and Measurement System. Photo Credit: Jon Fleming.

2.7 Ground Boards

The ground boards used in the following experiments are made of plywood in the shape of a thin circular disk. They each measure and $1m$ in diameter and $6mm$ thick and are painted red. An image of one such example is shown in Figure 2.11 with a measuring tape for size reference. Note that the surface of these ground boards are not perfectly smooth, which is just a result of the material and paint limitations. A small hole marks the geometric center of each ground board.

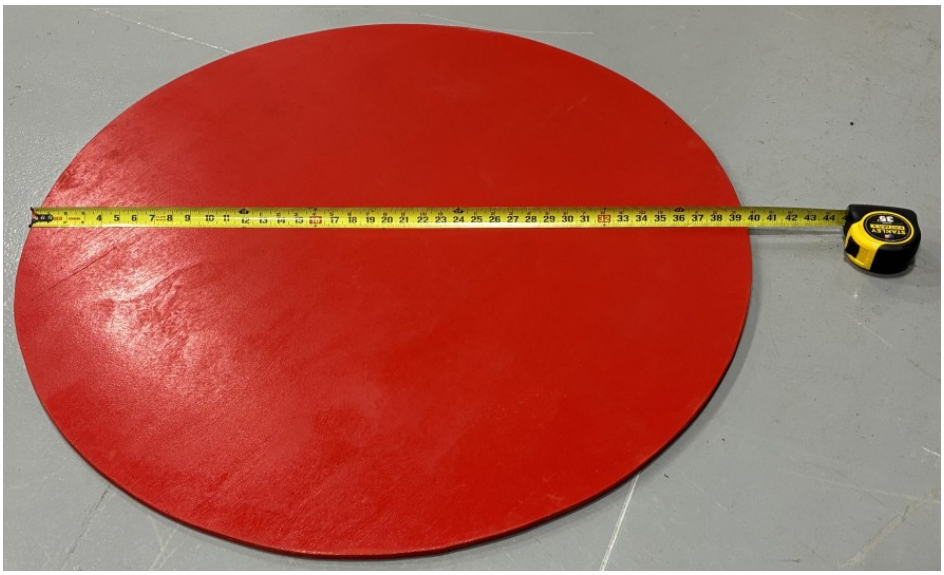

Figure 2.11: Plywood Ground Board.

2.8 Uncertainties

It is also important to note the calculation and measurement uncertainties to understand how reliable the results are. First, spectral uncertainty, a type of calculation uncertainty, in the acoustic measurements is dependent on the magnitude of the fluctuations and the number of records [9] [3]. This dependence is shown in Equation 2.2.

$$\delta\left[G_{pp}\right] = \frac{2G_{pp}}{\sqrt{N_{Rec}}} \tag{2.2}$$

Note that the "δ" in this equation is not the Dirac delta function, but rather indicates the uncertainty of the variable within the brackets. Also, N_{Rec} indicates the number of records within the entire sampling period. The number of records is dependent on the sampling period, sampling frequency, and record overlap, as shown in Equation 2.3.

$$N_{Rec} = \left\lfloor \left(\frac{\frac{f_S T}{n_{Rec}} - 1}{1 - q} \right) \right\rfloor + 1 \tag{2.3}$$

Note that the "$\lfloor\ \rfloor$" indicates the "floor" operator, which rounds the interior value down to the nearest integer. Recall from Section 2.5 that these parameters are $f_S = 65536Hz$, $n_{Rec} = 8192$ samples, $T = 32s$, and $q = 0.5$, which results in $N_{Rec} = 511$ records. The uncertainty in decibel levels can then be found by Equation 2.4.

$$\delta\left[PSD\left(G_{pp}\right)\right] = \frac{1}{2}\left(10\log_{10}\left(\frac{G_{pp} + \delta\left[G_{pp}\right]}{p_{Ref}^2}\right) - 10\log_{10}\left(\frac{G_{pp} - \delta\left[G_{pp}\right]}{p_{Ref}^2}\right)\right) \tag{2.4}$$

This can be used with a sample propeller noise spectrum to calculate an uncertainty that can be used to represent the uncertainty of all propeller noise spectra. This was calculated for a particularly louder propeller noise spectra to obtain a worst-case uncertainty, which resulted in approximately $\delta\left[PSD\left(G_{pp}\right)\right] \approx \pm 0.385dB$. This uncertainty is outweighed by the measurement uncertainty of the B&K Type 4190 microphones, specifics of which are provided with each microphone. These uncertainties are nominally $\pm 1dB$ from $5Hz$ to $10000Hz$ and $\pm 2dB$ from $3.15Hz$ to $20000Hz$. Thus, the uncertainty in the spectra in a controlled environment should be treated as $\pm 1dB$ from $100Hz$ to $10000Hz$ and $\pm 2dB$ from $10000Hz$ to $20000Hz$. These uncertainties are less valid in a chaotic outdoor environment, where the measurements are not necessarily stationary, so it will instead be estimated at $\pm 2dB$ throughout $100Hz$ to $20000Hz$, which was approximated by observing the variations among repeated acoustic measurements during the outdoor experiment.

The uncertainty of the flow speed in the VTSMART is also important, and this can be found by propagating base measurement uncertainties and the sensitivity of the flow speed to a perturbation of each measurement to the calculation of the flow speed. For example, consider an arbitrary result X dependent on variables x_1, x_2, and x_3, each of which is directly measured and therefore has their own measurement uncertainties (perhaps provided by instrumentation manufacturers or obtained through other methods) $\delta\left[x_1\right]$, $\delta\left[x_2\right]$, and $\delta\left[x_3\right]$. The sensitivity of X on the three variables is directly related to its partial derivatives $\frac{\partial X}{\partial x_1}$, $\frac{\partial X}{\partial x_2}$, and $\frac{\partial X}{\partial x_3}$. The total uncertainty of the result $\delta\left[X\right]$ can then be approximated by a root-sum-square in Equation 2.5.

$$\delta\left[X\right] = \sqrt{\left(\delta\left[x_1\right]\frac{\partial X}{\partial x_1}\right)^2 + \left(\delta\left[x_2\right]\frac{\partial X}{\partial x_2}\right)^2 + \left(\delta\left[x_3\right]\frac{\partial X}{\partial x_3}\right)^2} \tag{2.5}$$

The derivation of a generalized form of Equation 2.5 can be found in the textbook by Glegg and Devenport [9]. In general, the flow speed of a wind tunnel is calculated using Equation 2.6.

$$U_\infty\left(T_a, p_d, p_a\right) = \sqrt{\frac{2RT_a p_d}{p_a}} \tag{2.6}$$

Here, U_∞ is the freestream flow speed, R is the gas constant, T_a is the ambient temperature, p_d is the dynamic pressure, and p_a is the ambient pressure. The gas constant is assumed to be at a constant $287\frac{J}{kgK}$ and thus its uncertainty will be considered negligible. The uncertainty of the flow speed can then be calculated by substituting these specific variables into Equation 2.5 to obtain Equation 2.7.

$$\begin{aligned}\delta\left[U_\infty\right] &= \sqrt{\left(\delta\left[T_a\right]\frac{\partial U_\infty}{\partial T_a}\right)^2 + \left(\delta\left[p_d\right]\frac{\partial U_\infty}{\partial p_d}\right)^2 + \left(\delta\left[p_a\right]\frac{\partial U_\infty}{\partial p_a}\right)^2} \\ &= \sqrt{\left(\delta\left[T_a\right]\sqrt{\frac{Rp_d}{2T_a p_a}}\right)^2 + \left(\delta\left[p_d\right]\sqrt{\frac{RT_a}{2p_d p_a}}\right)^2 + \left(\delta\left[p_a\right]\left(-\sqrt{\frac{RT_a p_d}{2p_a^3}}\right)\right)^2}\end{aligned} \tag{2.7}$$

The dynamic pressure is obtained using a Setra Model 239 pressure transducer, which has range of $\pm 3730Pa$ and uncertainty of $\pm 0.073\% FS$ ($\pm 2.72Pa$). The total temperature and total pressure were obtained using a Newentor Weather Station, which has an accuracy of $1K$ in temperature and $3390Pa$ in pressure. Additionally, typical values for the dynamic pressure, total temperature, and total pressure were about $11.9Pa$, $295K$, and $94100Pa$, respectively. Using this information with Equation 2.7 gives:

$$\begin{aligned}\delta[U_\infty] &\approx \sqrt{\left((1K)\left(0.00785\frac{m}{sK}\right)\right)^2 + \left((2.72Pa)\left(0.194\frac{m}{sPa}\right)\right)^2 + \left((3390Pa)\left(-0.0000246\frac{m}{sPa}\right)\right)^2} \\ &\approx 0.536m/s\end{aligned} \tag{2.8}$$

These values were obtained with the wind tunnel operating at nominally $4m/s$, but this uncertainty analysis shows that the true wind tunnel speed lies anywhere within about $4m/s \pm 0.536m/s$.

The measurement uncertainty of the ATI Omega 85 load cell is directly provided by ATI. These are nominally 1.5%, 1.5%, 1%, 1.25%, 1.75%, and 1.25% of the full scale load for the F_x, F_y, F_z, T_x, T_y, and T_z components, respectively. For the US-105-185 calibration, this comes out to be $7N$ for F_x and F_y, $9.34N$ for F_z, $0.366N$-m for F_y, and $0.261N$-m for F_x and F_z.

The propeller speed was monitored by a laser diode tachometer, whose uncertainty is greatly outweighed by the human error in controlling the propeller speed. The motor is a

simple DC drone motor controlled manually and generally maintained within about $\pm 2\%$ of the nominal RPM.

The measurement accuracy of the Trisonica LI-550 ultrasonic anemometer is also directly provided by the manufacturer. The accuracy is dependent on the magnitude of the measured wind speed, but for the wind speeds relevant to this project, this anemometer has an accuracy of $\pm 0.2 m/s$.

Chapter 3

Ground Board Characterization Experiment

As previously mentioned in SubSection 1.2.2, knowing the effects of the ground boards is crucial to understanding the relationship between the measured acoustics with the true acoustics. Therefore, careful experimentation was performed in the Durham Hall anechoic chamber to characterize the acoustic behavior of the ground boards.

3.1 Experiment Setup

Shown in Figure 3.1, a mounting bracket was attached to the center of the underside of the ground board, which was mounted to one of the metal struts underneath the wireframe floor inside the anechoic chamber. A speaker as described above in Section 2.6 was mounted to an adjustable thin stand on the wireframe floor and connected to the Crown XTi amplifier, which was in turn connected to the Minirator MR2 set to the white noise generator function. The Minirator MR2 was also connected to a B&K Type 3050-A-060-R DAQ to verify the integrity of the white noise signal. This split from the Minirator MR2 is shown in Figure 3.2. Due to the cable length limitations, the amplifier, white noise generator, and accompanying DAQ were kept inside the chamber but distanced away from the speaker, ground board, or microphone as to avoid any possible interference with the experiment. The electronic instrumentation required inside the chamber is shown in Figure 3.3. A B&K Type 4190 microphone was simply lain on top of and at the center of the ground board and pointed toward the speaker. A general overview of the setup within the anechoic chamber, including the speaker, microphone, ground board, and electronic instrumentation, can be seen in Figure 3.4.

Since the computer was kept outside of the chamber, an ethernet cable was fed through the pipe in the wall of the anechoic chamber and connected to the B&K DAQ inside of the chamber. Similarly, the microphone was connected to another B&K Type 3050-A-060-R DAQ located outside of the chamber, separate from the one connected to the Minirator MR2. The second unit was required because the connections for the Minirator MR2 and the B&K microphone required different connectors and therefore different front plates on each DAQ. The two DAQs were synchronized via an ethernet hub, which was directly connected to a

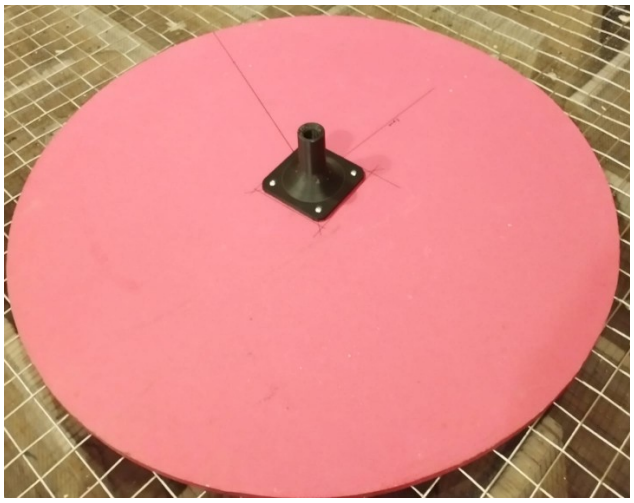

Figure 3.1: Mounting Bracket in the Center of the Ground Board. Photo Credit: Muhammad Raza. Bracket Design Credit: Andrew Single.

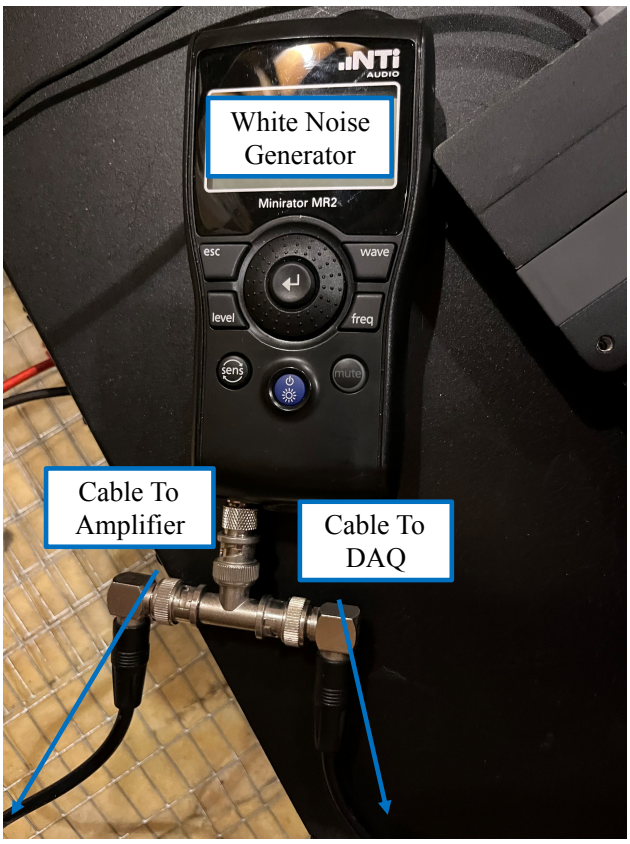

Figure 3.2: Minirator MR2 Cable Split to DAQ and Amplifier.

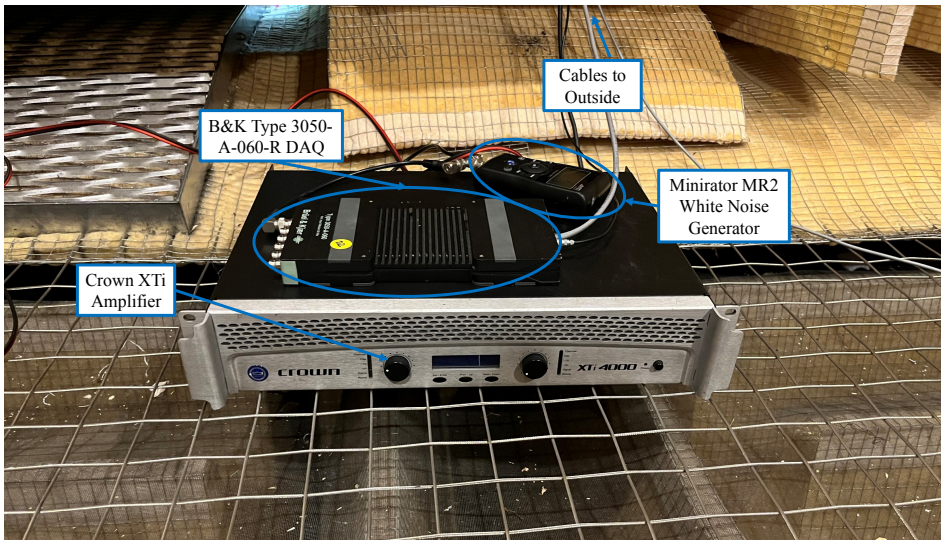

Figure 3.3: Crown XTi Amplifier, B&K Type 3050-A-060-R DAQ, and Minirator MR2 Inside Anechoic Chamber.

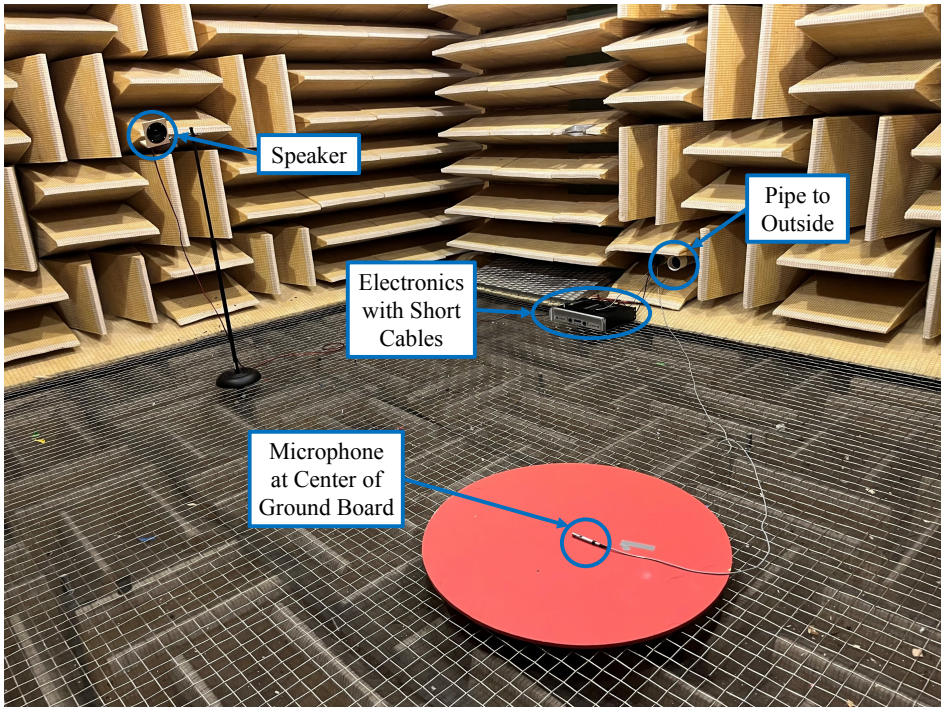

Figure 3.4: General Setup Inside Anechoic Chamber. Speaker at 23° to Microphone Relative to Horizontal, Microphone in the Center of Ground Board.

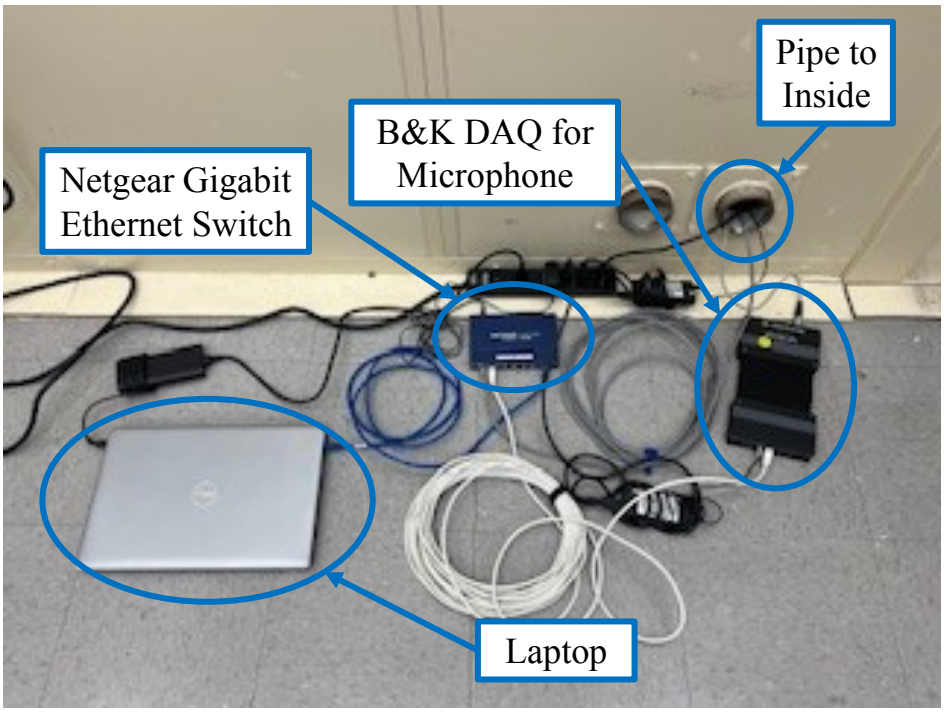

Figure 3.5: Laptop, Netgear Gigabit Ethernet Switch, and B&K Type 3050-A-060-R DAQ Outside Anechoic Chamber

laptop through an ethernet cable, enabling the simultaneous data collection of the input and output systems. The instrumentation outside of the chamber is shown in Figure 3.5.

To test the effects of angle of incidence on the frequency response, the speaker was moved relative to the location of the microphone. As previously stated, a thin stand was used to mount the speaker to the ground; furthermore, clamps were used to mount the speaker to the ceiling rings to reach higher angles. The horizontal and vertical distances to the microphone were measured using a measuring tape, and the angle of incidence was calculated from these measurements.

This process was repeated at each angle of incidence without a ground board, and again with the microphone lain on top of the ground board but located at three-fourths times the radius away from the center. To do this, the mounting strut on the bottom of the ground board also had to be moved to the three-quarter-radius position in order to maintain the distance from the microphone to the speaker. The mounting strut and microphone placed at this position can be seen in Figure 3.6. Careful consideration was taken to ensure that the location of the microphone, not center of the ground board, relative to the speaker was maintained constant for each condition. Additionally, the ground board was oriented such that the larger portion of the ground board was between the microphone and the speaker.

The purpose of repeating the experiment with the microphone placed offset from the center

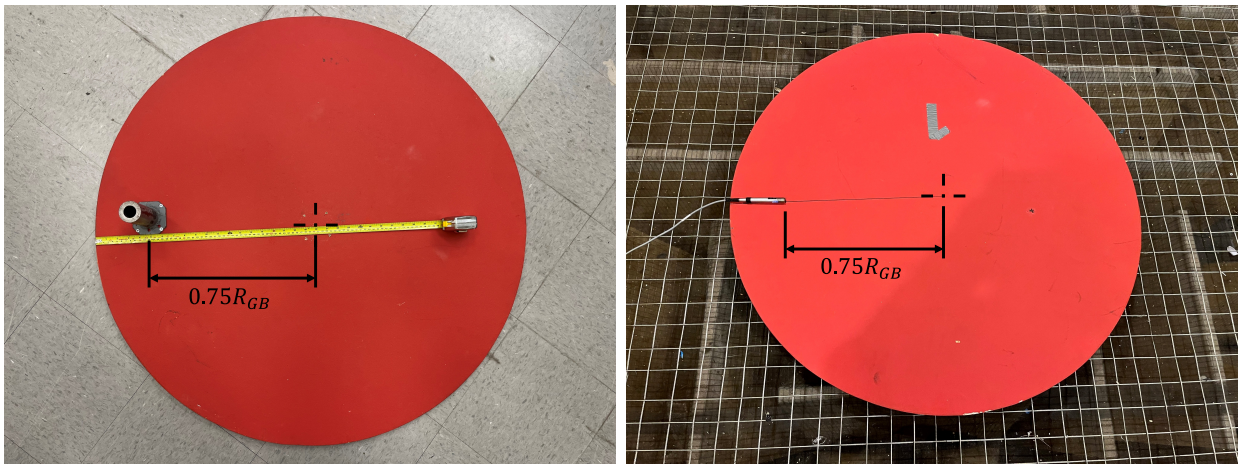

(a) Bottom Side with Mounting Bracket. (b) Top Side with Microphone.

Figure 3.6: Modified Ground Board Mounting for Three-Quarter Radius.

of the ground board was to observe another method to mitigate potential constructive and destructive interference from edge diffraction effects. When the microphone is placed at the center, the distance to the edge of the ground board is the same in each direction, which may result in undesired constructive or destructive interference patterns. When the microphone is placed elsewhere, the distance to the edge is different for each direction, which may avoid these edge scattering effects. Edge scattering effects may yield different effects for different incidence angles, which is another reason multiple incidence angles were tested. A full test matrix is shown below in Table 3.1.

Table 3.1: Ground Board Characterization Test Matrix.

	Source Incidence Angle				
Ground Board Setup	20°	23°	45°	65°	80°
No Ground Board	✓	✓	✓	✓	✓
Microphone at Ground Board Center	✓	✓	✓	✓	✓
Microphone at $0.75R_{GB}$ from Ground Board Center	✓	✓	✓	✓	✓

The condition with no ground board present was treated as a reference and used to calibrate the ground board effects. As with the three-quarter radius mounting, the position of the microphone relative to the speaker was kept constant when the ground board was removed entirely. This was easily done since when the microphone was positioned on top of the ground board, the mounting strut was located directly underneath the microphone, and the microphone was lain on the wireframe floor above the mounting strut. This condition was used as opposed to the white noise signal output directly from the DAQ so that any discrepancies in the white noise generator, amplifier, speaker, or any other system would be neutralized.

3.2 Calibration Method

The effects of the ground board were characterized using calculations performed in the frequency domain, whereby a transfer function was obtained, representative of the frequency response. From the cross-spectral matrix (CSM), the clean signals of both the reference microphone and the ground board microphone were calculated using Equation 3.1.

$$C = \frac{G_{Mic,WN} \times G_{WN,Mic}}{G_{WN,WN}} \tag{3.1}$$

where "C" represents the clean signal, or a correlated signal between the white noise input and the measured microphone response. Also, the "Mic" subscript indicates the microphone signal, and the "WN" subscript indicates the white noise signal, so "$G_{Mic,WN}$" is the cross spectrum between the microphone response and white noise signal, "$G_{WN,Mic}$" is its complex conjugate, and "$S_{WN,WN}$" is the autospectrum of the white noise signal. This clean signal was calculated in order to obtain a cleaner and less noisy autospectrum of the microphone input signal. The calibration transfer function can then be calculated by dividing the clean autospectrum of the reference microphone by the clean autospectrum of the ground board microphone, as seen in Equation 3.2.

$$H_{Cal} = \frac{C_{Ref}}{C_{GB}} \tag{3.2}$$

The difference in power spectral density (PSD) as heard by the microphone on the ground board relative to the reference can then be calculated using the inverse of the calibration transfer function, as shown in Equation 3.3.

$$\Delta PSD = 10 \log_{10}(H_{Cal}^{-1}) \tag{3.3}$$

This is essentially how much louder or quieter the microphone on the ground board detects a source than if the ground board were not present. The calibration transfer function has been defined with the reference microphone divided by the ground board microphone because these ground boards will be used again as per standards [11], and in order to correct for the ground board reflections, the raw microphone measurements will be multiplied by H_{Cal} such that the corrected measurement will represent a more accurate acoustic measurement. A perfect acoustic reflector would result in a constant $6dB$ increase in PSD, so this can be used as a baseline comparison to the ground boards used in this experiment.

3.3 Ground Board Effects

Acoustic pressure data was gathered for 32 seconds at a sampling rate of $65536Hz$. The raw data was collected through the BK Connect software and processed through MATLAB. As previously stated, multiple angles of incidence were tested, which were 20°, 23°, 45°, 65° and 80° as measured relative to horizontal, and repeated for three conditions: one condition with the microphone at the center of the ground board, one condition without the ground board, and one condition with the microphone at three-quarters of the radius of the ground board. The 23° condition was tested because previous measurements of propeller noise performed at the Drone Park used this angle, and future experiments are planned to use the same angle.

The power spectral density (PSD) was calculated for each condition using a reference pressure of $p_{Ref} = 20 \times 10^{-6} Pa$, as per Equation 2.1. A frequency spectrum can then be generated, and comparable conditions can be plotted alongside each other. For example, Figure 3.7 shows the frequency spectra for the speaker at 23° and the microphone without a ground board, the microphone at the center of the ground board, and their corresponding calibration transfer function. The decibel change due to an idealized perfect reflector of $6dB$ is also plotted to visualize the difference from these circular ground boards to a perfect reflector.

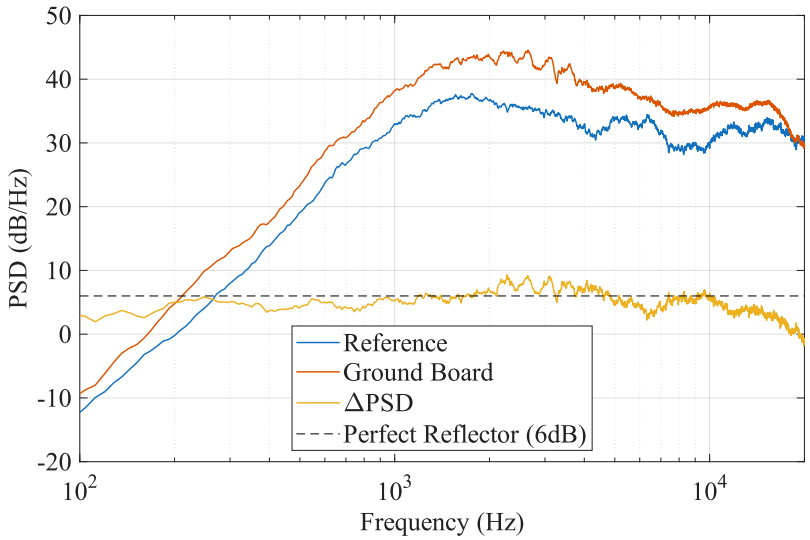

Figure 3.7: Frequency Response of Ground Board at 23° in Comparison to Perfect Reflector Response.

This sort of plot can be generated for each angle and microphone condition, but only the 23° with the microphone at the center of the ground board is shown for brevity. Figure 3.8 shows the calibration transfer function for each condition, again with the $6dB$ baseline

comparison. Figure 3.9 shows the all the calibration transfer functions again, but this time represented as a contour plot to more easily observe and compare fluctuations. To compare the effects of the microphone position, the calibration transfer function with the source at 23° is shown in Figure 3.10.

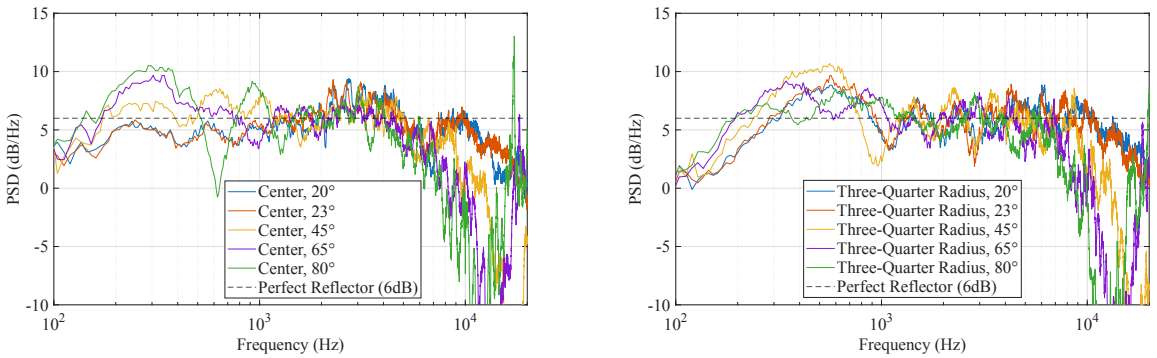

(a) Microphone at Center of Ground Board. (b) Microphone at Three-Quarter Radius.

Figure 3.8: Frequency Response of Ground Board at Each Angle.

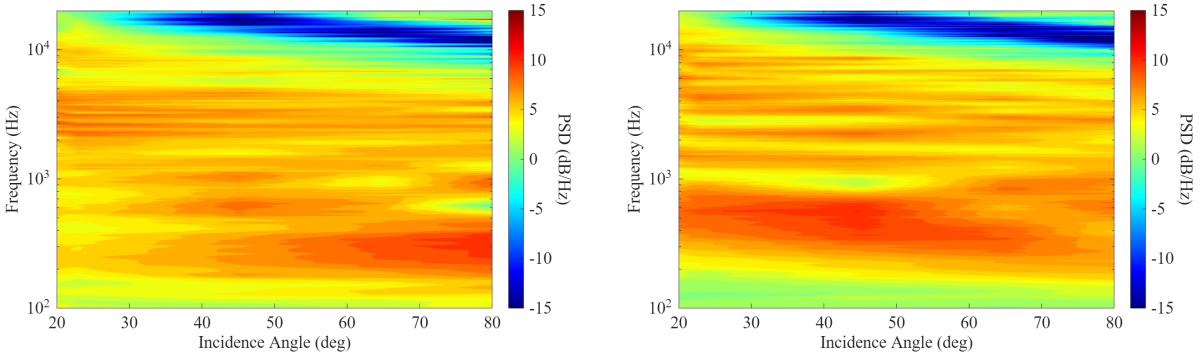

(a) Microphone at Center of Ground Board. (b) Microphone at Three-Quarter Radius.

Figure 3.9: Contour Representation of Frequency Response of Ground Board at Each Angle.

With regards to the microphone positioned at the center of the ground board, it appears that at lower frequencies up to about $2000Hz$, the shallower source angle results in a lower sound pressure magnification. In the mid-frequency range, about $2000Hz$ to $8000Hz$, there seems to be little dependence of ΔPSD on the source angle. Above $8000Hz$, the shallower angles appear to amplify the sound pressure more than the steeper source angles.

With regards to the microphone positioned at three-quarters the radius of the ground board, a similar trend can be observed, however to a much lesser comparative extent. In other words, it appears that a change in source angle has a greater effect on the sound heard by the microphone when placed at the center of the ground board than when placed at

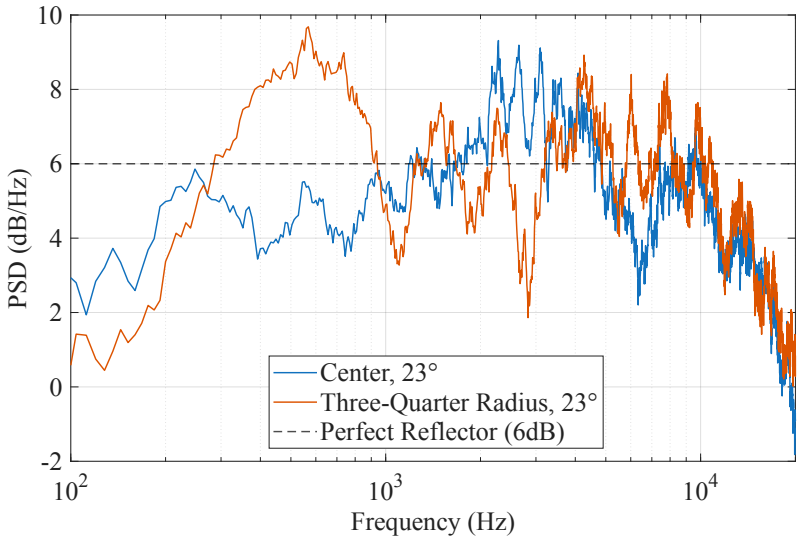

Figure 3.10: Microphone Position Comparison of Ground Board Frequency Response at 23°.

three-quarters the radius of the ground board. However, when observing the contour plots in Figure 3.9, a more nuanced conclusion should be drawn. From about $100Hz$ to $1000Hz$, the offset microphone position seems to have more uniform behavior among each incidence angle. Above $1000Hz$, the center microphone position seems to produce a more consistent frequency response at each incidence angle.

Figure 3.10 shows the effects of the microphone position on the ground board given the source angle of 23°. Analysis shows that the microphone positioned at the center experiences less magnification at most frequencies than when positioned at the three-quarter radius location. Furthermore, the frequency response more closely resembles that of a perfect reflector, within about $\pm 2dB$. This supports the suggestion that the behavior of a microphone placed at the center of the ground board at an angle of 23° can be approximated by that of a perfect reflector, especially between about $200Hz$ and $10000Hz$, where the response fluctuates around $6dB$ within about $\pm 2dB$.

Further research on this topic should aim to test more incidence angles and other microphone configurations. Another interesting aspect would be to test the three-quarter radius microphone position again, but with the shorter portion of the ground board oriented towards the speaker. This may produce different results due to differing edge diffraction effects.

These results can be used in the next experiment, which was performed outdoors and required the use of the same ground boards. Understanding the behavior of these ground boards in an anechoic environment can help predict and correct for the behavior of the ground boards in an outdoor environment on grass. More specifically, these calibration transfer functions can and should be calculated in the upcoming experiments to correct for the ground board reflections and other related effects.

Chapter 4

Drone Park Experiment

The following experiment was performed in conjunction with Techsburg Incorporated at the Virginia Tech Drone Park, which Section 2.2 described in more detail. This experiment aimed to provide broadband noise data at two different scales under many different operating conditions. These conditions included propeller RPM, number of blades, blade pitch, inclusion of turbulence trips, and blade tip drooping. Blade tip drooping is described in more detail by Fleming et al. [7]. A test matrix is shown in Table 4.1 below. This test matrix is not representative of every test condition tested, but excludes conditions that will not be shown in this document. Note that the cells without a checkmark are conditions that were not tested.

Table 4.1: Drone Park Experiment Test Matrix.

		Pitch Angle	7°		9°				
		Turbulence Trips	No	Yes	No			Yes	
Blade Number	**Rotor Diameter**	**Tip Droop** / **RPM**	None	None	None	Medium	Full	None	Full
5	$0.457m$	2400	✓	✓	✓	✓	✓	✓	✓
		2800	✓	✓	✓	✓	✓	✓	✓
		3200	✓	✓	✓	✓	✓	✓	✓
		3600	✓	✓	✓	✓	✓	✓	✓
		4000	✓	✓	✓	✓	✓	✓	✓
	$0.914m$	1200	✓	✓	✓			✓	
		1400	✓	✓	✓			✓	
		1600	✓	✓	✓			✓	
		1800	✓	✓	✓			✓	
		2000	✓	✓	✓			✓	

4.1 Experiment Setup

Techsburg's proprietary propeller design was fabricated at two different scales: one with a diameter of eighteen inches, and one with a diameter of thirty-six inches. Further detail of Techsburg's rotor geometry is described in Section 2.4 and by Fleming et al. [6] [7]. The propeller was attached to a T-Motor U15-II KV100 motor, which was controlled by a T-Motor Flame 200A ESC. The motor was attached to an ATI Omega 85 six-component

F/T sensor to measure the thrust and torque generated by the motor and propeller. These data, specifically thrust coefficient data, are important for calculating the Gill-Lee Spectrum Model (GLSM) broadband noise predictions [8]. A simple laser tachometer was also used to measure the rotational speed of the propeller. This system was mounted within a carbon fiber fairing atop a strut composed of a solid MDF core with a fiberglass wrapping. This strut had a streamlined airfoil shape to reduce aerodynamic and aeroacoustic interference. This strut was placed on a low-profile trailer, resulting in a total elevation of $1.905m$ of the rotor centerline above the ground. This trailer also held four batteries to provide nominally $48VDC$ to the Flame 200A ESC. More information on this mounting configuration is also provided by Fleming et al. [6] [7]. An image of the propeller mounted onto the strut and trailer is shown in Figure 4.1.

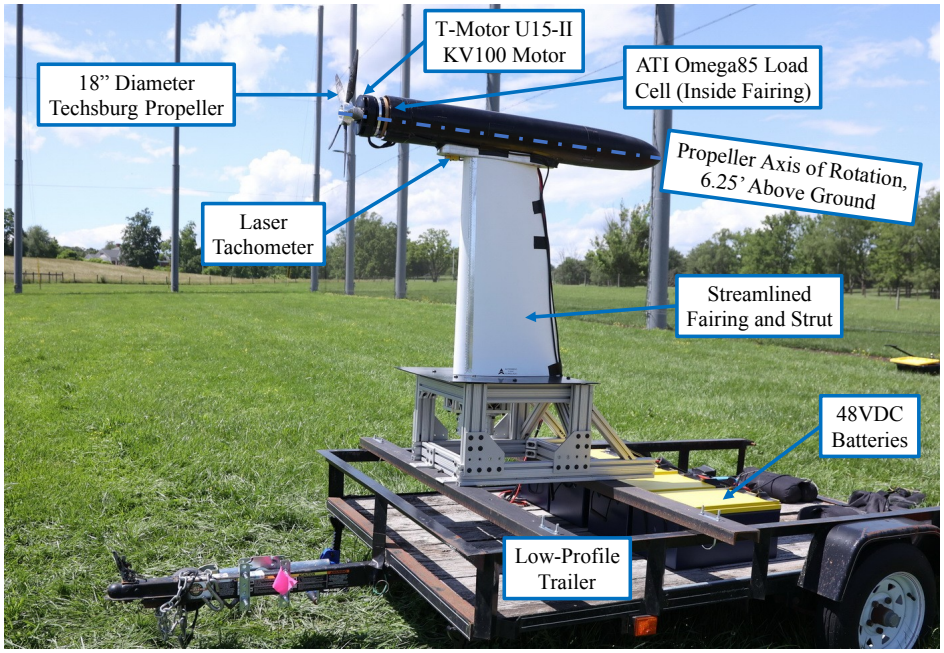

Figure 4.1: Propeller Mounting Structure. Photo Credit: Jon Fleming.

Techsburg also collected wind gust data from a Trisonica LI-550 3-axis ultrasonic anemometer at $10Hz$. This allows for observation of the outdoor environment, specifically considering turbulence and acoustic quiescence. Due to DAQ limitations, these wind data were not acquired synchronously with the acoustic data, but this can still allow for general correlation between the wind and the acoustics, and later will provide comparable conditions to the indoor anechoic wind tunnel experiment.

13 B&K Type 4190 microphones simultaneously collected acoustic pressure data from the propeller. Each microphone was laid on their own ground board in accordance with International Standard IEC 61400-11 [11]. A plumb bob was attached to the rotor plane, which was used to measure a $4.6m$ radius semicircle. The microphones were arranged on this $4.6m$ semicircle around the propeller, evenly spaced by 15° between each microphone.

Again due to DAQ limitations, three B&K 3050-A-060-R DAQs were required to connect all 13 microphones. An ethernet switch as described in Section 2.6 was used to allow for synchronous acoustic data collection. All acoustic data were sampled for $32s$ at a rate of $65536Hz$. Figure 4.2 shows the schematic of the ground board setup, and Figure 4.3 shows an image of the setup.

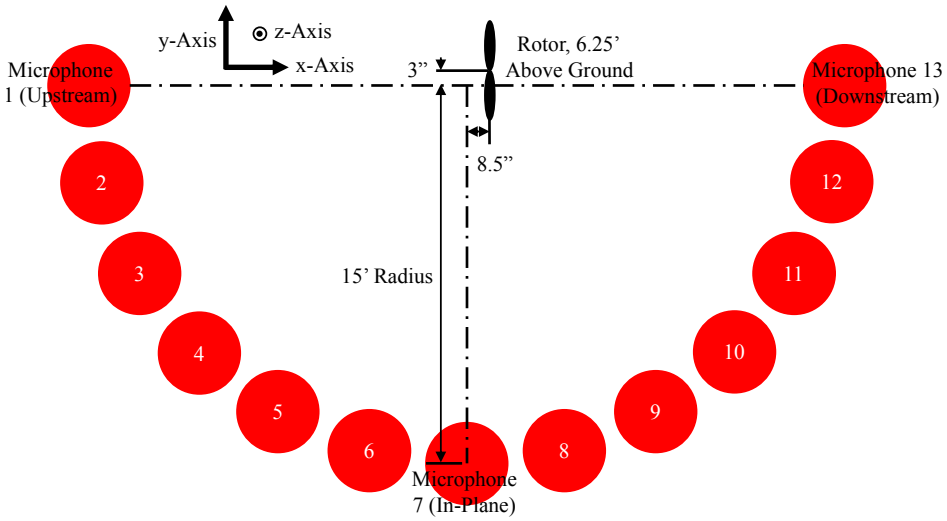

Figure 4.2: Schematic of Ground Board Setup Relative to Propeller.

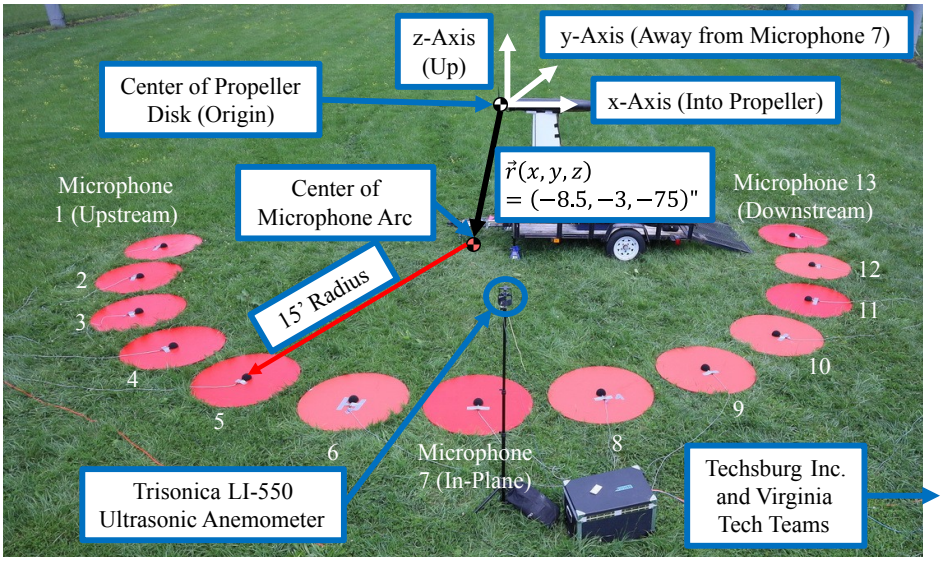

Figure 4.3: Image of General Experiment Setup. Photo Credit: Jon Fleming.

Note the axis and sign conventions of the wind anemometer. The origin is located at the center of the propeller disk; x-axis is aligned with the propeller's axis of rotation and points from Microphone 1 to Microphone 13; the y-axis is aligned with the cross-wind with the

positive direction pointed from port to starboard, and; the z-axis is aligned perpendicular to the ground with the positive direction pointed upwards. These axes will be adopted for the entire discussion of this experiment, which is especially important for noise predictions. Also, note the microphone numbering, starting with 1 at the directly upstream location and increasing in the counter-clockwise direction to 13 at the directly downstream location. The nominal horizontal distance of $4.6m$ from the microphone to the rotor axis and the nominal vertical distance of $1.91m$ from the ground to the rotor results in a nominal distance of $4.95m$ measured from the microphone directly to the rotor center. However, due to practical limitations, the rotor was not placed in the exact center of the semicircle, and was instead placed $0.216m$ closer to Microphone 13 and $0.0762m$ further from Microphone 7. This discrepancy is shown in the schematic in Figure 4.2, but note that it is only roughly to scale, and the discrepancies are exaggerated for visibility.

The Techsburg and Virginia Tech teams arrived at the Drone Park facility at approximately 8AM on 29 May 2024 to begin this experiment setup, and experimentation was ready by the afternoon on the same day. Data were taken until the end of the day, and carried on until the end of 30 May 2024. The dates of experimentation are provided so that atmospheric conditions (such as pressure, density, and temperature) can be cross-referenced.

4.2 Results

A series of methods were used to analyze the data. First, the full pressure time histories were compared to the background noise measurements to ensure they had a significant signal-to-noise ratio (SNR). Second, since the microphones were lain on top of an acoustically hard surface, the spectra had to be corrected for ground board reflections. Next, the wind anemometer data were used to approximate smaller windows of time from the full time series when the wind and environmental conditions were favorable, which was considered to be a small (approximately $1.75m/s$) inflow into the propeller. Observing fluctuations in the time-varying OASPL and spectrograms show a clear relationship between the inflow velocity and noise between about $2000Hz$ and $6000Hz$. Spectral analysis was then performed on these corrected and sequestered time windows, which yielded a more accurate representation of the true rotor noise. Spectra of multiple configurations can be compared to observe both individual and combined effects of those listed in the test matrix in Table 4.1. Since there are many parameters in a single configuration, it would be too lengthy to list every parameter each time a configuration is referenced, so a configuration numbering convention is provided in Table 4.2 to make this discussion more concise. Note that the nominal RPM is not specified in this table, since there are 5 rotational speeds per configuration, and splitting each speed into yet another configuration would yield less conciseness. The nominal RPM will simply have to be stated alongside the configuration number for a fully defined configuration.

Table 4.2: List of Configuration Numbers and Parameters.

Configuration Number	Blade Number	Blade Diameter	Pitch Angle	Turbulence Trips
Configuration 1	5	$0.457m$	9°	No
Configuration 2	5	$0.457m$	7°	No
Configuration 3	5	$0.457m$	9°	Yes
Configuration 4	5	$0.914m$	9°	No

4.2.1 Background Noise and Ground Board Calibrations

Background noise data was collected throughout the day, specifically during long periods of down-time when a significant change to the test configuration was being made and the propeller could not be run. These windows of background noise collection occurred approximately once per hour. This process was very simple and required no extra setup: all the electronics were turned off, everyone was cleared of the test area, it was ensured that all controllable noise was kept at a minimum, and acoustic data were taken like normal. However, background noise was retaken if the uncontrollable test conditions, such as wind gusts or nearby vehicles, were deemed to be abnormally high. This was acceptable because the same considerations were taken for propeller acoustics.

Since this experiment occurred outdoors, the environment was much less controlled than an indoor facility. This is important for the background noise because this means that the background noise may have variations from one moment to the next. This stochastic nature of the background noise makes it impossible to directly subtract background noise spectra from the rotor acoustic measurements since they were not acquired simultaneously. Instead, general observations and comparisons between the background noise levels with the rotor noise levels will be conducted. Figure 4.4 shows all of the background noise data collected during this experiment, totaling to 12 background noise spectra. Note that only the extreme microphone positions are shown, namely the upstream Microphone 1, in-plane Microphone 7, and downstream Microphone 13.

On a surface level, there appears to be a weak correlation between the background noise level with the time of day. Only two background noise spectra were collected on the first day, both in the evening, and they are some of the louder spectra. On the second day, more background noise was collected consistently throughout the day, and the spectra collected in the morning are generally quieter than those collected in the evening. This is likely due to increased highway activity. This is a large contributing factor to determining the quality of outdoor acoustic experiments, since these conditions are not always easily controllable. The large variations in these spectra further support the claim that the instantaneous background noise at this outdoor facility is random, and that direct spectral subtraction should not be done. However, plotting a spectra collected during rotor noise observation directly on top of the background noise spectra may reveal how significant the background noise impact

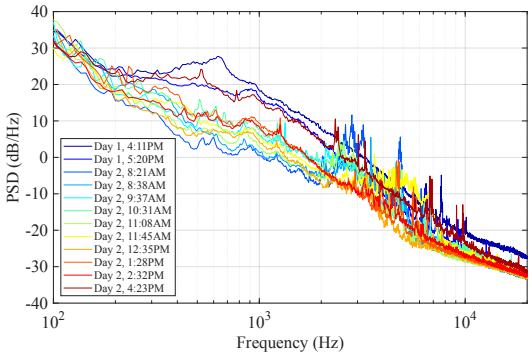

(a) Upstream Microphone 1.

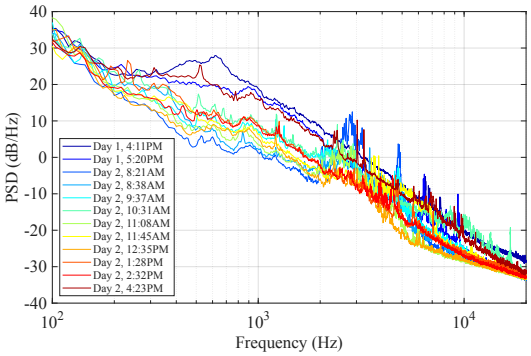

(b) In-Plane Microphone 7.

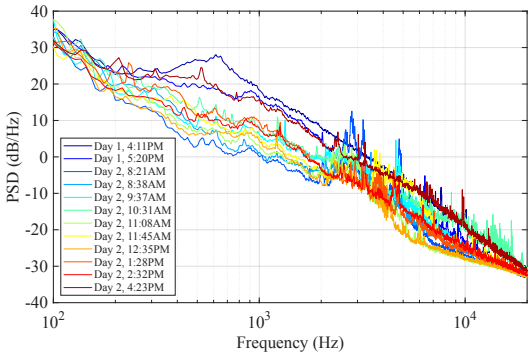

(c) Downstream Microphone 13.

Figure 4.4: Background Noise Distributions.

is. Figure 4.5 shows the average spectrum of the 12 background noise spectra with red and green lines indicating the maximum and minimum values, respectively. Additionally, this figure plots the spectra for Configuration 2 at $2400RPM$, which was one of the runs with the quietest rotor behaviors.

Using one of the quietest runs provides a very conservative estimate for which frequencies the rotor noise is substantially louder than the background noise. For the quietest observer position, or the in-plane Microphone 7, it appears that sound above about $1100Hz$ can be confidently attributed to actual rotor noise. For the along-axis Microphones 1 and 13, this cutoff appears at a slightly lower frequency, at about $1000Hz$. Of course, this is using a very cautious approach, and other operating conditions and configurations may have significant rotor-to-background noise ratios at lower frequencies. Additionally, the tonal peaks at the BPF are meaningfully louder than the background noise even below these cutoff frequencies. However, when considering the broadband noise component, it would be prudent to consider noise below $1000Hz$ with reasonable skepticism. However, these lower limits may be pushed further by separating the background noise according to the day the data were collected. Figure 4.6 shows the background noise average, maximum, and minimum separated by day.

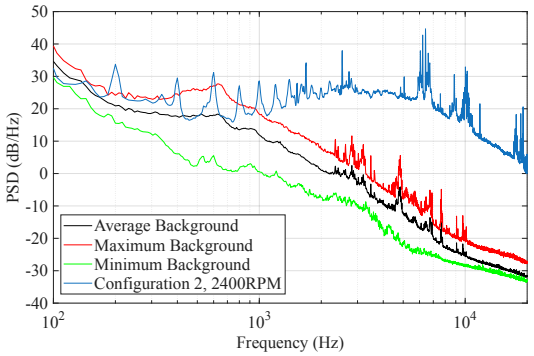

(a) Upstream Microphone 1.

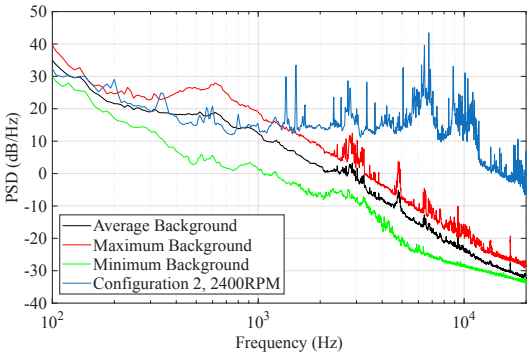

(b) In-Plane Microphone 7.

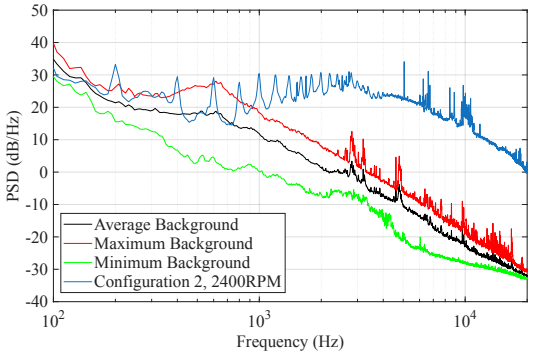

(c) Downstream Microphone 13.

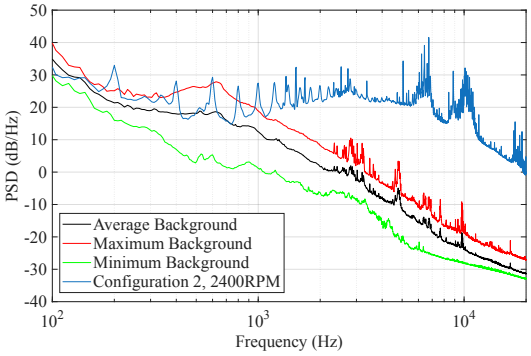

(d) Microphone Average.

Figure 4.5: Background Noise Averages, Minimums, and Maximums in Comparison to Configuration 2 at 2400RPM.

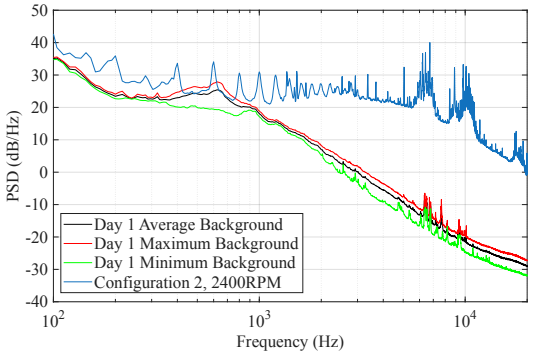

(a) Day 1 Background Noise Versus Configuration 2 at 2400RPM.

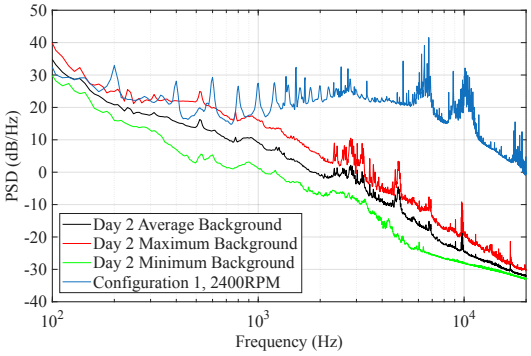

(b) Day 2 Background Noise Versus Configuration 1 at 2400RPM.

Figure 4.6: Background Noise Averages with Minimum and Maximum Ranges in Comparison to Quiet Rotor Spectra Collected on Corresponding Day.

Both of these plots show the average microphone spectra for conciseness. Additionally, Figure 4.6a shows the average microphone spectra for Configuration 2 at $2400RPM$, and Figure 4.6b shows the average microphone spectra for Configuration 1 at $2400RPM$, both chosen as representatives for the quietest rotor behavior on their respective day. Especially on the first day, there is a clear improvement with regard to the rotor noise levels above the background noise levels, even if the cutoff frequency is the same. To see this improvement, a signal-to-noise ratio (SNR) can be calculated as according to Equation 4.1. Furthermore, the PSD of the SNR of the average rotor noise over the background noise is shown in Figure 4.7.

$$PSD(SNR) = 10\log_{10}\left(\frac{G_{pp,Rotor}}{G_{pp,Background}}\right) \tag{4.1}$$

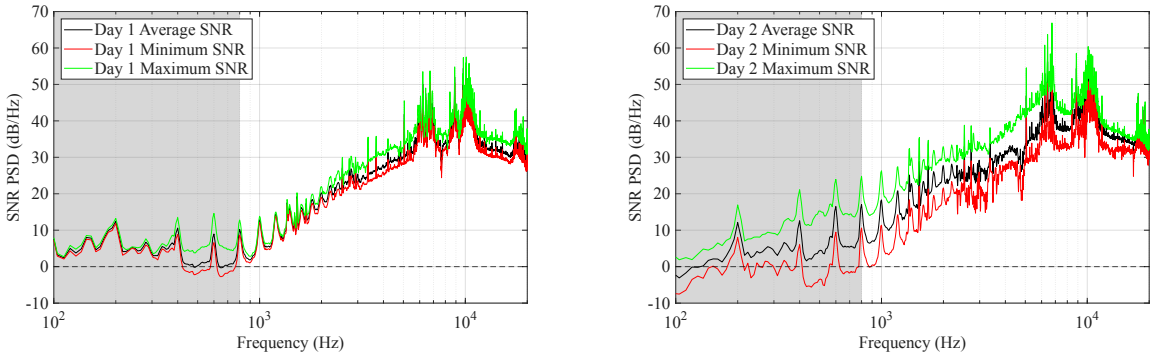

(a) Day 1 SNR.

(b) Day 2 SNR.

Figure 4.7: Rotor-to-Background SNR.

Note that a horizontal dashed black line is shown to easily reference zero. The SNR of the first day dips below zero around $400Hz$ to $800Hz$ for the worst cast scenario. For the second day, the worst case SNR is nonzero only above about $800Hz$. When cautiously observing spectra , it should be noted that noise lower than $800Hz$ is likely to be dominated by background noise. In these figures and all figures following, the background-noise-dominant region will be shaded as an indicator. This is done rather than completely excluding frequencies below $800Hz$ since a few significant tones at the blade passage frequency (BPF) occur below $800Hz$.

Since each microphone was placed on top of an acoustically rigid ground board, these also had to be calibrated. This calibration was not applied to the spectra presented above in Figures 4.4 or 4.5, but doing so would not change the conclusions since the calibration would apply equally to the background noise and Configuration 2 spectra, and only relative, not absolute, levels were used to draw the conclusions. The ground boards were assumed to be perfect acoustic reflectors, where an observer at the center of the ground board assumed to experience a pressure doubling effect relative to the same condition without a ground board.

Specifically, to correct for the ground board reflections, $6dB$ was simply subtracted from the background-corrected spectra. Refer to Section 3.3 for a more detailed justification of this assumption, but to recall in short, the frequency response of the ground board with a microphone at its center at an incidence angle of 23° is similar to that of a perfect infinite reflector at most frequencies between $200Hz$ and $10000Hz$, as seen in Figure 3.7. Equation 4.2 shows the simple ground board correction calculation to obtain the fully corrected spectra.

$$10\log_{10}\left(\frac{G_{pp,Corrected}}{p^2_{Ref}}\right) = 10\log_{10}\left(\frac{G_{pp,Raw}}{p^2_{Ref}}\right) - 6dB \tag{4.2}$$

From this point forth, unless otherwise stated, all spectra presented from the Drone Park experiment are fully corrected with respect to ground board reflections.

4.2.2 Wind, OASPL, and Spectrogram Sequestering

As briefly mentioned at the beginning of Section 4.1, wind velocity and gusts were measured during the experiment with an ultrasonic anemometer. Although these data were taken at roughly the same time as the acoustic data, the main difficulty was that the anemometer DAQ was not synchronized with the microphone DAQs and have different sampling frequencies, so exact correlations between wind gusts and acoustic fluctuations would generally be weaker and less representative of their relationship. However, general trends were still observable, and the acoustic data was still successfully filtered through the wind data.

The raw wind data consisted of time-varying U-, V-, and W-components of wind velocity (u_{wind}, v_{wind}, and w_{wind}, respectively). Again, data collection for the wind velocities were not synchronized with the acoustic data, and the start and end of the wind data collection had to be manually commanded. This resulted in the wind velocity data files encapsulating a larger time window than the acoustic time-series data, whose stop condition was automated to end after $32s$. This was done to ensure that the wind data were collected throughout the entire acoustic time window.

These instantaneous wind velocity data can be plotted against their own time, an example of which can be seen in Figure 4.8. This shows the wind velocities for Configuration 1 at $4000RPM$. The U-, V-, and W-components of the wind are shown in red, blue, and green, respectively. The wind velocity magnitude was also calculated from these components and is shown as the solid black line in Figure 4.8. Note that the horizontal black dashed line marks the no-wind condition for ease of visibility.

As expected, the W-component of the wind velocity hovers around $0m/s$, whereas most of the fluctuations occur in the plane parallel to the ground. Recall from Figure 4.3 that a negative U-component means that the wind is flowing from behind the propeller. This effectively increases the angle of attack of each blade and may increase blade-wake ingestion

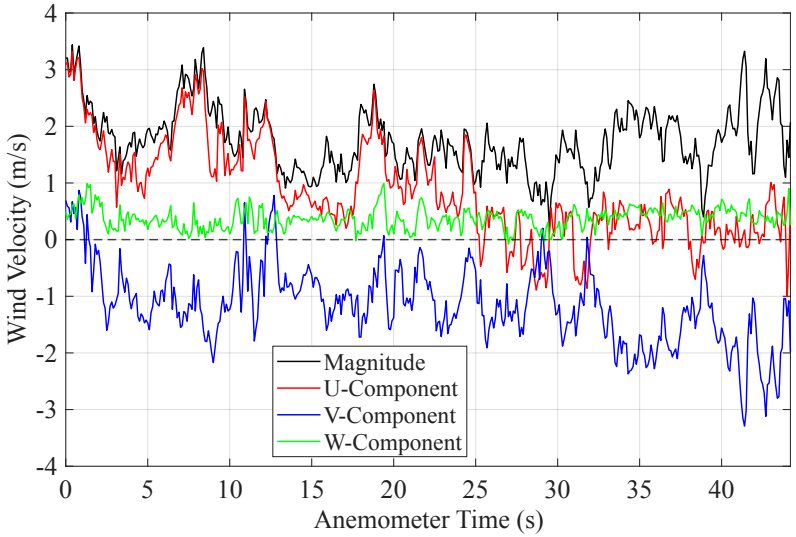

Figure 4.8: Wind Velocity Data of Configuration 1 at $4000RPM$.

(BWI) noise and even cause boundary layer separation. Boundary layer separation can be estimated by calculating the effective angle of attack of each blade using pitch, linearized rotational speed at a given position along the blade radius, and inflow velocity, as shown in Equation 4.3.

$$\alpha_{eff} = \beta - \arctan\left(\frac{u_{wind}}{v_{local}}\right) \tag{4.3}$$

Here, β represents the local twist angle (which can be obtained from Figure 2.4), u_{wind} is the inflow velocity, and v_{local} is the local linear blade speed. At a location 70% of the radius along the blade and at the fastest rotational speed and assuming a backwards flow of $2m/s$, the effective angle of attack is approximately $\alpha_{0.7R} \approx 19.5° - \arctan\left(\frac{-2m/s}{67m/s}\right) \approx 22.9°$, but decreases to about 21.2° at the fastest rotational speed. Further analysis with the specific airfoil geometry would be required to determine boundary layer behavior, but if separation occurred, this would increase the blade self-noise contributions to broadband noise. Therefore, when looking for clean segments of the full time-series for broadband noise analysis, these wind data imply that the best segments would be those with non-negative u_{wind}.

To verify or falsify this hypothesis, these wind velocity fluctuations can be compared to the acoustic fluctuations over time, which will first be represented with time-varying overall sound pressure level (OASPL). For the following calculation, the pressures were integrated between $1000Hz$ and $5000Hz$. This range was chosen to exclude the lower background noise frequencies (which are significant up to about $800Hz$) and the higher motor noise frequencies

(which are significant around $6000Hz$ to $9000Hz$) and isolate the aerodynamic propeller noise. This was considered to be the time-varying acoustic fluctuations over the entire measurement period and compared to the wind velocity fluctuations. For these analyses, 511 records were used for spectral analysis of the full time-series, so the time-varying OASPL had a resolution of 511 points over 32 seconds. Figure 4.9 shows the time-varying OASPL for Configuration 1, with the upstream Microphone 1 shown in blue, the in-plane Microphone 7 shown in orange, and the downstream Microphone 13 shown in yellow.

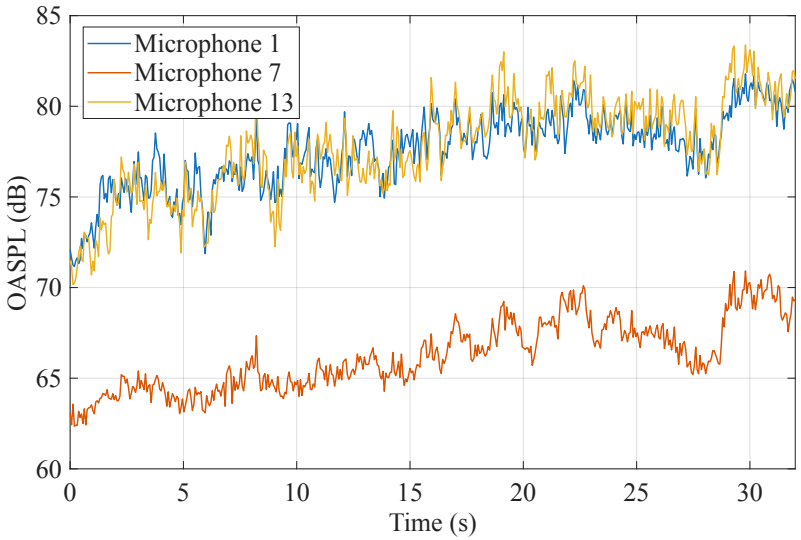

Figure 4.9: OASPL Over Time of Configuration 1 at $4000RPM$.

The same trend is observed for all microphone positions, which appears to be related to u_{wind}. The steady increase in OASPL during the first 25 seconds lines up well with the steady decrease in wind velocity, after which both the OASPL and wind velocities hold relatively constant. An obvious observation that can be made is that the OASPL as heard by Microphone 7 is much lower than that of the other shown microphones. This is likely due to the behavior of the propeller noise sources observed. The decrease in flow velocity into the propeller would affect the loading noise and prevent the wake from convecting downstream of the propeller, increasing the blade-wake interaction (BWI) noise. Furthermore, when the flow velocity becomes negative, the wind would push the wake back into the propeller and cause wake reingestion, increasing the turbulence ingestion noise (TIN). Steady loading, BWI noise, and TIN all primarily propagate along the axis of rotation, which explains why Microphones 1 and 13, which are the closest to the rotational axis, experience much louder sound levels compared to the in-plane Microphone 7. This directivity is more clearly shown in Figure 4.10, which shows the time-varying OASPL directivity. Again, the OASPL is calculated from $1000Hz$ to $5000Hz$. This is a polar plot to reflect the experimental setup, and the microphone positions are labeled as such. Note that the radial axis is time, and the color gradient represents the OASPL.

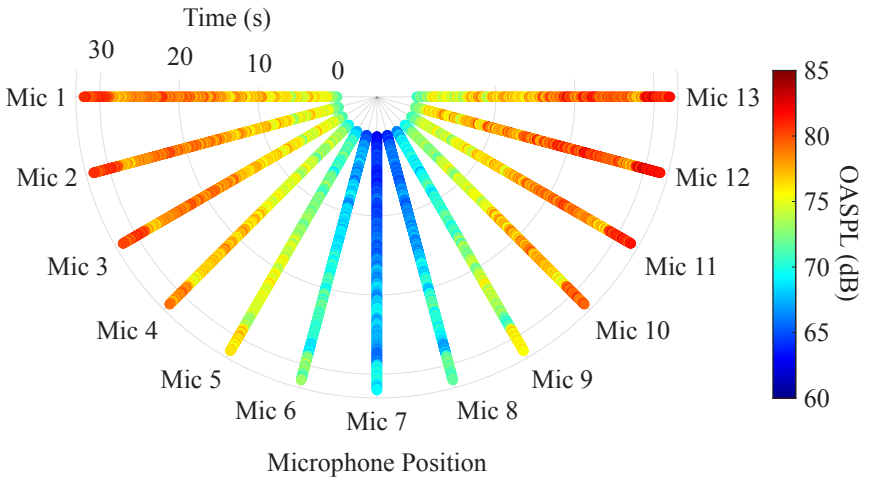

Figure 4.10: Directivity of OASPL Over Time of Configuration 1 at $4000RPM$.

See that all the microphones hear a steady increase in OASPL, consistent with the slowly decreasing u_{wind}. Furthermore, Figure 4.10 reflects a dipole-like directivity, with maximum sound levels along the axis of rotation and minimum levels in-plane, exactly the expected behavior consistent with loading noise of a rotor. This also shows the general acoustic trends of each microphone that are consistent with the previously proposed relationship with the wind velocity. Of course, there are inherent limitations in observing only OASPL, emerging from collapsing an entire frequency spectra to a single value. This blending of low- and high-frequency behaviors make them indistinguishable. This is especially clear since the lower background noise frequencies and the higher motor noise frequencies had to be excluded in order to observe the rotor noise. However, perhaps a more compelling argument for all microphones can be made by observing their spectrograms, which can display full frequency spectra over time. The spectrograms for the same microphones are shown in Figure 4.11.

These spectrograms also show correlation between the noise and the wind in the U-direction. In the spectrograms for Microphones 1 and 13, the PSD clearly appears to gradually increase throughout the entire time-series, especially in the $2000Hz$ to $5000Hz$ range. This behavior corresponds to the gradual wind decrease in the U-direction. More importantly, these trends are much more visible in the spectrograms than the time-varying OASPL plots. The trend for Microphone 7 is less obvious, but it is still visible. There are some loud events early on in the lower frequencies around $100Hz$ to $200Hz$, which are likely caused by random variations in the instantaneous background noise. Around the 16 to 17 second mark, Microphone 7 starts to more clearly hear some PSD increase that the other microphones also hear, but to a much lesser degree. This phenomenon is again likely due to directivity effects, which further suggests that the reduced wind velocity in the U-direction increases the unsteady loading noise, and such noise propagates dominantly along the axis

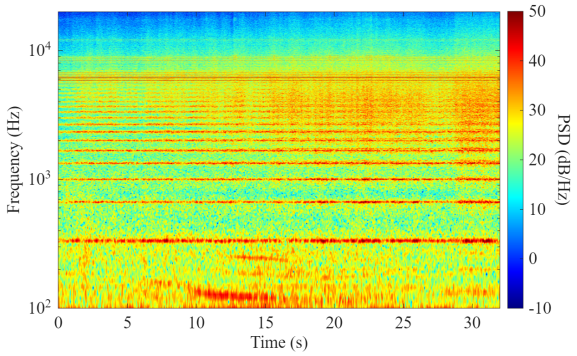

(a) Upstream Microphone 1.

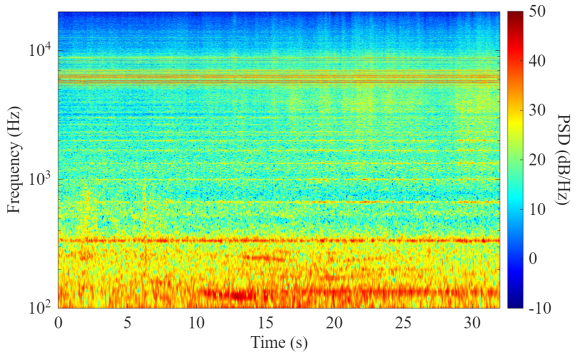

(b) In-Plane Microphone 7.

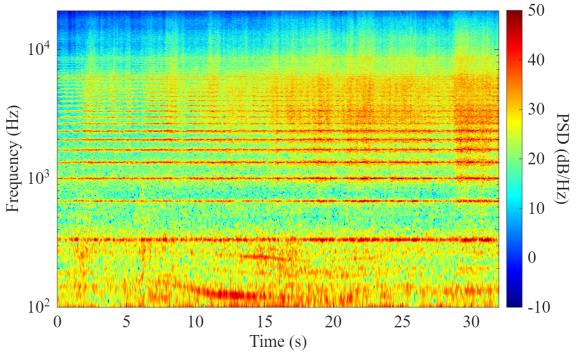

(c) Downstream Microphone 13.

Figure 4.11: Spectrograms of Configuration 1 at $4000RPM$.

of rotation in the mid- to high-frequency ranges.

To observe the effects of manually sequestering the data based on wind velocity, Figure 4.12 shows the spectra calculated from the full time-series compared to the spectra calculated from the sequestered signal. The selected sequestered time segment for this configuration was from $0s$ to $12s$, selected due to u_{wind} being consistently between $0.5m/s$ and $3m/s$, as well as relatively low high-frequency noise. Additionally, the spectra of the other sequestered segment of the time-series (the spectra calculated from $12s$ to $32s$, where u_{wind} was approximately between $-1m/s$ and $0.5m/s$) are also shown to further emphasize the effect of sequestering the time-series. The $0.5m/s$ boundary between the two conditions was chosen somewhat as an arbitrary factor of safety between small positive inflow and near-zero inflow conditions.

At first glance, there does not appear to be a large difference between these spectra, especially in the tonal peaks. Indeed, the most significant change occurs with the broadband trend. The sequestered spectra with $0.5m/s < u_{wind} < 3m/s$ see a decrease in the amplitude of the broadband noise, especially in the frequency range above $1000Hz$. The largest difference occurs in the $2000Hz$ to $6000Hz$ range, where the sequestered spectra is about

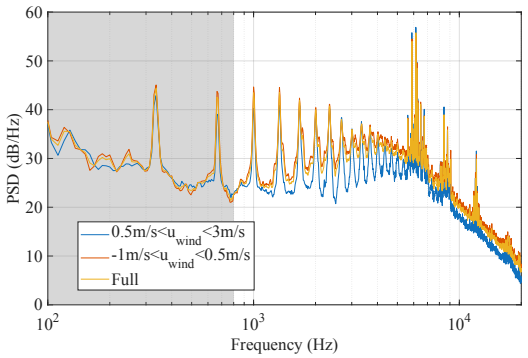

(a) Upstream Microphone 1.

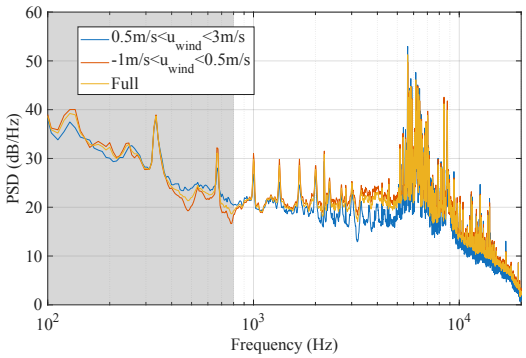

(b) In-Plane Microphone 7.

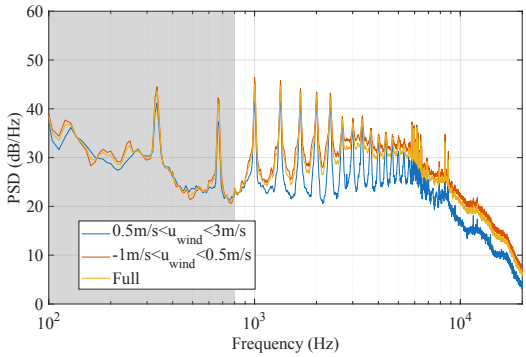

(c) Downstream Microphone 13.

Figure 4.12: Comparison of Spectra Calculated from Sequestered Versus Full Time-Series of Configuration 1 at $4000RPM$.

$5dB$ to $10dB$ quieter than the full spectra. Additionally, the sequestered spectra considering $-1m/s < u_{wind} < 0.5m/s$ are relatively similar to the full spectra, especially in comparison to the $0.5m/s < u_{wind} < 3m/s$ sequestered spectra. This further supports the idea that sequestering based on the wind and spectrograms affects the broadband noise levels. This is significant for a number of reasons. First, in relation to physical phenomena, this result makes sense, since the sequestering process appears to separate different sources of noise that may be changing over time, which would register as broadband noise. Second, a more accurate representation of the broadband noise is necessary for comparison of these experimental results with mathematical predictions, such as the GLSM [8], which may not take flow conditions into consideration, so corresponding experimental conditions should be used for relevant comparisons. Third, this sequestration allows for the gathering of relatively steady and constant inflow conditions, which is necessary to obtain datasets comparable to datasets obtained in more controlled environments, such as in a wind tunnel. This will be obvious in the next experiment described in Chapter 5.

A preliminary conclusion can be drawn that to optimize analyses, the time-series data should be sequestered based on flow conditions, especially between positive and negative

inflows. Analysis of a single run can be refined by separately analyzing the segments of the full time-series where $0.5m/s < u_{wind} < 3m/s$ and those where $-1m/s < u_{wind} < 0.5m/s$. Comparability between two conditions can be further extended by sequestering the full time-series into smaller time segments that have similar environmental wind conditions, especially in the U-direction.

This preliminary conclusion should also be corroborated by performing the same analysis with another configuration. Figure 4.13 shows the wind velocity plot, time-varying OASPL, OASPL directivity, Microphone 1 spectrogram, and Microphone 1 spectra for the full and sequestered time-series of Configuration 3 at $2800RPM$. Similar to Figure 4.8, SubFigure 4.13a shows a steady wind decrease in the U-component, which also correlates with the steady OASPL increase in SubFigure 4.13b. The sudden spike in OASPL around $8s$ seems to correspond with the sudden dip in u_{wind} around $7s$. Also, SubFigure 4.13c shows that the rotor exhibits directivity similar to that of a dipole, and that the greatest acoustic changes occur along the axis of rotation. SubFigure 4.13d shows that the majority of the increase in sound occurs in the $2000Hz$ to $6000Hz$ frequency range, and that the steepest increase occurs around $15s$, corresponding to when u_{wind} dips below $0.5m/s$. The time-series was sequestered from $0s$ to $15s$ for this configuration, and the sequestered spectrum for Microphone 1 in SubFigure 4.13e shows a $1dB$ to $2dB$ quieter broadband trend than its full spectrum. The effect of sequestering is less prominent than seen in Figure 4.12, likely due to the lower rotational speed. All of these results reinforce the previous conclusions made from examining Configuration 1.

Another, less significant result was implied, which is the reinforcement of the effect of loading on rotor noise. Greater flow into the propeller would decrease thrust and therefore decrease noise. This is reflected in the cross-examination between the U-velocity and spectrograms for both configurations. The sequestered time-series based on $0.5m/s < u_{wind} < 3m/s$ isolates these periods of positive U-velocity and therefore periods of lower thrust and broadband noise.

These results reinforce the conclusion that sequestering the time-series data should be done, perhaps considering the separation of different operating conditions, such as small positive inflows ($0.5m/s < u_{wind} < 3m/s$) and near-zero and negative flows ($-1m/s < u_{wind} < 0.5m/s$). These conditions have the possibility of separating a different noise sources, including unsteady loading noise or even TIN and BWI noise, which may be varying with time. This will especially be useful in Section 5, where a similar experiment was conducted indoors and isolated from the potentially turbulent outdoor environment and cleaner acoustic signals were measured.

4.2.3 Broadband and Tonal Components

The total noise spectra were broken down into broadband and tonal components using methods described in SubSection 1.2.4. The breakdown of noise for Microphones 1, 7, and

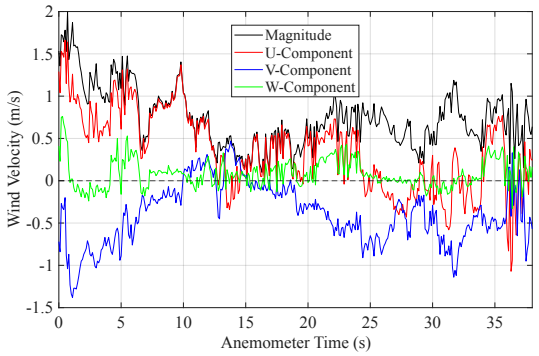

(a) Wind Velocity Over Time.

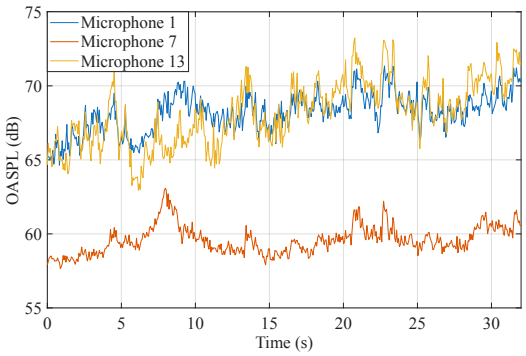

(b) OASPL Over Time.

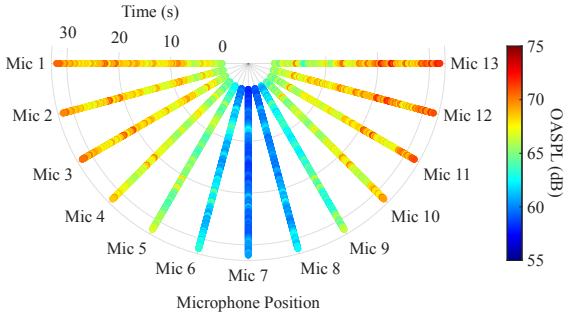

(c) OASPL Directivity.

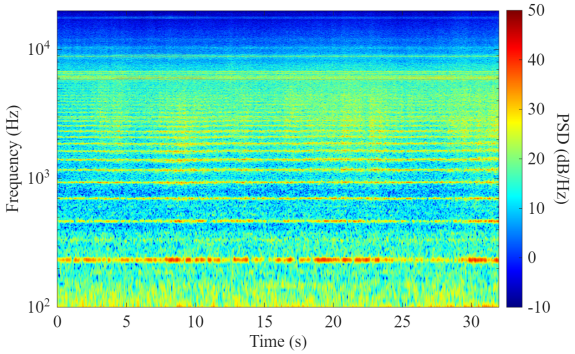

(d) Microphone 1 Spectrogram.

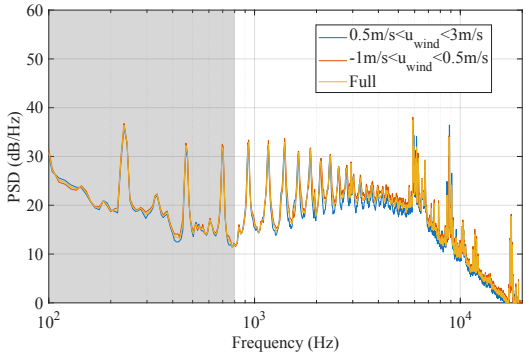

(e) Microphone 1 Spectra Comparison.

Figure 4.13: Summary of Configuration 3 at $2800RPM$

13 of the sequestered time-series of Configuration 1 at $4000RPM$ is shown in Figure 4.14.

Observe that the tonal noise contribution is the highest near $6000Hz$. This is thought to be primarily due to mechanical and electrical motor noise and not due to aerodynamic rotor noise. Unfortunately, pure motor noise without any propeller attached was not recorded and therefore this proposition is unable to be verified. Note that other than the motor noise frequencies, there are about three tonal spikes before the tonal spike at the blade passage

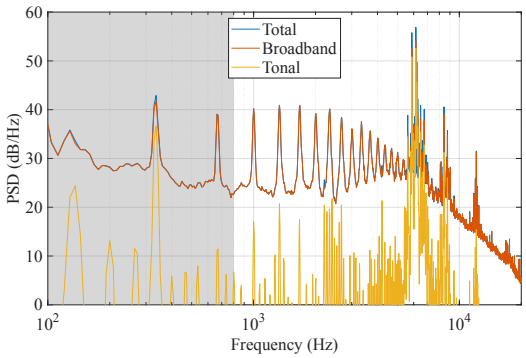

(a) Upstream Microphone 1.

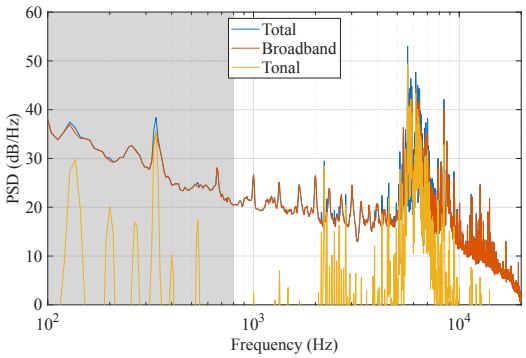

(b) In-Plane Microphone 7.

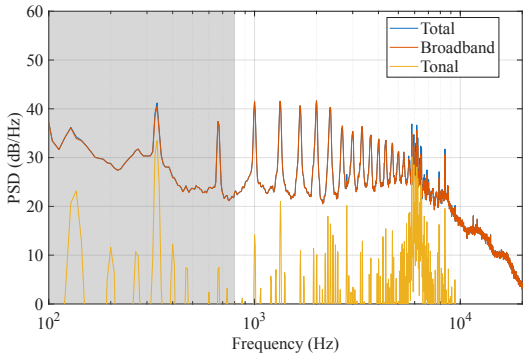

(c) Downstream Microphone 13.

Figure 4.14: Decomposition of Sequestered ($0.5m/s < u_{wind} < 3m/s$) Total AutoSpectra into Broadband and Tonal Components of Configuration 1 at $4000RPM$.

frequency (BPF). These first three tonal spikes are likely harmonics of the shaft rate. At the BPF, the broadband component decreases enough that the blue line representing the total noise is just visible, implying that there is a relatively significant tonal noise contribution at this frequency. For ease of reference, Table 4.3 shows a list of the nominal RPM and their associated BPF for a 5-bladed propeller. Note that the first row of this table is more of a guideline, since the $0.914m$ propeller was spun at the lower speeds, and the $0.457m$ was spun at the higher speeds such that the tip Mach Number at both scales remains constant. For Configuration 1 at $4000RPM$, the BPF is $333Hz$, which is exactly where the largest tonal spike occurs (disregarding the motor noise frequencies around $6000Hz$).

Table 4.3: List of Nominal RPM and Blade Passage Frequencies.

Rotor Diameter	$0.914m$					$0.457m$				
Nominal RPM	1200	1400	1600	1800	2000	2400	2800	3200	3600	4000
5-Blade BPF (Hz)	100	117	133	150	167	200	233	267	300	333

Aside from the tonal spike at the BPF and the motor noise, this decomposition reveals

that the overwhelming majority of the total noise is generated by broadband interactions and are broadband features. The result is nearly identical for all microphones, and a similar ratio between tonal noise and broadband noise can be observed at other rotational speeds. Even at the BPF and harmonics, the broadband component is greater than the tonal component. This suggests that the majority of what may be perceived as tonal noise may be caused by BWI or turbulence ingestion. Since these phenomena are not truly periodic, this would register as broadband noise; however, on short time-scales, the interaction between coherent inflow turbulence or wake and the rotor occurs at the BPF. This produces broadband peaks at these frequencies. Since BWI and TIN propagate along the axis of rotation, this would also explain why the in-plane Microphone 7 experiences a similar trend but the acoustic response is much quieter. To view the effect of rotational speed, Figure 4.15 shows the same decomposition into broadband and tonal noise for Microphone 1 of Configuration 1 at $2400RPM$, $2800RPM$, $3200RPM$, and $3600RPM$. Only Microphone 1 is shown for conciseness.

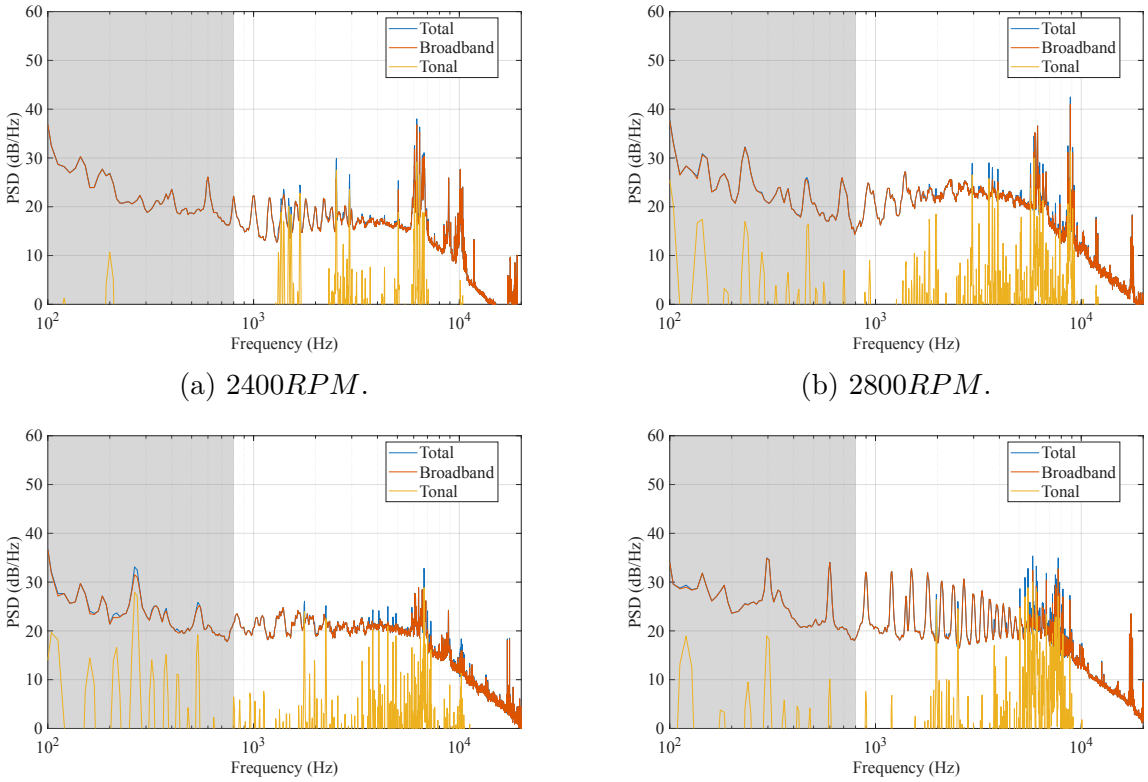

(a) $2400RPM$.

(b) $2800RPM$.

(c) $3200RPM$.

(d) $3600RPM$.

Figure 4.15: Decomposition of Sequestered ($0.5m/s < u_{wind} < 3m/s$) Total AutoSpectra into Broadband and Tonal Components for Microphone 1 of Configuration 1 at $2400RPM$, $2800RPM$, $3200RPM$, and $3600RPM$.

Consistent at all rotational speeds and configurations is the largely dominant broadband

component, which almost completely physically obscures the total noise curve in Figures 4.14 and 4.15, even often dominating over tonal noise at the BPFs. These results are in accordance with expectations regarding outdoor testing environments, which subjects the propeller to higher chances of encountering turbulence. These turbulent structures interact with the propeller, increasing its noise especially at the BPF and its harmonics, which appears to be tonal noise in the short-term timescale. However, since these turbulent structures are truly stochastic, the noise generated by these turbulent interactions are truly broadband noise sources, despite the increase in noise at the BPF and frequencies commonly correlated with tonal noise sources. A similar explanation could potentially be made for BWI, assuming there are components that occur with interaction timescales associated with the BPF.

Further comparisons between this experimental data with predictive models proves to be quite difficult, the main reason being the components that contribute towards broadband noise. Recall that three major broadband noise sources include TIN, BWI, and trailing edge noise. Accurately modeling the first two of these require detailed knowledge about the inflow and wake conditions, which is nearly impossible to obtain in field experiments. However, there are many predictive tools to model trailing edge noise, such as the Gill-Lee Spectrum Model [8]. This model will be used for comparisons against the sequestered spectra, although it should be noted that these may not be fully comparable, since modeling is limited to trailing edge noise and the experimental data may encapsulate other broadband noise sources, even after sequestration. Furthermore, recall that this model was trained using datasets primarily considering operating conditions of Mach Numbers between 0.2 and 0.4 and normalized thrust coefficients between 0.14 and 0.18. The data presented in this work generally have tip Mach Numbers between 0.166 and 0.28 and a normalized thrust coefficient of up to $\frac{C_T}{\sigma} \approx \frac{0.03}{0.195} \approx 0.154$. These operating conditions clearly fall on the lower end of what the GLSM was trained for, which may cause some inaccuracies simply due to the fact that the experimental data are beginning to fall outside the scope of the model. Figure 4.16 shows the broadband component derived from the experimental data from Configuration 1 at $4000RPM$ compared against the prediction generated by the GLSM [8] at the Microphone 1, 7, and 13 positions. Note that the frequency range is limited to $800Hz$ to $20000Hz$ to focus on the broadband frequency range.

Observe that the GLSM is compared against both sequestered spectra and the full spectra. On average, the GLSM appears to predict the sequestered spectra based on $-1m/s < u_{wind} < 0.5m/s$ and full spectra the best and well over-predicts the sequestered spectra based on $0.5m/s < u_{wind} < 3m/s$. This is primarily due to the nature of the GLSM, which is a trailing edge noise model derived from datasets considering a hover flight condition. This explains why the GLSM more closely matches the sequestered spectra with near-zero inflow velocities, since this portion of the time-series corresponds to inflow velocities near $0m/s$, similar to the hover conditions used to derive the GLSM. The differences in these spectra could also be explained by differences in thrust coefficient. Recall from Equation 1.3 that one of the GLSM parameters is the thrust coefficient C_T. The GLSM prediction plotted in purple in Figure 4.16 was calculated using the average C_T over a non-simultaneous sampling period, but the

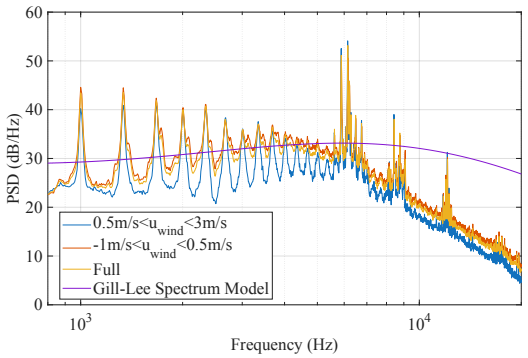

(a) Upstream Microphone 1.

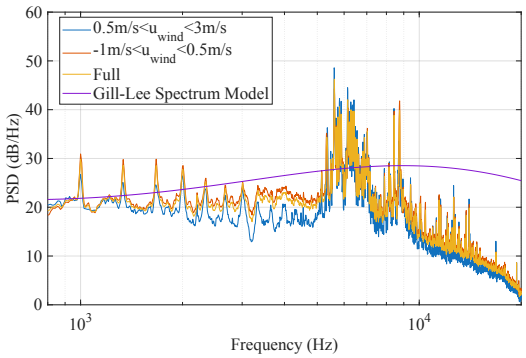

(b) In-Plane Microphone 7.

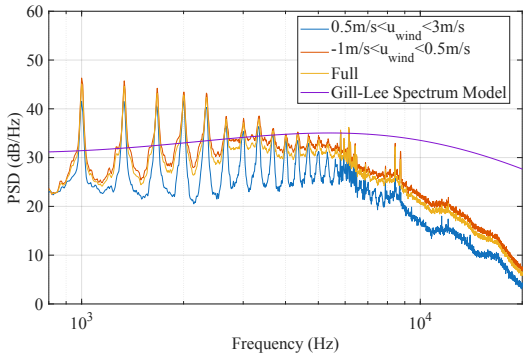

(c) Downstream Microphone 13.

Figure 4.16: Comparison of Broadband Experimental Data Versus Gill-Lee Spectrum Model of Configuration 1 at $4000RPM$.

sequestered time-series may have a different average C_T and result in a different prediction that may match the sequestered spectra better. Importantly however, within the $1000Hz$ to $6000Hz$ range, the shape of the GLSM spectra matches the broadband component fairly well, even if the levels do not align. One difference between the experimental data and the GLSM prediction is where the broadband noise peaks. On average, the GLSM prediction peaks around $6500Hz$, whereas the broadband trend in the experimental data peaks around $4500Hz$. Consequently, another large deviation is that the experimental spectra drop off much quicker than the GLSM prediction. Further analysis with applying the ISO-9613-1-1993 attenuation standard [12] revealed that at the environmental conditions during the experiment, attenuation only accounted for at most a $1dB$ offset, and the experimental data still would not match the slope of the GLSM prediction above $10000Hz$. However, it is important to note that this standard is only applicable up to $10000Hz$, and a more robust attenuation standard should be applied. Figure 4.17 shows this attenuation correction compared to the GLSM prediction. Note that only Microphone 1 is shown for brevity.

Additionally, recall from Chapter 3 that the ground board does not behave exactly like a perfect reflector, which can be seen Figure 3.7. In Figure 3.7, it can bee seen that there is

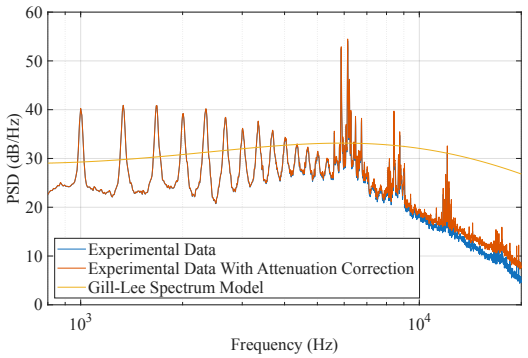

(a) $0.5m/s < u_{wind} < 3m/s$.

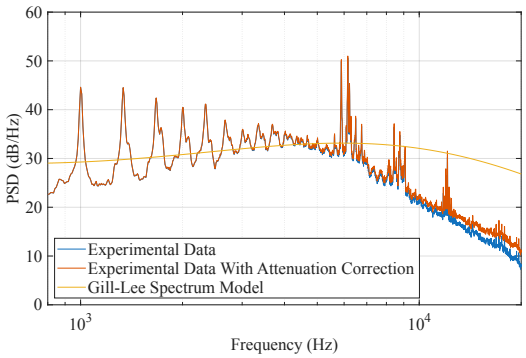

(b) $-1m/s < u_{wind} < 0.5m/s$.

Figure 4.17: Estimation of Attenuation Effects Using ISO-9613-1-1993 Standard [12] for Microphone 1 of Configuration 1 at $4000RPM$. Relevant Parameters: $p_a = 102000Pa$, $T_a = 295K$, $\phi = 40\%$.

a decline in PSD above $10000Hz$, from about $1dB$ to $6dB$ below the behavior of a perfect reflector. This may account for the steep slope in the experimental data above $10000Hz$, but not to the entire $20dB$ difference seen in Figure 4.17 and not as low as $7000Hz$. Additionally, it is important to note that the frequency response in Figure 3.7 was obtained for an anechoic environment, so a response should be obtained in the same environment as the experimental data to confirm this.

These conclusions, specifically about the effects of sequestering on broadband noise, are corroborated by the same analysis for Configuration 3 at $2800RPM$ shown in Figure 4.18.

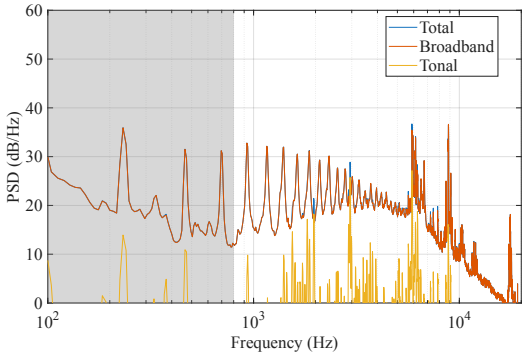

(a) Total, Broadband, and Tonal Components.

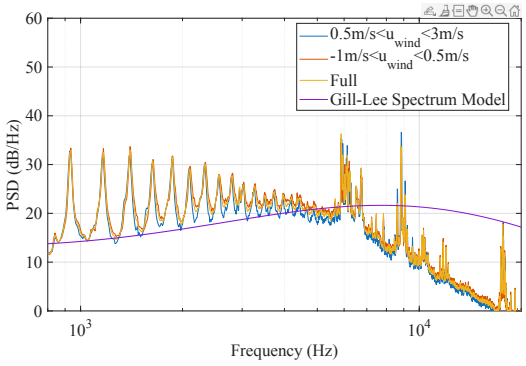

(b) Broadband Experimental Data Versus Gill-Lee Spectrum Model.

Figure 4.18: Broadband and Tonal Decomposition and Gill-Lee Spectrum Model Comparison of Microphone 1 of Configuration 3 at $2800RPM$.

Figure 4.18a also reveals that the majority of the noise is broadband, and Figure 4.18b shows that the GLSM produces a prediction that matches the shape of the experimental data

within the $1000Hz$ to $6000Hz$ range and drops off slower above $7000Hz$. The GLSM prediction also peaks around $6500Hz$, and the experimental data peaks earlier at about $3000Hz$. These results generally reinforce the conclusions made from analyzing Configuration 1 at $4000RPM$.

4.2.4 Effects of Scale

One major limitation to indoor acoustic testing is scale, and the difficulty with testing full or large scale rotors in a confined wind tunnel. Therefore, it is important to understand the effects of scale in the outdoor environment to begin relating results to indoor acoustic experiments.

Analysis was performed on Configuration 4, which is essentially the same as Configuration 1 but with a diameter of $0.914m$ instead. To account for the doubled scale, the rotational speeds were halved to match tip speeds, which are shown in Table 4.4.

$\vec{\mathbf{V}}_{\mathbf{Tip}}$ **(m/s)**	57.5	67	76.6	86.1	95.8
Required RPM for 0.457m Diameter	2400	2800	3200	3600	4000
Required RPM for 0.914m Diameter	1200	1400	1600	1800	2000

Table 4.4: Required Rotational Speed for Given Propeller Diameter and Tip Speed

The broadband component of Configuration 4 at $2000RPM$, Configuration 1 at $4000RPM$ and the corresponding GLSM prediction is shown in Figure 4.19. Furthermore, the sequestered spectra based on $0.5m/s < u_{wind} < 3m/s$ are shown in the left column, and the sequestered spectra based on $-1m/s < u_{wind} < 0.5m/s$ are shown in the right column.

For the sequestered spectra considering a small positive inflow, the GLSM unsurprisingly overpredicts the experimental broadband levels at both scales. Up to about $10000Hz$, the GLSM appears to overpredict the $0.914m$ scale more than it overpredicts the $0.457m$ scale. Additionally, the peak in the GLSM occurs at a lower frequency at the $0.914m$ scale than the $0.457m$ scale (shifting from about $7000Hz$ to about $3000Hz$), and a similar trend is visible in the experimental data (shifting from about $4500Hz$ to about $2000Hz$). However, when comparing the GLSM to the sequestered spectra considering a near-zero inflow, the model and experimental data match much better, with the GLSM matching the broad spectral features within about $3dB$ to $5dB$ rather than about $10dB$ to $15dB$. This is consistent with the comparisons done in the previous subsection, where the inflow conditions near $0m/s$ of the sequestered spectra are similar to the hover conditions used to derive the GLSM. One may also note that the broad spectral features of the experimental data do not appear to vary with size as much as the GLSM predicts, which may simply be due to only a smaller portion of the training data for the GLSM encapsulating these experimental conditions.

It is also important to compare the tonal noise from the two experimental spectra in more

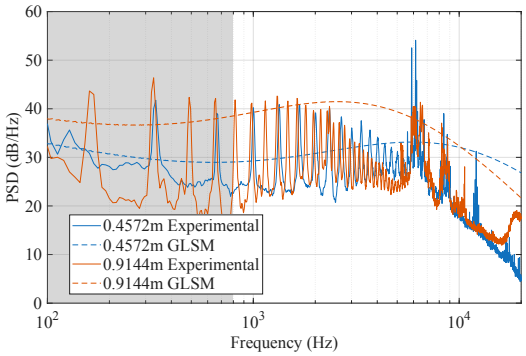

(a) Microphone 1 ($0.5m/s < u_{wind} < 3m/s$).

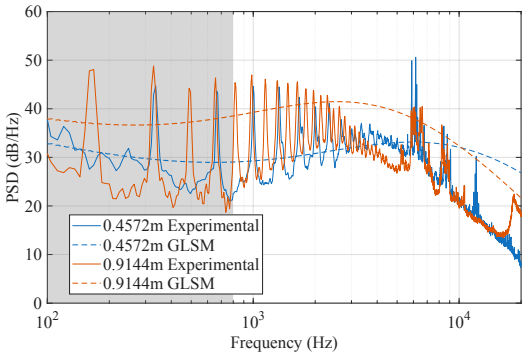

(b) Microphone 1 ($-1m/s < u_{wind} < 0.5m/s$).

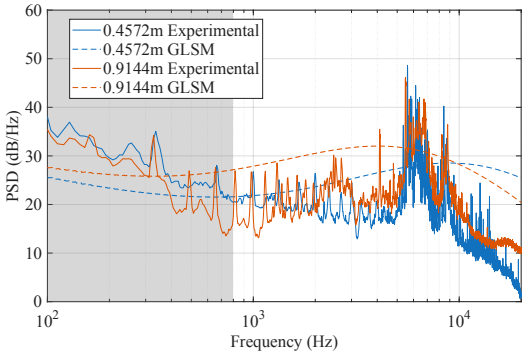

(c) Microphone 7 ($0.5m/s < u_{wind} < 3m/s$).

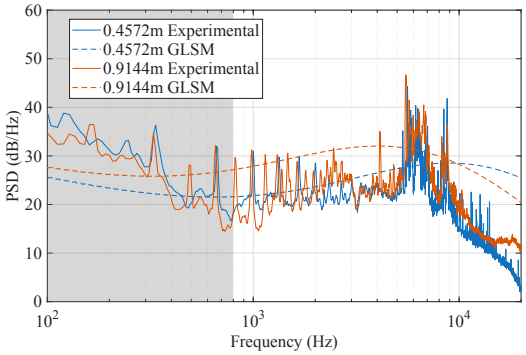

(d) Microphone 7 ($-1m/s < u_{wind} < 0.5m/s$).

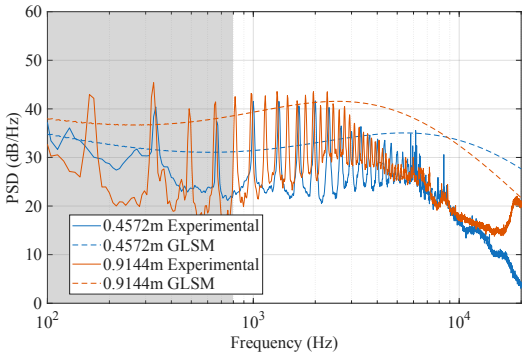

(e) Microphone 13 ($0.5m/s < u_{wind} < 3m/s$).

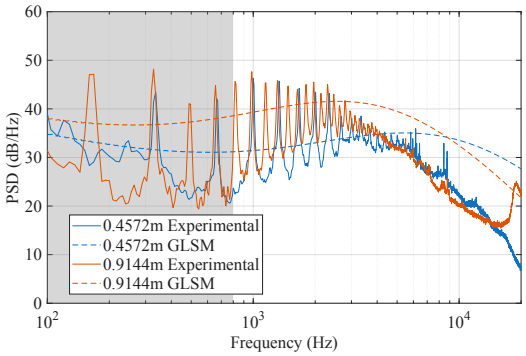

(f) Microphone 13 ($-1m/s < u_{wind} < 0.5m/s$).

Figure 4.19: Comparison of Broadband Experimental Data Versus Gill-Lee Spectrum Model of Configuration 1 at $4000RPM$ and Configuration 4 at $2000RPM$.

detail. The tones for the $0.914m$ scale occur twice as frequently as the tones for the $0.457m$ scale, which is expected since the former is rotating half as fast as the latter, resulting in a halved BPF and twice the harmonics. Of course, the tones of the two scales do not line up exactly since the propeller speed was not kept perfectly at the nominal RPM, but was manually maintained within about $\pm 2\%$ of the nominal value. To more consistently compare

the two scales, Figure 4.20 shows the frequency spectra of the experimental data normalized on their BPFs. Note that where other figures have a gray shading to indicate frequencies at which background noise may be significant, Figure 4.20 has correspondingly split the shading into blue and orange regions due to the re-scaled frequency axis.

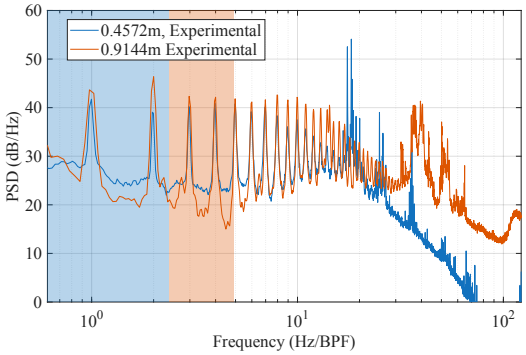

(a) Microphone 1 ($0.5m/s < u_{wind} < 3m/s$).

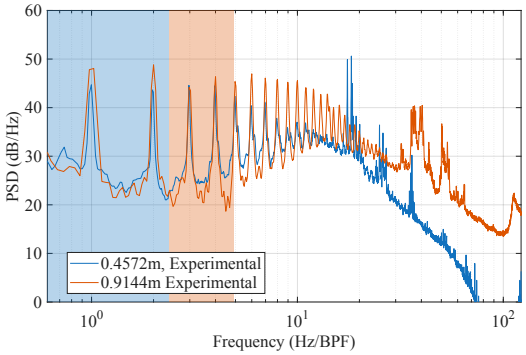

(b) Microphone 1 ($-1m/s < u_{wind} < 0.5m/s$).

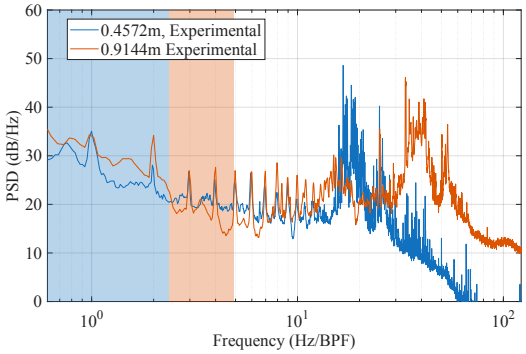

(c) Microphone 7 ($0.5m/s < u_{wind} < 3m/s$).

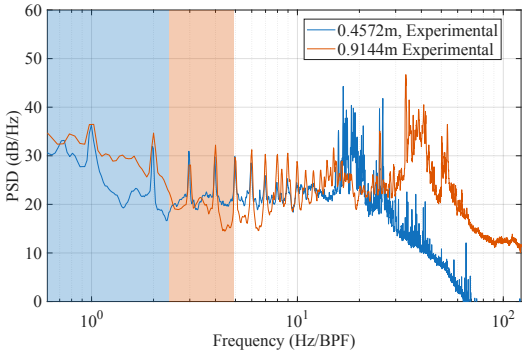

(d) Microphone 7 ($-1m/s < u_{wind} < 0.5m/s$).

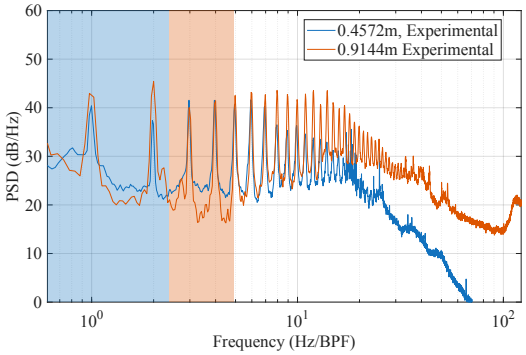

(e) Microphone 13 ($0.5m/s < u_{wind} < 3m/s$).

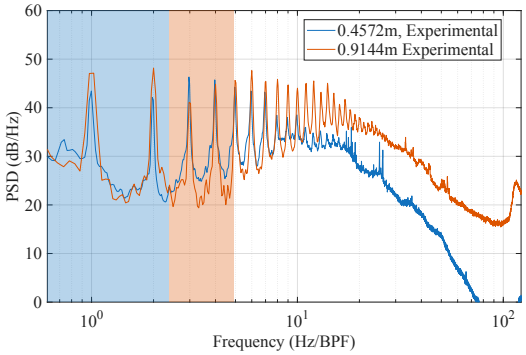

(f) Microphone 13 ($-1m/s < u_{wind} < 0.5m/s$).

Figure 4.20: Comparison of Sequestered ($0.5m/s < u_{wind} < 3m/s$) Broadband Experimental Data Configuration 1 at $4000RPM$ and Configuration 4 at $2000RPM$ Normalized on Blade Passage Frequency.

As expected, the tones at both scales line up directly on top of each other, with the $0.914m$ scale having consistently louder tones than the $0.457m$ scale. To potentially account for the tone difference, the performance parameters were investigated. The thrust for Configuration 1 at $4000RPM$ was about $54.8N$, and for Configuration 4 at $2000RPM$ was $205N$. It is expected that the steady loading tonal noise should approximately scale with the thrust squared, so the difference in noise should roughly be $10\log_{10}\left(\frac{T_1^2}{T_4^2}\right) = 10\log_{10}\left(\frac{(54.8N)^2}{(205N)^2}\right) \approx -11.5dB$. The sign of this result makes sense, since the larger scale is expected to produce more thrust and therefore louder noise. However, its magnitude is much greater than seen in Figure 4.20, where the greatest difference in tones is about $7dB$. Of course, this analysis may be limited since the performance parameters were averaged over the full time-series data, whereas the spectra shown are from the sequestered time-series data. This may suggest that the steady loading noise was not fully accountable for the difference in the tones at the BPF, but perhaps the tones may be dominated by TIN instead. This is supported by the idea that the larger propeller will further stretch and distort the turbulence in the environment as it is drawn into the face of the propeller, resulting in a greater increase in TIN, coalescing in louder tones and stronger harmonics.

4.2.5 Comparison of All Configurations

Other interesting variables that were also investigated alongside propeller size include pitch angle (Configuration 2) and turbulence trips (Configuration 3). As a comprehensive overview, all configurations are compared to each other to observe all their effects. Figure 4.21 shows the U-component of wind velocity data for all configurations, and Table 4.5 shows the sequestering windows considering $0.5m/s < u_{wind} < 3m/s$. Note that the sequestering windows considering $-1m/s < u_{wind} < 0.5m/s$ are taken to be elsewhere within the $32s$ sampling period. Figure 4.22 shows the sequestered broadband noise based on $0.5m/s < u_{wind} < 3m/s$ for all configurations at all rotational speeds.

Tip Speed (m/s)	**57.5**	**67**	**76.6**	**86.1**	**95.8**
Configuration 1	$7s$-$32s$	$12s$-$20s$	$0s$-$7s$	$4s$-$31s$	$0s$-$12s$
Configuration 2	$20s$-$32s$	$0s$-$20s$	$23s$-$32s$	$0s$-$32s$	$9s$-$17s$
Configuration 3	$20s$-$32s$	$0s$-$15s$	$15s$-$32s$	$0s$-$10s$	$5s$-$16s$
Configuration 4	$15s$-$32s$	$18s$-$32s$	$0s$-$10s$	$8s$-$15s$	$5s$-$15s$

Table 4.5: Sequestering Windows Considering $0.5m/s < u_{wind} < 3m/s$ of All Configurations.

At all propeller speeds, Configuration 4 appears dominant up to about $3000Hz$. From $3000Hz$ to $6000Hz$, Configuration 4 has a similar noise level to the other configurations. Generally, Configuration 2 appears relatively quieter than other configurations, which is expected since a slightly lower pitch angle would decrease thrust and therefore decrease noise. There are exceptions at tip speeds of $57.5m/s$ and $86.1m/s$. At the former tip speed, this

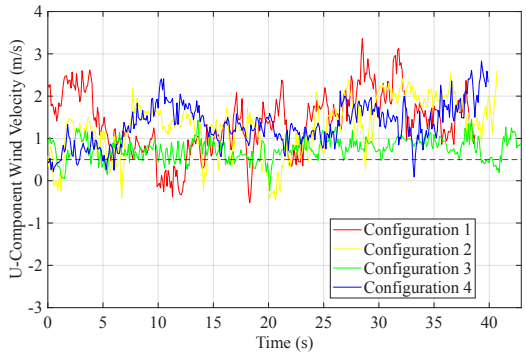

(a) $\vec{V}_{Tip} = 57.5m/s$.

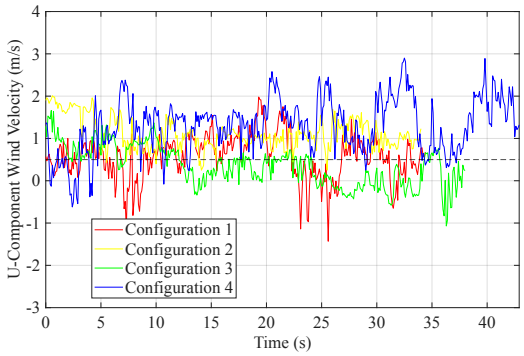

(b) $\vec{V}_{Tip} = 67m/s$.

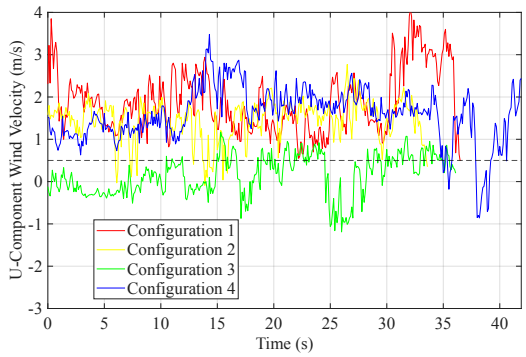

(c) $\vec{V}_{Tip} = 76.6m/s$.

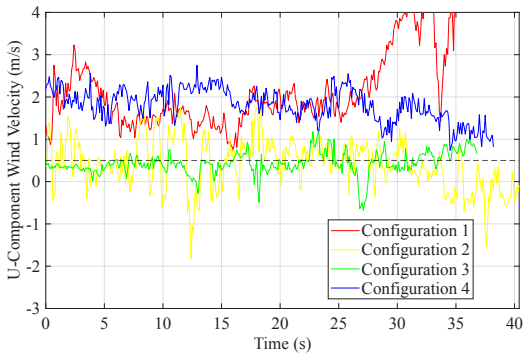

(d) $\vec{V}_{Tip} = 86.1m/s$.

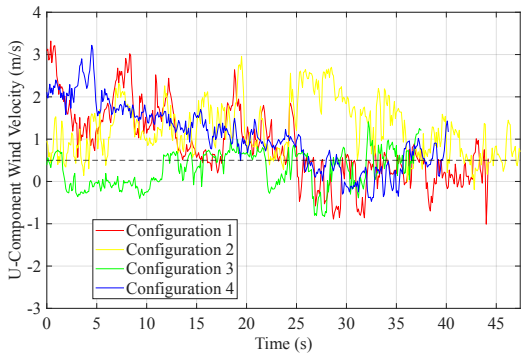

(e) $\vec{V}_{Tip} = 95.8m/s$.

Figure 4.21: Comparison of u_{wind} of Wind for All Configurations and Propeller Speeds.

may simply be due to a low tip speed such that differences in configurations may not yet be significant, as seen by the low variation in the broadband noise among configurations around $2000Hz$ to $5000Hz$. At the latter tip speed, this discrepancy is likely due to difficulties in sequestration, which will be discussed in more detail shortly. It would be expected that Configuration 3 would be louder than Configuration 1 since the addition of turbulence trips would increase trailing edge noise, although this is not consistently seen in Figure 4.22. In

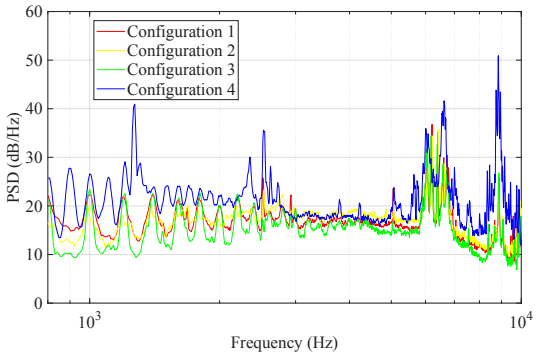

(a) $\vec{V}_{Tip} = 57.5m/s$.

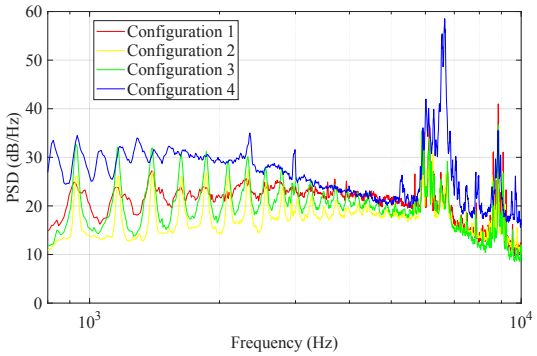

(b) $\vec{V}_{Tip} = 67m/s$.

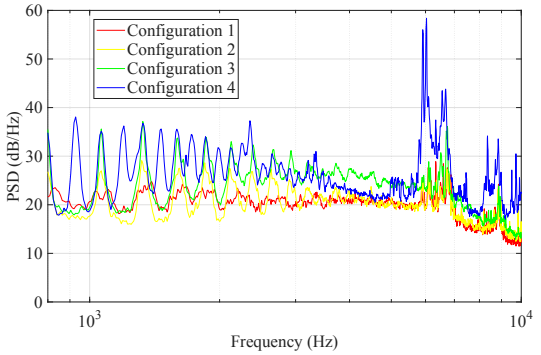

(c) $\vec{V}_{Tip} = 76.6m/s$.

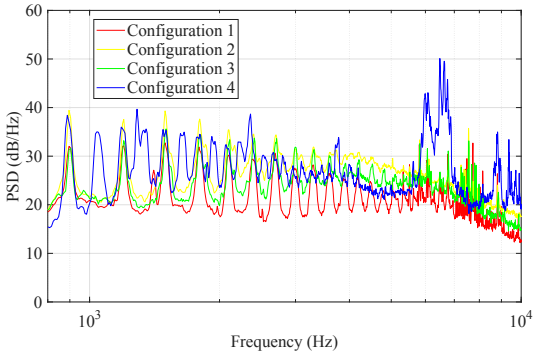

(d) $\vec{V}_{Tip} = 86.1m/s$.

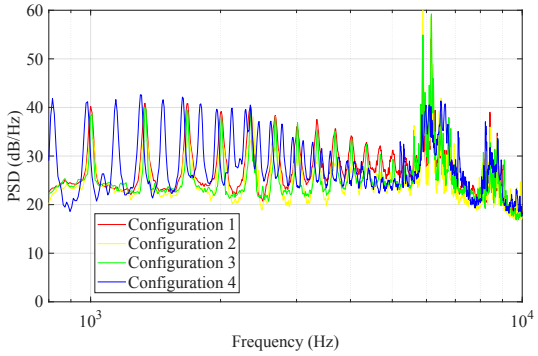

(e) $\vec{V}_{Tip} = 95.8m/s$.

Figure 4.22: Comparison of Sequestered ($0.5m/s < u_{wind} < 3m/s$) Broadband Noise of Microphone 1 for All Configurations and Propeller Speeds.

comparison to Configuration 1, there does not appear to be a consistent pattern with propeller speed, which may suggest there are still other environmental conditions affecting the spectra unaddressed by this specific sequestering process. For example, at $\vec{V}_{Tip} = 67m/s$, Configuration 1 appears louder than Configurations 2 and 3, but at $\vec{V}_{Tip} = 86.1m/s$, Configurations 2 and 3 are louder than Configuration 1. This corresponds to lower U-velocities

at the former propeller speed and higher U-velocities at the latter propeller speeds. This would ideally be addressed by sequestration, but the wind velocities throughout the entire time-series of the two conditions are not very similar (the slower tip speed has wind velocities mostly below $1m/s$ and the faster tip speed has wind velocities mostly above $2m/s$), so even sequestration would not resolve their differences. This emphasizes the difficulty of outdoor acoustic field tests: the environmental conditions are practically impossible to control, and comparable conditions may be difficult to isolate.

4.3 Summary

The background noise at this facility was dominant below about $800Hz$, electrical and mechanical motor noise dominant around $6000Hz$ to $9000Hz$, and aerodynamic rotor noise dominant elsewhere. The signal-to-noise ratio of the quietest rotor noise configuration compared to the background noise was consistently positive above $800Hz$ on both test days. Frequency spectra presented in this chapter should be considered significant in such frequency ranges.

The sequestering process was performed by separating the time-series data based on the U-component of wind. Two conditions were considered: one where $0.5m/s < u_{wind} < 3m/s$, and one where $-1m/s < u_{wind} < 0.5m/s$. These conditions were selected to separate periods with small positive inflow velocities from periods with negative or near-zero inflow velocities. Spectra calculated from the former condition resulted in lower broadband noise than spectra calculated from the latter condition, typically by about $1dB$ to $3dB$ in the $2000Hz$ to $6000Hz$ frequency range. These results are consistent with the expected behavior of noise with steady loading, which would change with fluctuations in wind velocities.

Decomposition of the total spectra into broadband and tonal components revealed that an overwhelming majority of the noise is a broadband contribution. The most prominent tonal components were at the blade passage frequency, its harmonics, and motor noise frequencies. The former event is dependent on the number of rotor blades and its rotational speed, and the latter is a more consistent source dominant around $6000Hz$. The aerodynamic noise sources dominant are likely blade-wake interaction and turbulence ingestion noise, which explain the large broadband contribution even at the blade passage frequencies.

The experimental broadband noise spectra were compared to the Gill-Lee Spectrum Model (GLSM) [8], and in general, the level of the GLSM were significantly greater than the experimental data, but their shapes were similar with the exception of the broadband peak in the GLSM occurred at a higher frequency than the experimental data by about $2000Hz$. Sequestering the time-series data with the condition of $-1m/s < u_{wind} < 0.5m/s$ resulted in experimental data with spectral levels similar to that of the GLSM. This is consistent with the construction of the GLSM, which was trained on acoustics of rotors operating at hover.

Comparing the spectra from the large scale propeller to the small scale propeller shows

the expected patterns in tones at the BPF and its harmonics. The larger propeller produced louder tonal noise than the smaller propeller by about $7dB$, whereas the thrust measurements suggest the difference should be approximately $11dB$. However, these thrust measurements were not completely synchronized to the acoustics, so the exact value of $11dB$ may not be completely accurate. The broadband noise at the large scale appears to be louder and peaks at a lower frequency compared to the smaller scale, which is consistent with the GLSM predictions.

All configurations at each rotational speed were sequestered with the condition of $0.5m/s < u_{wind} < 3m/s$ and compared among each other. Generally, Configuration 4 was louder than all other configurations around $1000Hz$ to $6000Hz$, which is consistent with larger propellers producing louder broadband noise. Configuration 2 behaved generally as expected relative to Configuration 1, namely being quieter due to decreased pitch angle and therefore decreased thrust and noise. Configuration 3 did not consistently behave as expected relative to Configuration 1, namely that the addition of turbulence trips unexpectedly did not result in a consistent increase in broadband noise. Comparing all the wind velocity data showed that some configurations did not have any wind conditions similar to other configurations, so sequestration would not yield any comparable data, which may account for these discrepancies. These uncontrollable environmental conditions create a large difficulty in obtaining comparable data during outdoor acoustic field tests.

There are many considerations to improve upon the experiment presented in this chapter. First, an exact ground board calibration should be conducted. This can be done by replacing the rotor with a monopole speaker with a white noise output and calculating calibrations in a similar methodology to Chapter 3. Second, wind velocity data collection should be synchronized with the acoustic data collection. This would allow for an additional component in the cross-spectral matrix and more accurate and in-depth analyses. Third, synchronized thrust coefficient data should also be collected. This would allow for a more accurate calculation of the GLSM since a sequestered thrust coefficient can be used.

These results can be compared to acoustic data gathered in a more controlled environment. These comparisons are important to understand how outdoor experiments are relevant and to what degree they are relevant. Acoustic data were gathered in a controlled environment, the results of which will be presented in the next chapter.

Chapter 5

VTSMART Experiment

The $0.457m$ propeller was tested again in the VTSMART. The $0.914m$ propeller was not tested because of size limitations, emphasizing the importance of relating outdoor tests to indoor tests. These data provided a control to compare against the data collected during the Drone Park experiment.

5.1 Experiment Setup

This experiment took place within the VTSMART as described in Section 2.3. To reiterate the most pertinent specifications, this facility is an open jet wind tunnel with an inlet cross section of $0.762m \times 0.762m$. It has a maximum flow speed of about $40m/s$ and is anechoic down to $420Hz$.

Techsburg's $0.457m$ propeller and propeller stand from the previous experiment in the Drone Park were reused in this experiment. The propeller stand was easily dismounted from the trailer and placed within the tunnel, aligning the center of the propeller disk with the horizontal center of the jet exit and $0.0381m$ above the vertical center of the jet exit. None of the components were changed, and the same stand, load cell, motor, and propeller from the Drone Park experiment were used in this experiment. The general setup of the propeller in the test section is shown in Figure 5.1.

Six B&K Type 4190 microphones were connected to a single B&K 3050-A-060-R DAQ to synchronously collect acoustic pressure data from the propeller. Five of the six microphones were mounted using a stand array, and the sixth microphone was mounted on a separate stand. The first five microphones were mounted along a line parallel to the axis of rotation and in the same horizontal plane as the rotor center. They were evenly spaced by 10°, starting from 10° upstream of the rotor plane to 30° downstream of the rotor plane. The sixth microphone was also placed in the same horizontal plane as the rotor center and located $1.02m$ away from the axis of rotation and $1.30m$ downstream of the rotor plane. Figure 5.2 shows the schematic of the microphone numbering and positions relative to the center of the propeller disk. This shows a bird's eye view of the layout, and all microphones were in the same horizontal plane as the center of the propeller disk. Again, all acoustic data were sampled for $32s$ at a rate of $65536Hz$. Note that Microphone 2 is in the rotor plane, Microphones 1, 2, 3, 4, and 5 are equally spaced by 10° between adjacent microphones, and

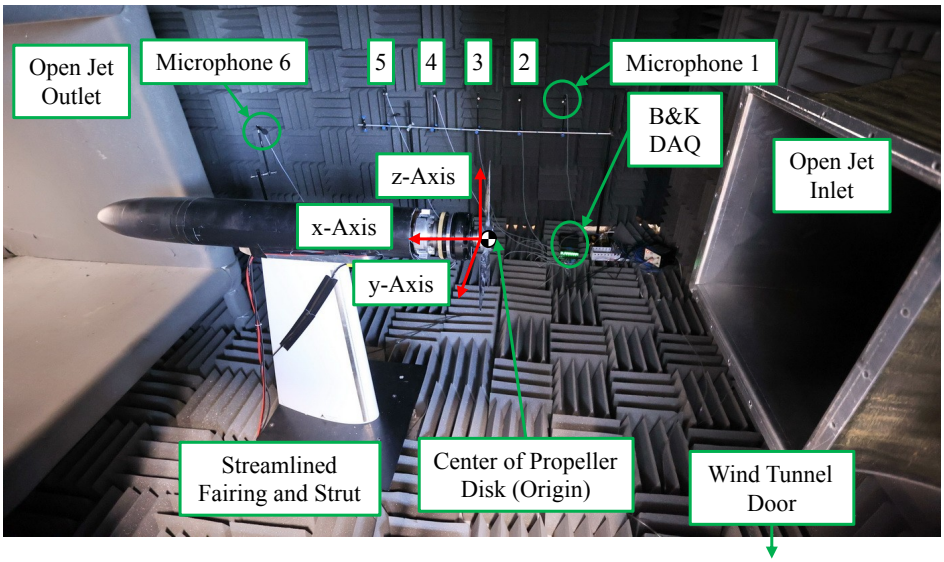

Figure 5.1: Overview of VTSMART Experiment Setup Inside Test Section with $0.457m$ Diameter Propeller.

that all microphones are oriented such that they are directly pointing towards the rotor. Also note that in this view, the rotor centerline is aligned with the center of the open jet inlet in the y-direction.

Due to size limitations, only the $0.457m$ diameter propeller was tested in the VTSMART. Specifically, the $0.914m$ diameter propeller would not be fully submerged within the $0.762m \times 0.762m$ open jet inlet cross section. Other variables included tip angle, turbulence trips, tip drooping, propeller rotational speed, and tunnel speed. The tested configurations are presented comprehensively in Table 5.1.

5.2 Results

The results of this experiment were also analyzed using spectral analysis methods. Similar to the previous Drone Park experiment in Chapter 4, background noise data were gathered, the rotor noise data were decomposed into broadband and tonal components, and comparisons to the Gill-Lee Spectrum Model (GLSM) [8] were performed. Ground boards were not used in this experiment, so such corrections were unnecessary. Also, sequestering the time-series data was not required either since the wind tunnel flow was constant. Finally, the spectra from the Drone Park experiment were compared to the spectra from this experiment, which had to be adjusted due to the difference in distance.

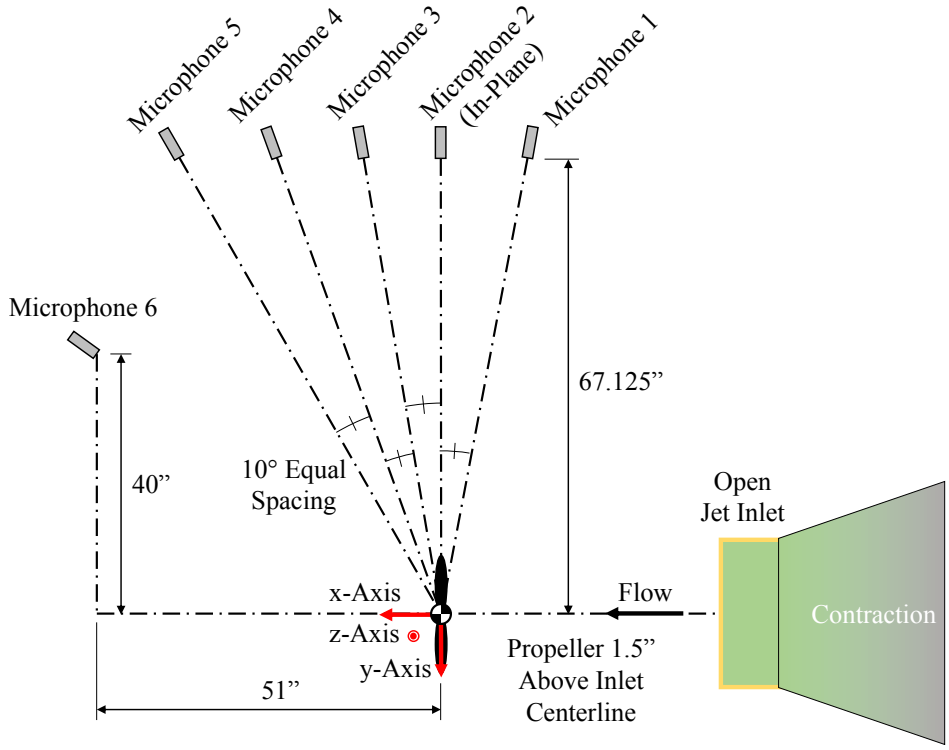

Figure 5.2: Top-Down View Schematic of VTSMART Experiment.

Table 5.1: VTSMART Experiment Test Matrix.

	Pitch Angle	7°	9°		
	Turbulence Trips	No	No		Yes
Tunnel Speed	**Tip Droop** / **RPM**	No	No	Yes	No
Off	2400	✓	✓	✓	✓
	2800	✓	✓	✓	✓
	3200	✓	✓	✓	✓
	3600	✓	✓	✓	✓
	4000	✓	✓	✓	✓
$4m/s$	2400	✓	✓	✓	✓
	2800	✓	✓	✓	✓
	3200	✓	✓	✓	✓
	3600	✓	✓	✓	✓
	4000	✓	✓	✓	✓

5.2.1 Background Noise

Before examining the acoustics of the rotor, the background noise of the facility should first be understood. Background noise within the facility was collected for the tunnel turned off, the tunnel turned on but no flow, and the tunnel operating with flow at $4m/s$. Figure 5.3 shows the background noise for these tunnel speeds. For ease of comparison, Figure 5.3d shows the average spectra of each tunnel condition.

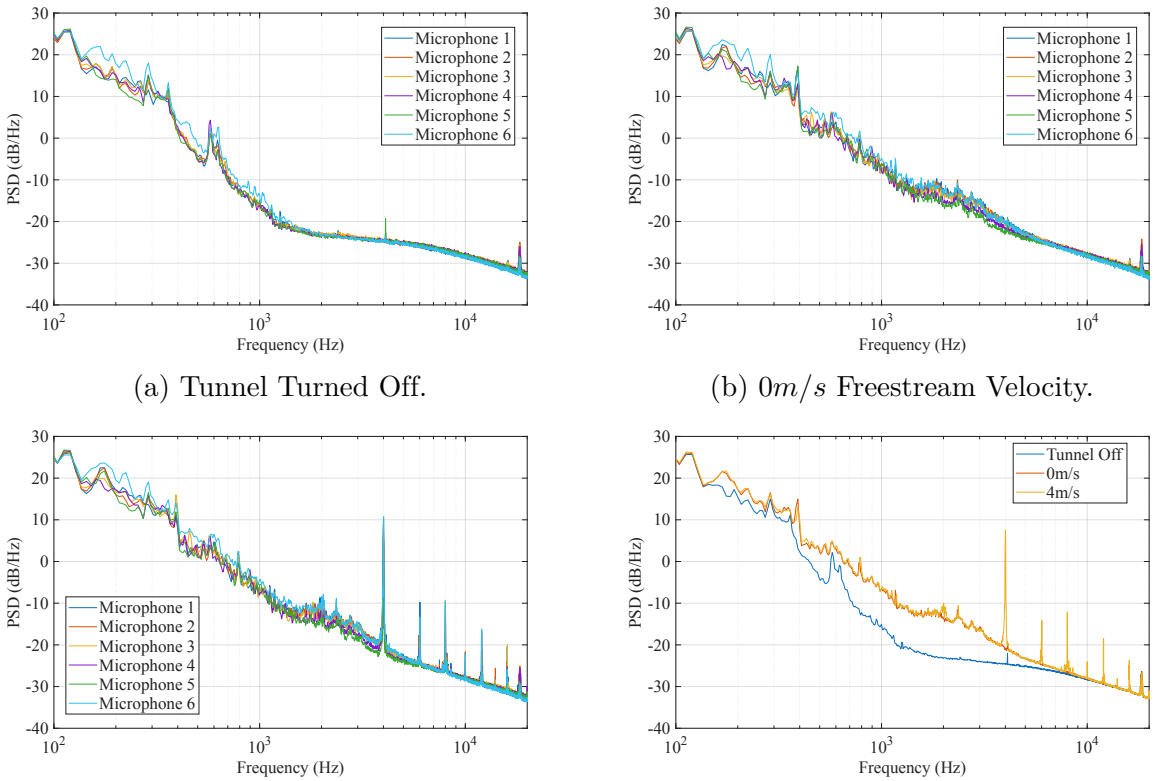

(a) Tunnel Turned Off.

(b) $0m/s$ Freestream Velocity.

(c) $4m/s$ Freestream Velocity.

(d) Average Spectra Comparison.

Figure 5.3: VTSMART Background Noise at Relevant Tunnel Conditions.

It appears that the microphone position has little to no effect on the background noise measured, with Microphone 6 measuring very slightly louder levels. The decibel range among the microphones peaks at $8dB$ around $200Hz$, a frequency that is not considered in the comparison to the Drone Park data, and averages around $1dB$ above $1000Hz$. This is consistent at all tunnel speeds with the exception of the tonal spikes at $400Hz$ for the $4m/s$ flow, but the absolute value peaks around $10dB$, which is much quieter than measured rotor noise, which will be shown in more detail shortly. Notice that the tunnel condition at $0m/s$ freestream velocity is difficult to see because it is very similar to the $4m/s$ freestream velocity condition. Also note that with the tunnel on but with no flow, it is louder than when the tunnel is off in the $400Hz$ to $4000Hz$ frequency range. This is due to the electrical motor

drive noise caused by simply turning the tunnel on. Also, notice at every $2000Hz$ starting from $4000Hz$, there are large spikes in the spectra with $4m/s$ flow that are not present with $0m/s$ flow. The reason for this discrepancy is the electrical and mechanical motor noise from the tunnel fan. Otherwise, they are similar.

These background noise levels should also be subtracted from the raw data. Unlike in the Drone Park experiment, background noise subtraction can be done in the VTSMART because it is a more controlled environment, and the background noise is more deterministic. This is done by a simple mean-square-pressure subtraction as shown in Equation 5.1.

$$G_{pp,Subtracted} = G_{pp,Rotor} - G_{pp,Background} \tag{5.1}$$

This corrected mean-square-pressure spectra can then be converted to a decibel level according to Equation 2.1. An example of this can be seen in Figure 5.4. This shows the background noise correction results for the average microphone spectra of Configuration 1, which considers a 9° pitch angle without turbulence trips or tip droop, at $2400RPM$ with the tunnel turned off and at $4m/s$. The same configuration numbering from Table 4.2 will be used in this chapter as well, but note that further specification about the experiment and tunnel speed will be required to fully define a spectrum.

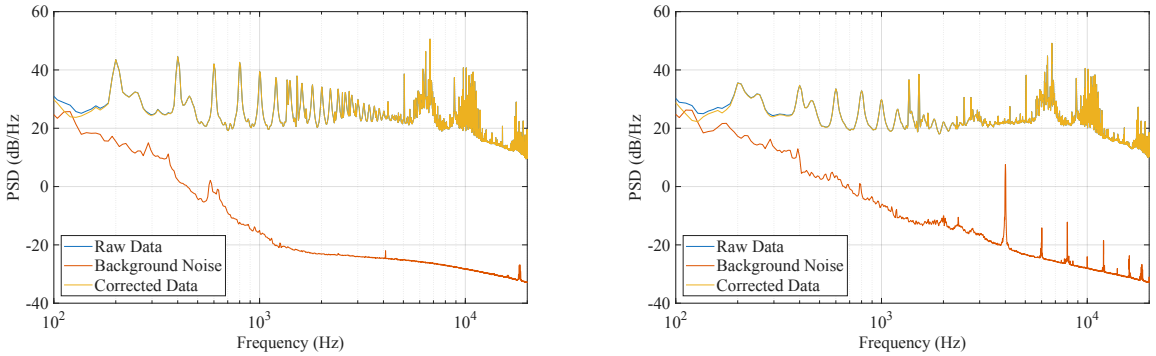

(a) Tunnel Turned Off.

(b) Tunnel at $4m/s$.

Figure 5.4: Average Background Noise Corrections for Configuration 1 at $2400RPM$.

Notice that the raw data from the rotor noise is much louder than the background noise at both tunnel speeds, which is reflected in the corrected spectra since this lies almost directly on top of the raw spectra. The background noise is only appreciable around the $100Hz$ to $200Hz$ range, and even in this range, the rotor noise is louder than the background noise by at least $1dB$. To observe this in more detail, the signal-to-noise ratio (SNR) was calculated for this configuration at both tunnel conditions. Figure 5.5 shows these distributions as a function of frequency for all microphones.

Figure 5.5 clearly shows that even for one of the quietest propeller configurations, the SNR is positive throughout the entire frequency spectrum between $100Hz$ and $20000Hz$,

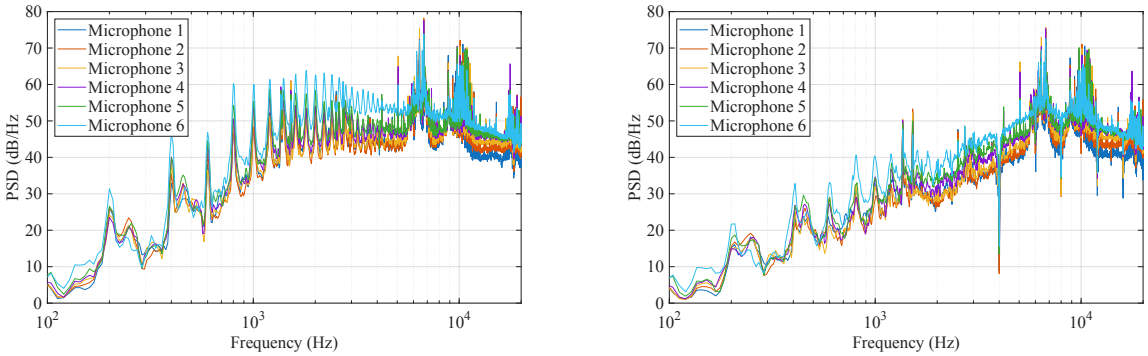

(a) Tunnel Turned Off. (b) Tunnel at $4m/s$.

Figure 5.5: Signal-to-Noise Ratios for Configuration 1 at $2400RPM$.

reaching a minimum of about 1 around $120Hz$. These observations increase confidence that the measured noise is dominated by rotor noise at least in the middle to high frequency ranges and likely throughout the entire frequency range, and that further analyses will be relevant to rotor noise.

5.2.2 Time Invariance

The spectrograms of Configuration 1 at $4000RPM$ with the tunnel turned off and with $4m/s$ flow were plotted in Figure 5.6 to ensure that the results are constant with respect to time. For brevity, only the in-plane Microphone 2 position is shown.

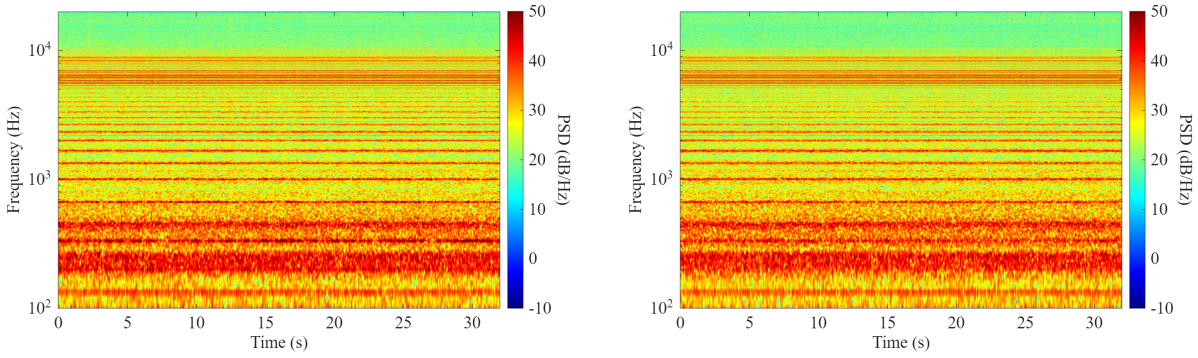

(a) Tunnel Turned Off. (b) Tunnel at $4m/s$.

Figure 5.6: Microphone 2 Spectrograms of Configuration 1 at $4000RPM$ at Both Tunnel Conditions.

Firstly, the two spectrograms seem nearly identical, and they are in fact very similar, but further analysis with line spectra in the next section, Section 5.2.3, will show some distinct

differences. More importantly, these spectrograms clearly show that the indoor tests in the VTSMART facility are much more controlled than the outdoor experiment at the Drone Park. Similar to the analysis done to the Drone Park data, directivity of the time-varying OASPL can also be plotted to observe the combined effects of observer position and time. This is shown in Figure 5.7 for Configuration 1 at $4000RPM$ with the tunnel turned off and with $4m/s$ flow.

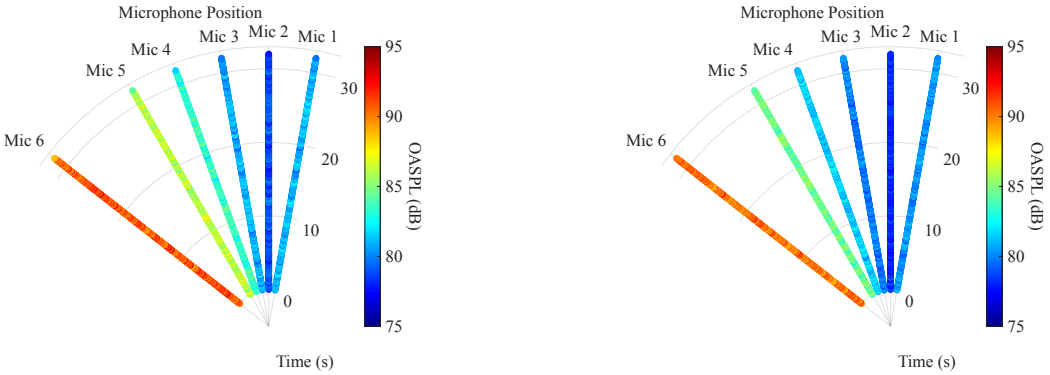

(a) Tunnel Turned Off.

(b) Tunnel at $4m/s$.

Figure 5.7: Directivity of OASPL Over Time of Configuration 1 at $4000RPM$ at Both Tunnel Conditions.

Note that each microphone has a different radial distance to the origin, so the OASPL for each microphone is normalized to the distance of Microphone 2 ($1.71m$) so that the elevation angle is the only factor in observer position. This calculation is similar to that presented in Equation 5.2. Even with this distance normalization, Microphone 6 still experiences significantly louder sound, which is unsurprising since it is expected that the rotor behaves similar to a dipole, with the majority of the broadband noise directed along the axis of rotation and a minimum amount of noise directed in the rotor plane.

These results showing time-invariant noise suggest that these data do not have to be sequestered, and spectra averaged over the entire sampling period can be considered accurate representations of the observed behavior.

5.2.3 Broadband and Tonal Components

These spectra were separated into broadband and tonal components exactly as done to the data obtained from the Drone Park experiment. The components of Configuration 1 at $4000RPM$ with the tunnel turned off and at $4m/s$ are shown in Figures 5.8 and 5.9, respectively. Furthermore, these plots display the 15° upstream Microphone 1, in-plane Microphone 2, and downstream Microphone 6 positions.

Unsurprisingly, this decomposition reveals that the majority of the noise is again domi-

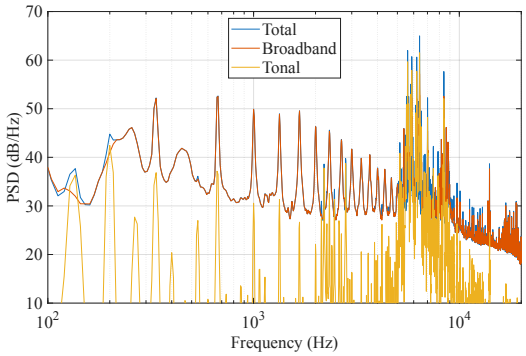

(a) 15° Upstream Microphone 1.

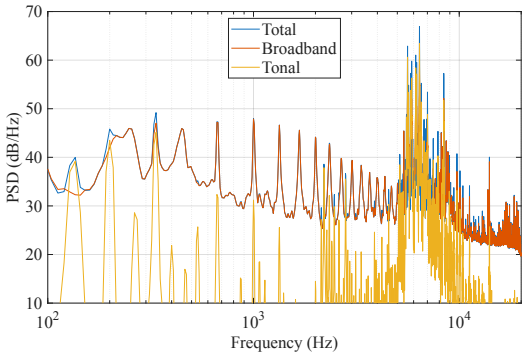

(b) In-Plane Microphone 2.

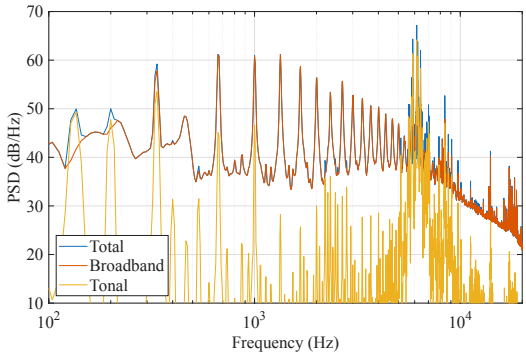

(c) Downstream Microphone 6.

Figure 5.8: Broadband and Tonal Components of Configuration 1 at $4000RPM$ with No Wind Tunnel Flow.

nated by the broadband component, regardless of inflow condition or microphone position. At the BPF, the tonal component is comparable, but the broadband comprises most of the noise at its harmonics. The tonal component dominates at the motor noise frequencies around $5000Hz$ to $9000Hz$. These results are similar to and corroborate the results from the Drone Park experiment. One interesting feature not seen in the Drone Park results are the tones around $130Hz$ and $200Hz$. This decomposition reveals that these features are truly tonal components. These tones are likely associated with multiples of the shaft rate, frequencies at which any imbalances in the system would generate noise. Furthermore, these tones would be more difficult to identify in the outdoor Drone Park experiment due to elevated background noise levels. However, identifying the cause of these features is not of utmost importance since they occur below $800Hz$ and comparisons to the Drone Park results are less valid below $800Hz$ due to background noise.

Another interesting observation can be seen when comparing the levels between the two tunnel speeds. Figure 5.10 shows the broadband components for Configuration 1 at both tunnel speeds on the same plot at each RPM on their own subfigure.

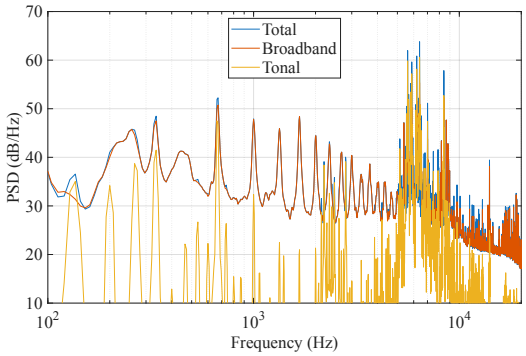

(a) 15° Upstream Microphone 1.

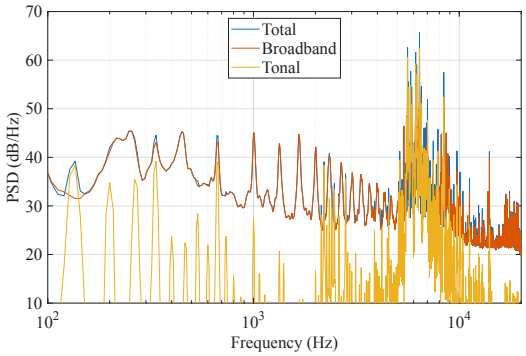

(b) In-Plane Microphone 2.

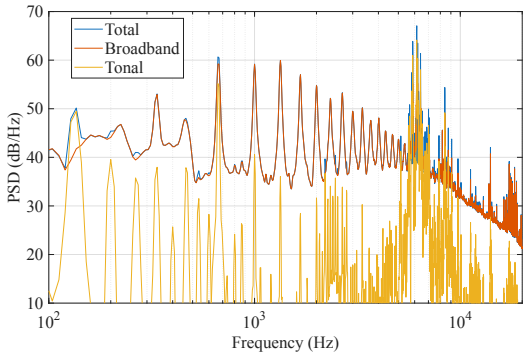

(c) Downstream Microphone 6.

Figure 5.9: Broadband and Tonal Components of Configuration 1 at $4000RPM$ with $4m/s$ Wind Tunnel Flow.

At each RPM, the tones appear to behave similarly and as expected: the introduction of flow reduces thrust, which results in quieter tones. This effect is more visible at lower RPMs, which has a difference in tones by about $10dB$ at the BPF and a few of the first few harmonics, whereas the higher RPMs has quieter tones by about $3dB$ at the BPF and a few of the first few harmonics.

Figure 5.11a shows the broadband component for Configuration 1 at $4000RPM$ at both tunnel speeds on the same plot for ease of comparison. Additionally, the GLSM was calculated for these conditions and plotted on the same plot.

Throughout the entire frequency spectrum, the broadband portion appears to be very similar between the two tunnel speeds, the only major difference being that the condition with the tunnel turned off may have a little bit more uncertainty in the spectrum. More obvious is the difference in the tones, which still appear in the broadband component spectrum. At the tonal peaks, the tunnel condition with $4m/s$ inflow is quieter than the condition with the tunnel turned off up to $5dB$, averaging around $2dB$ to $3dB$. Although perhaps not groundbreaking, this reinforces the theory that a higher flow into the propeller results in lower

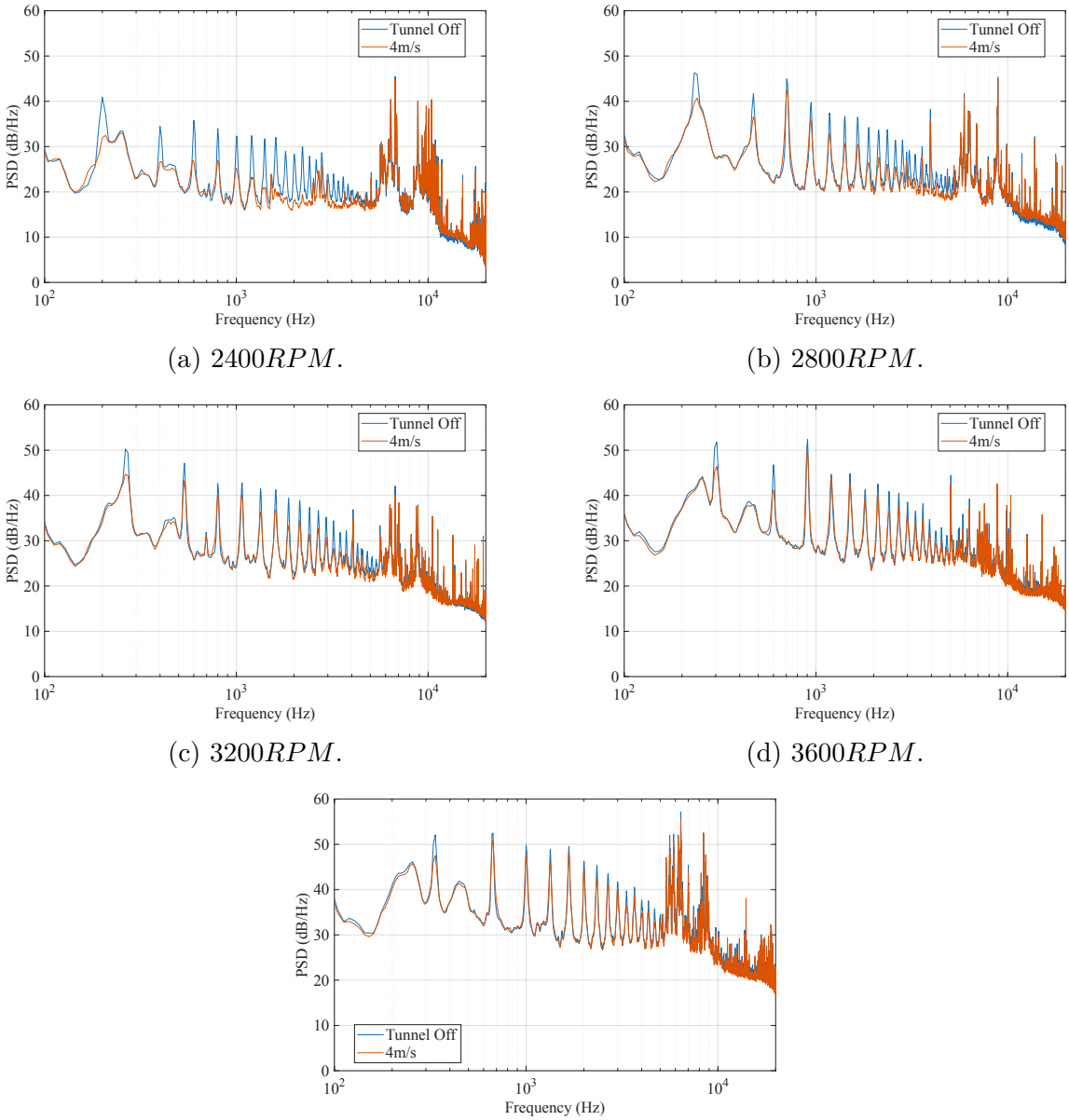

(a) $2400RPM$.

(b) $2800RPM$.

(c) $3200RPM$.

(d) $3600RPM$.

(e) $4000RPM$.

Figure 5.10: Comparison of Tunnel Inflow Conditions on Broadband Components of Microphone 1 of Configuration 1.

noise due to lower thrust and increased separation between the wake and propeller blades. Additionally, this may suggest there exist some stochastic flow interactions at $4000RPM$, perhaps due to the inflow velocity failing to convect such structures sufficiently far downstream of the rotor. Further studies involving flow characterization may be necessary to identify and verify this.

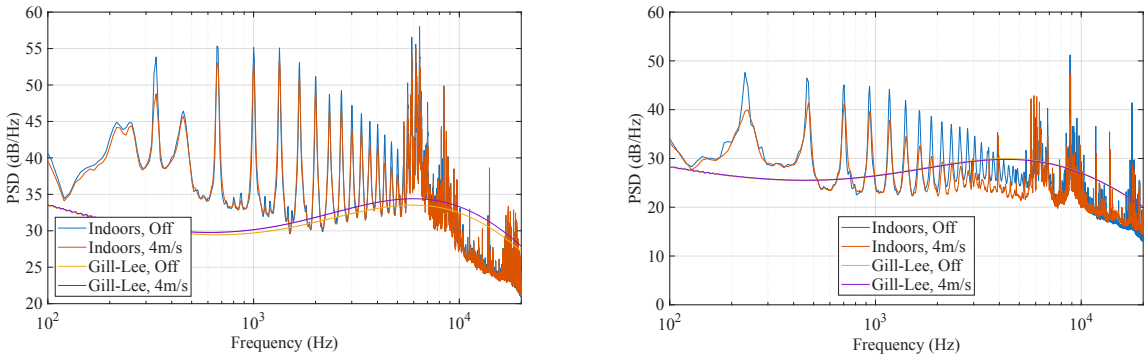

(a) Configuration 1 at $4000RPM$. (b) Configuration 3 at $2800RPM$.

Figure 5.11: Comparison of Tunnel Inflow Conditions on Average Broadband Components for Experimental Data and GLSM Predictions.

The GLSM produces curves that are not only similar to each other, but also similar to the experimental data. The two predictions are nearly identical at low frequencies up until about $1000Hz$, where the $4m/s$ flow prediction starts to sound louder than the prediction for the no-flow condition by at most $1dB$. Above about $7000Hz$, the GLSM curves diverge from the experimental data, the former being significantly louder than the latter. However, the slopes of all spectra appear similar above $10000Hz$, a similarity that is not observed from the Drone Park data (recall Figure 4.16, where the experimental data show a steeper slope above $10000Hz$). Better similarity between the GLSM and the indoor experiment than between the GLSM and the outdoor experiment may be explained by more accurate performance data. Recall that the performance parameters were not collected simultaneously to acoustics in either experiment. In the outdoor experiment, the lack of simultaneous data collection affects the repeatability more since the wind conditions may vary from instant to instant. However, in the indoor experiment, these effects would be much less, since it was shown that the data collected at the VTSMART facility are time-invariant and the data collected at one instant may still be representative of the data collected at another instant since the environmental conditions are consistent.

Similar trends can be observed from the broadband spectra for Configuration 3 at $2800RPM$. Figure 5.11b shows the average broadband spectrum at both tunnel conditions and their respective GLSM predictions. Again, the tones are much louder with the tunnel turned off than with $4m/s$ flow. Additionally, the former's broadband trend is slightly louder in the $2000Hz$ to $5000Hz$ range. The GLSM predictions match each other more closely for this configuration, but do not match the levels of the experimental data as well, although it is important to remember that the conditions in these experiments may be edge cases for the GLSM or even fall outside the range of the data used to train it. As with the previous comparison, the shape of the GLSM predictions matches the experimental data very well, although the experimental broadband trend appears to peak around $4000Hz$ and the GLSM predicts a peak around $6500Hz$.

5.2.4 Effects of Test Facility

Perhaps the most important analysis to perform is relating the outdoor experiment to the indoor experiment. To maintain maximum comparability, the relative microphone positions should be the same between both experiments. There are only two microphones that have the same angle relative to the rotor: Microphone 2 from the VTSMART experiment and Microphone 7 from the Drone Park experiment are both in-plane, and Microphone 5 from the VTSMART experiment and Microphone 9 from the Drone Park experiment are both 30° downstream of the rotor plane. Therefore, these analyses will focus on these two microphone positions.

Furthermore, the microphones are much closer to the rotor in the VTSMART experiment than in the Drone Park experiment. These spectra must be corrected for this distance discrepancy for valid comparability. In the following analyses, the spectra from the VTSMART experiment were scaled such that they are comparable to the Drone Park experiment. This was done by an inverse square law relationship, which is shown in Equation 5.2.

$$G_{pp,Corrected} = \frac{d^2_{Drone\ \ Park}}{d^2_{VTSMART}} G_{pp,Raw} \tag{5.2}$$

For the in-plane position, this correction factor is $\frac{d^2_{Mic\ 7,Drone\ \ Park}}{d^2_{Mic\ 2,VTSMART}} \approx \frac{(5.03m)^2}{(1.71m)^2} \approx 8.7$, and for the 30° downstream position, this correction factor is $\frac{d^2_{Mic\ 9,Drone\ \ Park}}{d^2_{Mic\ 5,VTSMART}} \approx \frac{(4.92m)^2}{(1.97m)^2} \approx 6.24$. After applying these corrections, the PSD can be calculated as per Equation 2.1.

These corrections were applied to the VTSMART experiment broadband spectra, and the comparison between these and the Drone Park experiment for Configuration 1 at $4000RPM$ at both in-plane and 30° downstream positions are shown in Figure 5.12.

First, to note the differences, the tones as observed during the indoors experiment are significantly louder than the outdoors experiment, even considering the $4m/s$ flow condition. One explanation for this increased tonal noise could be the failure of the inflow velocity to convect the wake of the propeller sufficiently downstream to avoid recirculation. This effect is exacerbated in the confined space of a wind tunnel, which would force the propeller to reingest its wake. This effect would be reduced in an outdoor environment, where the propeller's open surroundings may allow it to ingest cleaner air than its wake, further emphasizing the importance and necessity of reliable outdoor acoustic tests. In any case, wake recirculation would result in an increase in TIN and the perceived tones as seen in Figure 5.12. Other major differences can be seen below $1000Hz$, but they will be disregarded in these analyses since the data is not comparable in the Drone Park experiment anyways.

At both microphone positions, the broad spectral features between the two experiments match best considering a small positive inflow better than considering a near-zero inflow. For the former condition, the broad spectral features between the two experiments are within

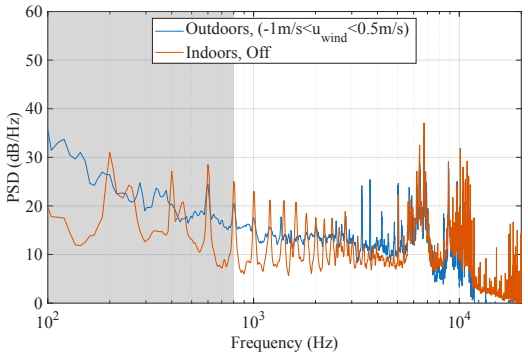

(a) In-Plane, Near-Zero Inflow.

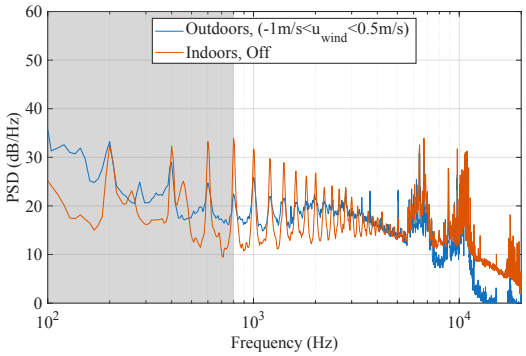

(b) 30° Downstream, Near-Zero Inflow.

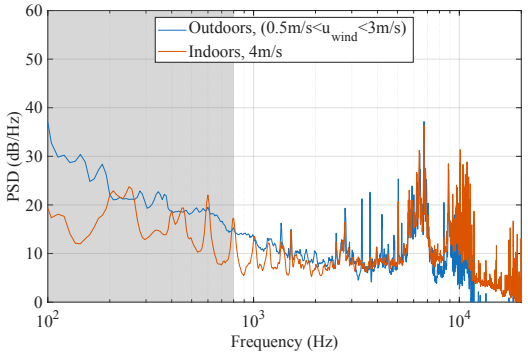

(c) In-Plane, Small Positive Inflow.

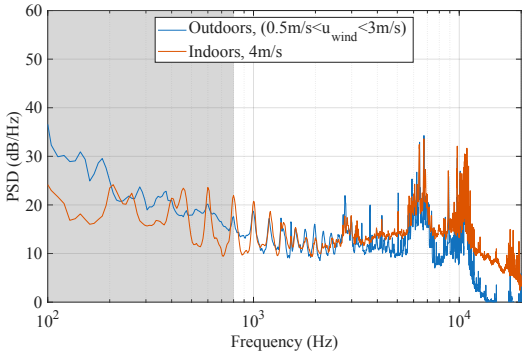

(d) 30° Downstream, Small Positive Inflow.

Figure 5.12: VTSMART Experiment vs. Drone Park Experiment Broadband Spectra Comparison for Configuration 1 at $2400RPM$.

about $1dB$ to $2dB$ of each other, whereas the broadband noise from the near-zero inflow condition may differ by up to about $5dB$. However, looking at the same analysis for Configuration 3 at $2800RPM$ in Figure 5.13 suggests an even more interesting result.

The outdoor sequestered broadband noise considering $0.5m/s < u_{wind} < 3m/s$ matches well with the indoor broadband noise at $4m/s$ in the $2000Hz$ to $6000Hz$ range for both microphone positions. Not only that, but the outdoor sequestered broadband noise considering $-1m/s < u_{wind} < 0.5m/s$ matches well with the indoor broadband noise with the tunnel turned off. This is in line with expectations because the sequestering process separates periods with small positive inflow from periods with near-zero inflow, so it would make sense that similar conditions simulated indoors would yield similar spectra. To observe the effects of different sequestering conditions, Figure 5.14 better visualizes the differences between these spectra on a contour plot. Note that the frequency range is limited from $800Hz$ to $20000Hz$ to exclude the frequency range where the background noise is dominant in the Drone Park spectra.

These figures show the absolute value of the difference between the decibels. Figures

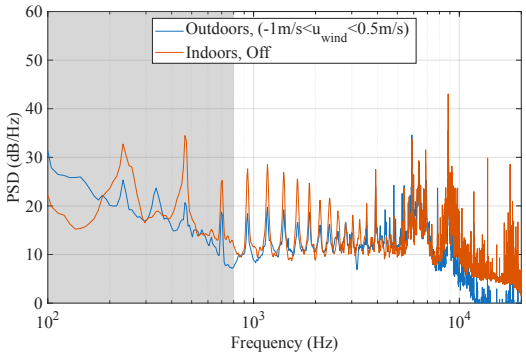

(a) In-Plane, Near-Zero Inflow.

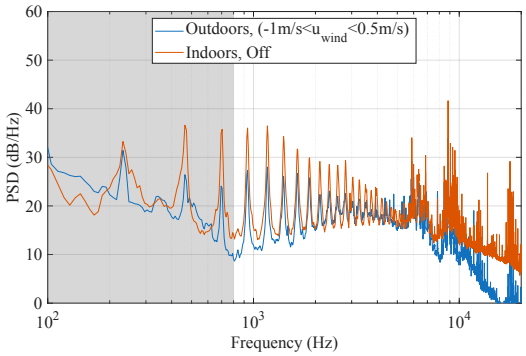

(b) 30° Downstream, Near-Zero Inflow.

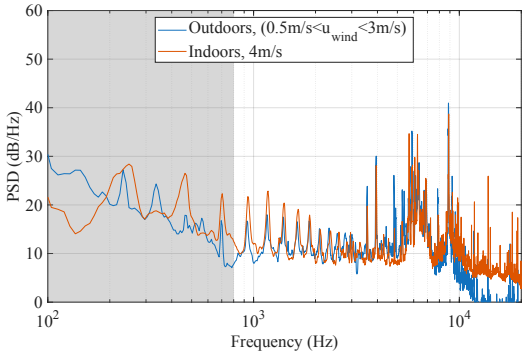

(c) In-Plane, Small Positive Inflow.

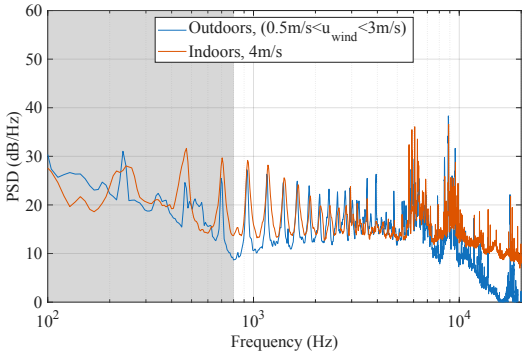

(d) 30° Downstream, Small Positive Inflow.

Figure 5.13: VTSMART Experiment vs. Drone Park Experiment Broadband Spectra Comparison for Configuration 3 at $2800RPM$.

5.14a and 5.14c show the microphone positions in the rotor plane, and Figures 5.14b and 5.14d show the microphone positions 30° below the rotor plane. Figures Figures 5.14a and 5.14b show the difference between the indoor data without flow and the full outdoor data, and Figures 5.14c and 5.14d show the difference between the indoor data with flow and the sequestered outdoor data considering $0.5m/s < u_{wind} < 3m/s$. Observe that these figures are dominantly blue in the $2000Hz$ to $6000Hz$ range, meaning that the differences between these spectra are well under about $5dB$. These differences are more exacerbated as RPM is increased, and the largest differences occur at the tones corresponding to the BPF and its harmonics. However, the differences in both broadband and tonal noise seem much lower when looking at Figures 5.14c and 5.14d than with Figures 5.14a and 5.14b, suggesting that sequestering the outdoor data makes it more similar to the indoor data with $4m/s$ flow than using the full outdoor data and comparing it with indoor data without any flow, although some more fine-tuning may be required to find even more comparable conditions.

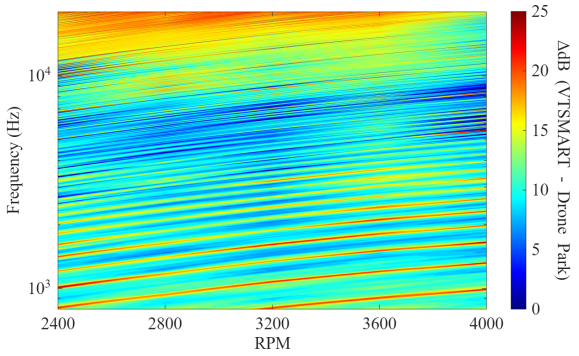

(a) In-Plane Position, $0m/s$ Versus Full.

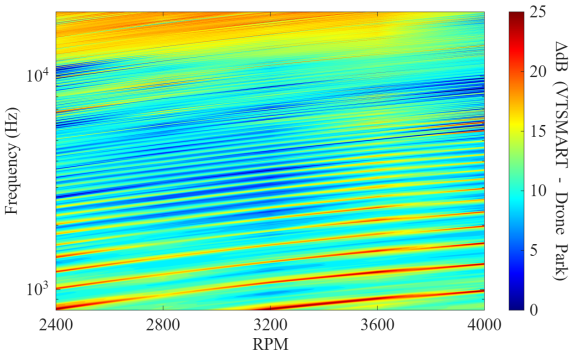

(b) 30° Downstream Position, $0m/s$ Versus Full.

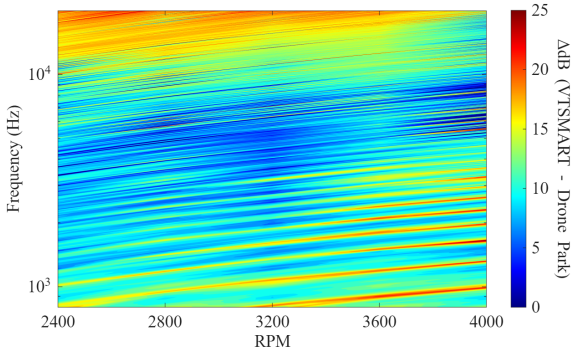

(c) In-Plane Position, $4m/s$ Versus Sequestered.

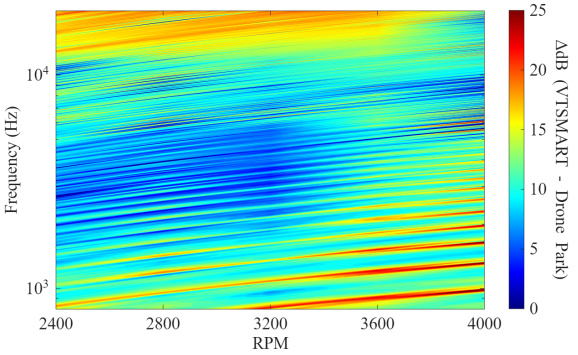

(d) 30° Downstream Position, $4m/s$ Versus Sequestered.

Figure 5.14: Broadband ΔPSD Between VTSMART Experiment vs. Drone Park Experiment for Configuration 3 at Various RPMs.

5.2.5 Comparison of All Configurations

All configurations were again compared to each other, with the exception of Configuration 4, since this involves the $0.914m$ diameter propeller, and this was not tested in the VTSMART facility. Figure 5.15 shows these spectra. For brevity, only the slowest, middle, and fastest rotational speeds are shown, and only Microphone 5 (30° downstream position) is shown, but both tunnel conditions are shown. Furthermore, the frequency range is limited to $800Hz$ to $6000Hz$ to focus on the primary broadband frequencies.

Holding the tip speed constant, increasing the tunnel speed appears to reduce the magnitude of the tones up to about $10dB$ at the slowest tip speed. This effect is most significant at the slower tip speeds, whereas the higher tip speeds have a reduction in tones by about $2dB$. The tunnel speed appears to have little effect on the general broadband trend. These two points (less significant effect on tones at higher propeller speed, and little effect on broadband noise at all propeller speeds) support the hypothesis that $4m/s$ is too slow to convect broadband structures far enough downstream of the propeller to avoid aerodynamic

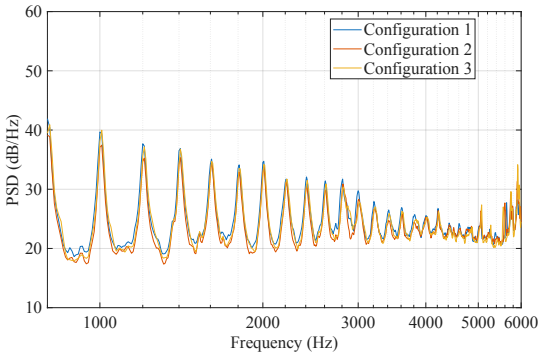

(a) $\vec{V}_{Tip} = 57.5m/s$, Tunnel Turned Off.

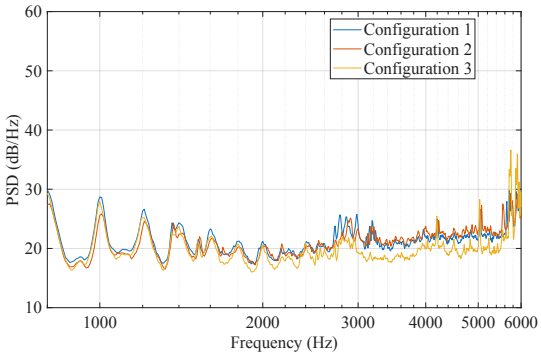

(b) $\vec{V}_{Tip} = 57.5m/s$, Tunnel at $4m/s$.

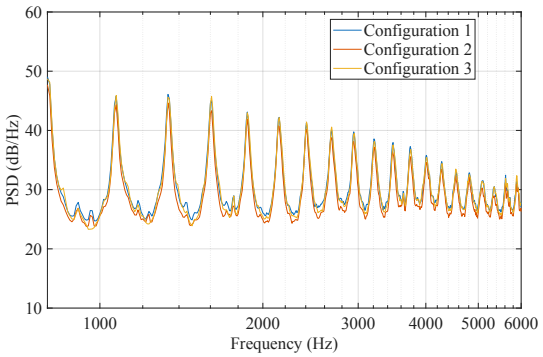

(c) $\vec{V}_{Tip} = 76.6m/s$, Tunnel Turned Off.

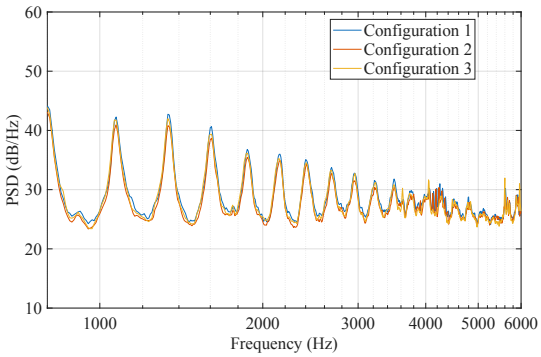

(d) $\vec{V}_{Tip} = 76.6m/s$, Tunnel at $4m/s$.

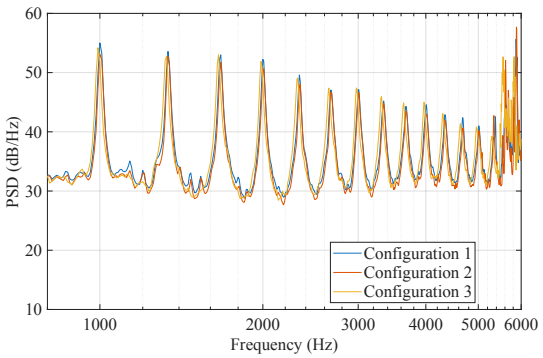

(e) $\vec{V}_{Tip} = 95.8m/s$, Tunnel Turned Off.

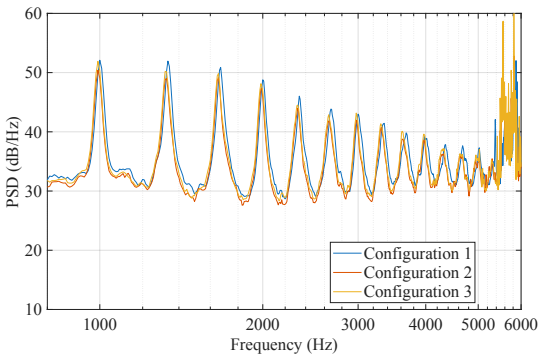

(f) $\vec{V}_{Tip} = 95.8m/s$, Tunnel at $4m/s$.

Figure 5.15: Comparison of Indoor Broadband Noise of Microphone 5 for Configurations 1, 2 and 3, Propeller Tip Speeds of $57.5m/s$, $76.6m/s$, and $95.8m/s$, and Both Tunnel Conditions.

interactions at the VTSMART facility. This contrasts the results from the Drone Park experiment in Chapter 4, where sequestration of the time-series data into near-zero inflow ($-1m/s$ to $0.5m/s$) segments and small positive inflow ($0.5m/s$ to $3m/s$) segments had a significant noticeable effect on both broadband and tonal components. This may be due to the nature of each facility. At the Drone Park, the area surrounding the propeller is open,

allowing for more free convection of any structures that may cause noise, even with smaller wind velocities. On the contrary, the VTSMART is mainly enclosed despite being an open jet wind tunnel with a $1.27m \times 1.27m$ outlet. This confinement, relative to the Drone Park, would enclose the same potentially noisy structures despite an inflow of $4m/s$.

Within each subfigure, there appear to be very little differences among the spectra, varying by at most about $3dB$, suggesting that at this scale, turbulence trips and pitch have little effect. Although small, it is generally consistent at each condition that the loudest configuration is Configuration 1. This is not quite expected, since the addition of turbulence trips would increase turbulent boundary layer trailing edge noise, so it would be expected that Configuration 3 be the loudest and Configuration 2 be the quietest. However, these differences are small, and the small trend that is visible may again be attributed to the lack of structure convection in the confined wind tunnel and low inflow velocity. Recall from SubFigure 4.22b from the previous chapter that Configuration 1 also appears louder than Configurations 2 and 3, and that this was due to the low inflow velocities. These suggest that the effects of pitch and turbulence trips may be outweighed by lack of convection, which would increase broadband noise due to other sources, such as TIN.

5.3 Summary

The background noise at the VTSMART facility was well under the quietest propeller noise measurements, with a positive SNR throughout the entire $100Hz$ to $20000Hz$ frequency spectrum and a minimum of about 1 around $120Hz$. This allows for a broad range of frequencies comparable to the outdoor Drone Park spectra. Furthermore, the background noise at the VTSMART facility was constant and therefore subtracted from the propeller noise spectra. This had negligible effect on the propeller noise spectra above $100Hz$.

Spectrogram analyses also reveal that the measured propeller acoustics are independent of time, with both the tunnel turned off and the tunnel operating with $4m/s$ flow. OASPL over time for each microphone was plotted on a polar plot, with microphone angle on the angular axis and time on the radial axis. These plots also reinforce time-invariance of the propeller noise for each microphone. Furthermore, the variation of OASPL with microphone position is consistent with the expected dipole-like directivity of a rotor.

Decomposition of the total spectra into broadband and tonal components show that the majority of the noise is composed of broadband noise, a similar result to the Drone Park results. The relative strength of the tonal component at the indoor VTSMART facility is higher than the relative strength of the tonal component at the outdoor Drone Park facility. These tones correspond most strongly at the BPF, its harmonics, and the shaft rate, its harmonics, and motor noise. Even at these tones, there are strong broadband components, suggesting that they are dominated by stochastic interactions. The experimental broadband noise has a similar shape to the GLSM above $1000Hz$, but the levels do not match con-

sistently, and the experimental broadband trend peaks around $4000Hz$ whereas the GLSM predicts a peak at about $6500Hz$.

Acoustic spectra from indoor experiments were scaled based on the distance from the propeller to the microphones since the microphone positions from the outdoor Drone Park experiment were different. This scaling makes the indoor spectra comparable to the outdoor spectra, and such comparisons reveal that the broadband noise around $2000Hz$ to $6000Hz$ is very similar between the indoor and outdoor experiments. These similarities diminish with an increase in RPM, and the largest differences occur at the tones of the BPF and its harmonics. Furthermore, the spectra become more similar when comparing the $4m/s$ flow condition from the indoor experiment to the sequestered spectra from the outdoor experiment than when comparing the no flow condition to the full spectra. This reinforces the idea that sequestering the time series data from outdoor acoustic testing generates spectral data relevant to similar indoor tests.

When comparing all configurations, there appear to be little differences among all the spectra. Additionally, what small trend that is visible does not conform to expectations: the addition of turbulence trips did not consistently show an increase in broadband noise, and the reduction in pitch angle did not show a consistent decrease in broadband noise. However, this may be due to the confinement of the test facility and the inability of the flow to convect structures such as the wake away from the propeller, which would cause the noise to be dominated by other sources, such as TIN.

Further investigations can be conducted to improve upon this experiment and provide supplementary material to support these results. For example, particle imaging velocimetry (PIV) could be done synchronized to the acoustics. This would provide visuals to observe the behavior of structures near the propeller and perhaps confirm if the wake is indeed loitering near the propeller and not being convected downstream. Collecting data for these configurations with more tunnel speeds could also provide more comparability to the Drone Park experiment, especially if higher speeds are required to counteract the confinement of the wind tunnel test section.

Chapter 6

Conclusion

Ultimately, the work presented in this document aimed to contribute towards the ability to relate outdoor acoustic experiments to indoor acoustic experiments, specifically bearing in mind the limitations due to scale. To prepare for such experiments, experimentation was done in an anechoic chamber to characterize the response of circular plywood ground boards with a diameter of $1m$ and a thickness of $6mm$. The significant findings from this experiment are:

- at shallower incidence angles of 20°, 23°, and 45°, the measured ΔPSD is similar to that of a perfect reflector within a few decibels ($6dB \pm 3dB$), especially between $200Hz$ and $10000Hz$, and this behavior is seen for both microphone positions, which justifies the assumption of a perfect reflector in the results of the Drone Park experiment
- at steeper incidence angles of 65° and 80°, the measured ΔPSD is similar to that of a perfect reflector within a few decibels ($6dB \pm 3dB$) only within about $2000Hz$ to $7000Hz$ for the microphone at the center of the ground board, but extends to about $200Hz$ to $8000Hz$ for the microphone at three-quarters the radius of the ground board
- at steeper incidence angles, a microphone placed at the center of a circular ground board is more susceptible to interference patterns from edge reflections, demonstrated by the deviation of the response from that of a perfect reflector
- with the microphone at three-quarters the radius of the ground board, the measured ground board response is similar to that with the microphone at the cneter of the ground board, but the ΔPSD is less sensitive to source angle

Once the behavior of the ground boards was understood, they were used in the outdoor Drone Park facility. Here, the acoustics of two geometrically similar Techsburg propellers, one with a diameter of $0.457m$ and one with a diameter of $0.914m$, were measured. 13 microphones were placed on top of ground boards in a $4.6m$ semicircle around the propeller, starting from directly upstream of the propeller and evenly spaced to directly downstream of the propeller. The significant findings from this experiment are:

- background noise is significant compared to quiet rotor noise up to about $800Hz$

- motor noise from the T-Motor U15-II KV100 is dominant around the $6000Hz$ to $9000Hz$ frequency range
- the majority of the propeller noise appears as a broadband component, with the tonal component being significant only at the shaft rate, blade passage frequencies and their harmonics
- a decrease in inflow velocity (including negative inflow or flow from behind the propeller) corresponds to an increase in OASPL and PSD, especially in the $2000Hz$ to $6000Hz$ frequency range
- sequestering the time-series data was done to separate small positive inflow conditions ($0.5m/s < u_{wind} < 3m/s$) from negative and near-zero inflow conditions ($-1m/s < u_{wind} < 0.5m/s$), and the former condition resulted in lower broadband noise than the latter condition, typically by about $1dB$ to $3dB$ in the $2000Hz$ to $6000Hz$ frequency range
- the GLSM overpredicts the spectra calculated from the former condition by up to about $10dB$, whereas the GLSM matches the broad spectral features of the latter condition within about $3dB$ for the smaller scale and about $6dB$ for the larger scale
- the reduction in pitch angle generally decreased the broadband noise, which is expected with a reduction in thrust
- the addition of turbulence trips unexpectedly did not consistently increase broadband noise, which may be due to the lack of similar wind conditions, making the two configurations less comparable

To have a comparison for the outdoor experiment, a similar experiment took place at the indoor Virginia Tech Subsonic Modular Anechoic Research Tunnel (VTSMART). Due to limitations of the size of the wind tunnel, only the $0.457m$ diameter propeller was tested, and 6 microphones were used, two of which were in a position relative to the propeller similar to two in the Drone Park experiment. The significant findings from this experiment are:

- background noise is insignificant compared to quiet rotor noise above about $150Hz$
- background noise and propeller noise are constant with respect to time and can be directly subtracted from each other
- the majority of propeller noise appears to be broadband even with $4m/s$ flow, suggesting that there may still be some recirculation and reingestion of the propeller wake due to the confined chamber
- after normalizing on distance, the broadband noise spectra from the outdoor Drone Park experiment are comparable to the indoor VTSMART experiment within $\pm 2dB$ in the $1000Hz$ to $6000Hz$ frequency range

- comparing sequestered spectra considering $0.5m/s < u_{wind} < 3m/s$ from the outdoor experiment to the indoor experiment with $4m/s$ flow is more similar than comparing the full spectra from the outdoor experiment to the indoor experiment with $0m/s$ flow
- there were insignificant changes to noise when changing pitch and turbulence trips, suggesting that other sources dominated over loading and trailing edge noise, likely due to the confinement of the anechoic wind tunnel facility entrapping structures such as the wake near the propeller

There is plenty of room for improvement with these experiments, and further research and experiments may yield great results. The author suggests:

- further characterizing the ground board response at more source incidence angles and microphone configurations, which would provide more understanding to potentially correct for ground board effects in further acoustic experiments
- obtaining exact ground board calibrations before outdoor field tests rather than using an assumption of a perfect reflector, which would also provide more tools to correct for ground board effects and possibly account for unexpected behavior seen in the presented outdoor experiment
- measuring synchronized wind velocity data and thrust data to acoustics, which would make the sequestration more accurate and easier
- using more microphones at geometrically similar positions in an indoor anechoic wind tunnel for further comparability to outdoor tests
- obtaining synchronized particle imaging velocimetry (PIV) to the acoustics to further understand detailed effects of flow, which may confirm if the confinement of the anechoic wind tunnel facility is causing structures to be trapped near the propeller

Bibliography

[1] Toufic Abboud, Ahmed Bennani, Benoit Chaigne, Nedezda Petrova, Xiaodong Zhou, and Vincent Blandeau. Modelling of an infinite impedance ground plane for aircraft noise flight simulation. In *AIAA Aviation 2021 Forum*, August 2021. doi: https://doi.org/10.2514/6.2021-2141.

[2] Mark C. Anderson, James H. Stephenson, Nikolas S. Zawodny, and Kent L. Gee. Characterizing the effects of two ground-based outdoor microphone configurations. *Proceedings of Meetings on Acoustics*, 39(1), December 2019. doi: https://doi.org/10.1121/2.0001388.

[3] Julius S. Bendat and Allan G. Piersol. *Random Data: Analysis and Measurement Procedures*, volume 729. John Wiley & Sons, Incorporated, 4 edition, February 2010. ISBN 9780470248775.

[4] Vincent Blandeau and Philippe Bousquet. A new plate design to improve the accuracy of aircraft exterior noise measurements on the ground. In *AIAA Aviation 2021 Forum*, August 2021. doi: https://doi.org/10.2514/6.2021-2158.

[5] European Union Aviation Safety Agency. *Guidelines on Noise Measurement of Unmanned Aircraft Systems Lighter than 600 kg Operating in the Specific Category (Low and Medium Risk) (TE.RPRO.00034-011)*, June 2023.

[6] Jonathan Fleming, Matthew Langford, Jacob Gold, Kyle Schwartz, David Wisda, Nathan Alexander, and Jeremiah Whelchel. Measured acoustic characteristics of low tip speed evtol rotors in hover. In *Vertical Flight Society 78th Annual Forum & Technology Display*, May 2022. doi: 10.4050/f-0078-2022-17434.

[7] Jonathan Fleming, Matthew Langford, Will Walton, Ricardo Burdisso, Bennett Witcher, Nathan Alexander, and ThanhLong Duong. Experimental and numerical acoustic scaling investigation of a low tip speed evtol proprotor in hover. In *Vertical Flight Society 81st Annual Forum & Technology Display*, May 2025. doi: https://doi.org/10.4050/F-0081-2025-99.

[8] Hyunjune Gill and Seongkyu Lee. Development of new empirical rotor broadband noise prediction models for urban air mobility applications. In *AIAA Scitech 2024 Forum*, January 2024. doi: https://doi.org/10.2514/6.2024-2473.

[9] Stewart Glegg and William Devenport. *Aeroacoustics of Low Mach Number Flows: Fundamentals, Analysis and Measurement*. Elsevier Science & Technology, 2nd edition, 2023. ISBN 9780443191121.

[10] International Civil Aviation Organization. *Annex 16 to the Convention on International Civil Aviation: Environmental Protection - Aircraft Noise*, 8th edition.

[11] International Electrotechnical Commission. *Wind Turbines - Part 11: Acoustic Noise Measurement Techniques (IEC 61400-11:2012)*, 3rd edition, November 2012.

[12] International Organization for Standardization. *Acoustics - Attenuation of Sound During Propagation Outdoors (ISO 9613-1:1993(E))*, 1st edition, 1993. URL https://www.iso.org/standard/17426.html.

[13] International Organization for Standardization. *Noise Measurements for UAS (Unmanned Aircraft Systems) (ISO 5305:2024)*, 1st edition, 2024. URL https://www.iso.org/standard/81111.html.

[14] Michael Kingan, Sung Tyaek Go, Rafael Piscoya, and Martin Andreas Ochmann. On the modelling of ground-board mounted microphones for outdoor measurements. *Journal of Sound and Vibration*, 565, October 2023. doi: https://doi.org/10.1016/j.jsv.2023.117894.

[15] Seongkyu Lee and Jessica G. Shum. Prediction of airfoil trailing-edge noise using empirical wall-pressure spectrum models. *AIAA Journal*, 57(3), March 2019. doi: https://doi.org/10.2514/1.J057787.

[16] Sichen Li and Seongkyu Lee. Ucd-quietfly: A new program to predict multi-rotor evtol broadband noise. In *2020 VFS Aeromechanics for Advanced Vertical Flight Technical Meeting*, January 2020.

[17] Sicheng Li and Seongkyu Lee. Prediction of urban air mobility multirotor vtol broadband noise using ucd-quietfly. *Journal of the Americal Helicopter Society*, 66(3), July 2021. doi: https://doi.org/10.4050/JAHS.66.032004.

[18] Jack E. Marte and Donald W. Kurtz. A review of aerodynamic noise from propellers, rotors, and lift fans. Technical report, National Aeronautics and Space Administration, January 1970.

[19] Robert J. Pegg. A summary and evaluation of semi-empirical methods for the prediction of helicopter rotor noise. Technical report, National Aeronautics and Space Administration, December 1979.

[20] Robert Schlegel, Robert King, and Harold Mull. Helicopter rotor noise generation and propagation. Technical report, U.S. Army Aviation Materiel Laboratories, October 1966.

[21] Jeremiah Whelchel. *Measurement and Prediction of Rotor Noise sources for sUAS in Outdoor and Laboratory Environments*. PhD thesis, Virginia Polytechnic Institute and State University, 2023.

[22] Jr. William L. Willshire and Paul A. Nystrom. Investigation of effects of microphone position and orientation on near-ground noise measurements. Technical report, National Aeronautics and Space Administration, April 1982.